

A panchromatic study of BLAST counterparts: total star-formation rate, morphology, AGN fraction and stellar mass

Lorenzo Moncelsi¹, Peter A. R. Ade¹, Edward L. Chapin², Luca Cortese^{1,3}, Mark J. Devlin⁴, Simon Dye¹, Stephen Eales¹, Matthew Griffin¹, Mark Halpern², Peter C. Hargrave¹, Gaelen Marsden², Philip Mauskopf¹, Calvin B. Netterfield⁵, Enzo Pascale¹, Douglas Scott², Matthew D. P. Truch⁴, Carole Tucker¹, Marco P. Viero⁵, Donald V. Wiebe²

lorenzo.moncelsi@astro.cf.ac.uk

ABSTRACT

We carry out a multi-wavelength study of individual galaxies detected by the Balloon-borne Large Aperture Submillimeter Telescope (BLAST) and identified at other wavelengths, using data spanning the radio to the ultraviolet (UV). We develop a Monte Carlo method to account for flux boosting, source blending, and correlations among bands, which we use to derive deboosted far-infrared (FIR) luminosities for our sample. We estimate total star-formation rates for BLAST counterparts with $z \leq 0.9$ by combining their FIR and UV luminosities. Star formation is heavily obscured at $L_{\text{FIR}} \gtrsim 10^{11} L_{\odot}$, $z \gtrsim 0.5$, but the contribution from unobscured starlight cannot be neglected at $L_{\text{FIR}} \lesssim 10^{11} L_{\odot}$, $z \lesssim 0.25$. We assess that about 20% of the galaxies in our sample show indication of a type-1 active galactic nucleus (AGN), but their submillimeter emission is mainly due to star formation in the host galaxy. We compute stellar masses for a subset of 92 BLAST counterparts; these are relatively massive objects, with a median mass of $\sim 10^{11} M_{\odot}$, which seem to link the $24 \mu\text{m}$ and SCUBA populations, in terms of both stellar mass and star-formation activity. The bulk of the BLAST counterparts at $z \lesssim 1$ appear to be run-of-the-mill star-forming galaxies, typically spiral in shape, with intermediate stellar masses and practically constant specific star-formation rates. On the other hand, the high- z tail of the BLAST counterparts significantly overlaps with the SCUBA population, in terms of both star-formation rates and stellar masses, with observed trends of specific star-formation rate that support strong evolution and downsizing.

Subject headings: cosmology: observations — galaxies: evolution — galaxies: high-redshift — submillimeter — surveys

1. Introduction

The physical processes associated with the evolution of the Universe have left an imprint in the extragalactic background light. The far-infrared (FIR) portion of the background is associated with forming galaxies in which the ultraviolet (UV) photons emitted by new born stars are absorbed and re-radiated by dust in the IR. Roughly half of the energy content of the starlight integrated over the age of the Universe is stored in the Cos-

mic Infrared Background (CIB), glowing with a broad peak at around $200 \mu\text{m}$ (Puget et al. 1996; Fixsen et al. 1998; Dwek et al. 1998). The tight connection between star formation and FIR luminosity provides a route to understanding the history of star formation in the Universe, by means of studying the CIB at wavelengths close to its peak (Gispert et al. 2000; Rowan-Robinson 2001; Chary & Elbaz 2001; Hauser & Dwek 2001).

The first leg on this route is to identify the sources contributing to the CIB. Ground-based surveys with the Submillimetre Common-User Bolometer Array (SCUBA) have revealed the existence of a population of distant, highly dust-obscured galaxies, similar to the Ultra Luminous Infrared Galaxies (ULIRGs) detected by *IRAS* (Smail et al. 1997; Hughes et al. 1998; Barger et al. 1998), which make up all the background at $850 \mu\text{m}$ (Blain et al. 1999). However, at these wavelengths the energy in the CIB is only one-thirtieth of the value at its peak, and the SCUBA population only contributes 20–30% to the CIB at its peak (Coppin et al. 2006; Dye et al.

¹Cardiff University, School of Physics & Astronomy, Queens Buildings, The Parade, Cardiff, CF24 3AA, U.K.

²Department of Physics & Astronomy, University of British Columbia, 6224 Agricultural Road, Vancouver, BC V6T 1Z1, Canada

³European Southern Observatory, Karl-Schwarzschild-Str. 2, D-85748, Garching, Germany

⁴Department of Physics & Astronomy, University of Pennsylvania, 209 South 33rd Street, Philadelphia, PA, 19104, U.S.A.

⁵Department of Astronomy & Astrophysics, University of Toronto, 50 St. George Street Toronto, ON M5S 3H4, Canada

2007).

Recent progress has been made through new observations obtained at 24, 70, and 160 μm by the MIPS instrument aboard the *Spitzer Space Telescope* (Rieke et al. 2004), and at 250, 350 and 500 μm by the Balloon-borne Large Aperture Submillimeter Telescope (BLAST, Devlin et al. 2004; Pascale et al. 2008), a forerunner of the SPIRE instrument (Griffin et al. 2010) on the *Herschel Space Observatory* (Pilbratt et al. 2010). These wavelengths bracket the CIB peak; several authors have shown through stacking analyses that 24 μm -selected galaxies resolve the CIB background, both on the short-wavelength side of the peak (Dole et al. 2006) and on its long-wavelength side (Devlin et al. 2009; Marsden et al. 2009).

Sources identified at 24 μm are mostly unresolved in the FIR, and have a redshift distribution with median of 0.9 (Pascale et al. 2009). A detailed multiwavelength study of these sources is the necessary next step. Starting from a catalog of $\geq 5\sigma$ BLAST sources, Dye et al. (2009, hereafter D09) have identified counterparts in 24 μm and radio catalogs (BLAST IDs). These tend to be relatively nearby sources (median z of 0.6, inter-quartile range of 0.2–1.0), with a median dust temperature of 26 K and a median bolometric FIR luminosity of $4 \times 10^{11} \text{ L}_\odot$, which contribute 20% to the CIB at 250 μm . Identified BLAST sources typically lie at lower redshifts and have lower rest-frame dust temperatures compared to submillimeter (submm) sources detected in surveys conducted with SCUBA (Chapman et al. 2005; Pope et al. 2005). However, D09 also note that the $\sim 40\%$ of BLAST sources without identified counterparts probably lie at higher redshifts on average. Finally, D09 illustrate how the apparent increase in dust temperature and FIR luminosity with redshift occurs as a result of selection effects.

We also note that three other multi-wavelength studies of fainter BLAST sources discovered in the deepest part of the map have been undertaken. Dunlop et al. (2010) concentrate on 250 μm radio-identified sources within GOODS-S (Dickinson et al. 2003, see Section 2.1) where the deepest ancillary data coincide. Chapin et al. (2010) use overlapping BLAST 250–500 μm and LABOCA 870 μm (Weiß et al. 2009) data in the larger Extended Chandra Deep-Field South (ECDFS) to constrain the Rayleigh-Jeans tail more accurately than was possible in D09. Finally, Ivison et al. (2010) study the FIR/radio correlation for a catalog of BLAST 250 μm -selected galaxies in the ECDFS; this sample is deeper than the D09 one, and yet slightly shallower than the selection in Dunlop et al. (2010). There is little overlap between the sources used in these studies and the shallower/wider-area sample from D09.

The basis of our present study is the D09 sample as its brighter, and lower-redshift objects were most eas-

ily followed-up in the optical and UV. However, we first extend the submm analysis of D09 by accounting for flux boosting, source blending and correlations among BLAST bands that inevitably arise in IR surveys as a consequence of finite instrumental angular resolution and source confusion (Coppin et al. 2005). We then identify counterparts to the BLAST IDs in the near- and far-UV *GALEX* maps, in order to quantify the total dust-obscured and unobscured star formation, as described by several authors (Bell 2003; Hirashita et al. 2003; Iglesias-Páramo et al. 2006; Buat et al. 2007). We also extend the analysis of Eales et al. (2009, hereafter E09) to combine spectroscopic data of BLAST IDs with optical, near-IR (NIR) and mid-IR (MIR) photometry in order to place firmer constraints on source redshifts, morphology, AGN fraction, and stellar masses.

We are able to assign spectroscopic and photometric redshifts to $\sim 62\%$ of the BLAST IDs. We use this information to estimate the rest-frame total FIR luminosity from the combined BLAST and MIPS photometry. We compare our FIR luminosities with those obtained from MIPS photometry only, finding a significant discrepancy for high luminosity sources ($L_{\text{FIR}} \gtrsim 5 \times 10^{11} \text{ L}_\odot$) at $z \gtrsim 0.5$. The BLAST and SPIRE wavebands are therefore fundamental in constraining the peak of hidden star formation at high redshift (see also e.g. Schulz et al. 2010; Elbaz et al. 2010).

In addition, UV counterparts are found for about 60% of the BLAST IDs. This allows us to estimate the fraction of UV photons that manage to escape the dust shroud, which is then combined with FIR data to build an estimator of the total star-formation rate (SFR_{tot}) ongoing in these sources. Recent observations at the same wavelengths (Rodighiero et al. 2010) delineate the UV contribution as marginal at all redshifts. We find that star formation is heavily obscured at $L_{\text{FIR}} \gtrsim 10^{11} \text{ L}_\odot$, $z \gtrsim 0.5$, but unobscured starlight plays an important role in low redshift, low FIR luminosity sources ($z \lesssim 0.25$, $L_{\text{FIR}} \lesssim 10^{11} \text{ L}_\odot$), in agreement with Buat et al. (2010).

We reanalyze the optical spectroscopy data from the AAOmega survey presented in E09 to obtain H α equivalent widths and [NII]/H α line ratios. This spectral analysis, combined with a qualitative study of the radio, MIR and optical emission, allows us to assess whether or not a BLAST galaxy is hosting an active nucleus: roughly 20% of the objects in our sample show evidence of AGN presence. Recent observations of FIR-selected samples (Wiebe et al. 2009; Coppin et al. 2010; Muzzin et al. 2010; Hatziminaoglou et al. 2010; Shao et al. 2010; Elbaz et al. 2010) show that the submm emission of such objects is mainly due to star formation ongoing in the host galaxy, rather than due to the AGN. Therefore we do not explicitly exclude AGN from our analysis, unlike other authors (Bell 2003; Iglesias-Páramo et al. 2006; Buat et al. 2007), but rather

flag them as such. Visual examination of BLAST IDs in UV, optical and MIR images (see Appendix A) is used to derive a broad morphological classification of these objects: at low redshift we find predominantly spirals, whereas most of the BLAST sources identified at high redshift are compact and show AGN signatures. This is probably a selection bias, as the fraction of submm sources identified at other wavelengths gradually decreases with z (see D09), and the farthest objects can often be identified only if they are particularly bright in the radio or in the optical, frequently an indication of AGN presence. As a matter of fact, the analysis carried out by Dunlop et al. (2010) shows that a deep survey at $250\mu\text{m}$ not only contains low- z spirals, but also extreme dust-enshrouded starburst galaxies at $z \sim 2$. Our analysis tends to miss the latter because they are typically extremely faint in the optical/UV, unless they also host an AGN.

Finally, stellar masses (M_\star) are estimated using the method detailed in Dye (2008), in order to study whether or not specific star-formation rates ($\text{SSFR} \equiv \text{SFR}/M_\star$) depend on stellar mass and L_{FIR} . The SSFR plays an important role as it measures the time scale of recent star formation in a galaxy, as compared to the star-formation rate integrated over the galaxy's history. Several studies (Santini et al. 2009; Rodighiero et al. 2010, and references therein) report that the SSFR increases with redshift at all masses, whereas the dependence of SSFR on mass is one of the most debated questions. In particular, we aim to understand whether or not sources selected at wavelengths longward of $200\mu\text{m}$ are experiencing a major episode of star formation, forming stars more actively than in their recent past and building up a substantial fraction of their final stellar mass. We highlight a dichotomy in the BLAST population: sources at $z \lesssim 1$ appear to be run-of-the-mill star-forming galaxies with intermediate stellar masses (median $M_\star \sim 7 \times 10^{10}\text{M}_\odot$) and approximately constant SSFRs, whereas the high- z tail of the BLAST counterparts significantly encroaches on the SCUBA population detected in the SHADES survey (Dye et al. 2008), in terms of both stellar masses and SSFRs. This is expected since there is good overlap between fainter BLAST sources and $870\mu\text{m}$ -selected galaxies (Dunlop et al. 2010; Chapin et al. 2010), but it is also important to establish an additional link with a shallower BLAST sample, using a methodology equivalent to that of SHADES. In addition, since the more massive BLAST galaxies at intermediate redshifts ($0 < z < 1$) seem to form stars more vividly than the equally massive and aged $24\mu\text{m}$ sources detected in the GOODS survey, we suggest that the BLAST counterparts may act as linking population between the $24\mu\text{m}$ -selected sources and the SCUBA starbursts.

The layout of this paper is as follows. In Section 2 we describe in detail the maps, images and catalogs

used throughout this paper. Section 3 and Section 4 are concerned with luminosities and star-formation rates in the FIR and UV, respectively. In Section 5 we build a unified estimator of total star formation and discuss the first results. In Section 6 we estimate the AGN content of our sample, while in Section 7 we outline a broad morphological scheme for our sources. In Section 8 we compute the stellar masses and present the main results. Section 9 contains our conclusions. Throughout this paper we assume the standard concordance cosmology: $\Omega_M = 0.274$, $\Omega_\Lambda = 0.726$, $H_0 = 70.5\text{ km s}^{-1}\text{ Mpc}^{-1}$ (Hinshaw et al. 2009).

2. Data

This Section describes the data sets used for our analysis, spanning from the UV to the submillimeter.

2.1. Submillimeter data

We use data from the wide-area extragalactic survey of BLAST described by Devlin et al. (2009), and centered on the Great Observatory Origins Deep Survey-South (GOODS-S, Dickinson et al. 2003, which in turn is centered on the Chandra Deep-Field South, CDFS) region. The maps cover an area of 8.7deg^2 with a 1σ depth of 36, 31 and 20mJy at 250 , 350 , and $500\mu\text{m}$, respectively. We refer to this region as the BLAST GOODS South Wide (BGS-Wide). A smaller region of 0.8deg^2 (BGS-Deep) nested inside BGS-Wide has a 1σ depth of 11, 9 and 6mJy at 250 , 350 , and $500\mu\text{m}$, respectively. These depths account for the instrumental noise only, and do not include confusion. Marsden et al. (2009) estimate that fluctuations arising from unresolved sources are a factor two larger than instrumental noise at $500\mu\text{m}$, in BGS-Deep. Catalogs of sources detected at each wavelength in BGS-Deep and BGS-Wide are presented by Devlin et al. (2009).

D09 combine these single-wavelength catalogs by selecting sources with a $\geq 5\sigma$ (instrumental only, no confusion noise) significance in at least one of the bands. They use this multi-band catalog to identify counterparts (BLAST primary IDs) in deep radio (ACTA and VLA, Norris et al. 2006; Miller et al. 2008) and $24\mu\text{m}$ (SWIRE and FIDEL, Lonsdale et al. 2004; Dickinson & FIDEL team 2007; Magnelli et al. 2009) surveys. The BLAST primary IDs all have $\leq 5\%$ probability of being a chance alignment. They also compile a list of secondary IDs, with different counterparts associated to the same BLAST source as the primary ID, but with larger probability of being a chance alignment.

In this work we present an extended version of the D09 catalog of BLAST primary IDs which contains 227 BLAST sources. In the following sections we update this list to include UV data, recent redshifts, corrections for submm flux boosting and blending, morphology, AGN

features, and star-formation rates (see Appendix B for data tables). The list of secondary IDs is extensively discussed in E09 and we do not investigate them further.

We emphasize again that the sample studied in this work comprises the subset of BLAST-selected bright sources for which optical spectroscopy/photometry is available, and/or for which we find a clear counterpart in the UV. Naturally, this is only a fraction of sources that would be in a purely BLAST-selected catalog, skewed towards lower redshifts and strong optical/UV fluxes.

2.2. Optical spectroscopy

A spectroscopic follow-up of the BLAST IDs was carried out with the AAOmega optical spectrograph at the Anglo-Australian Telescope. The BLAST spectroscopic redshift survey is discussed in E09, as well as the reduction of the spectral data; here we extend their analysis and results (see Sections 6, 7 and Tables 2, B1).

AAOmega (AAO, Sharp et al. 2006) consists of 392, 2"-wide fibers feeding light from targets within a 2° field-of-view; the configuration of diffraction gratings was chosen to yield a wavelength coverage from 370 to 880 nm, with spectral resolution $\lambda/\delta\lambda \simeq 1300$. At redshifts lower than 1, this allows us to detect two or more of the following lines: [OII] 372.7, Calcium H and K, H β , [OIII] 495.9 and 500.7, H α , [NII] 658.3 and [SII] 671.6 and 673.1. At redshifts greater than 1, we only rely on broad emission lines, such as Lyman α , SiIV 140.3, CIII] 190.9 and CIV 154.9.

We have produced two prioritized lists of targets. The first list comprises $\geq 3.5\sigma$ BLAST sources with primary radio or 24 μm counterparts¹. Sources selected at 24 μm are also included in the target list to use all the available fibers. The second list contains the secondary BLAST IDs, plus 24 μm sources.

The net observing time for the list of primary targets was 7 hr, obtaining spectra for 669 sources (316 BLAST IDs, and 356 SWIRE sources). The list of secondary targets was observed for only 1 hr (due to poor weather), obtaining 335 spectra (77 BLAST IDs, and 258 SWIRE sources). Spectroscopic redshifts were consequently obtained by E09 for 212 BLAST IDs in the primary list, 193 of which have $\geq 75\%$ confidence level (c.l.), and for 11 BLAST IDs in the secondary list (all with $\geq 75\%$ c.l.).

It is important to clarify here that the two lists used for the AAO observations are not fully coincident with the D09 list discussed in the previous section and used in this work. However, a large overlap among sources in these lists is present and 82 sources from the D09 catalog of BLAST IDs have AAO redshifts, all with $\geq 95\%$ c.l. (see Table B1).

Using the available spectra we estimate H α Equivalent Widths (EWs) and [NII]/H α line ratios for 56 of these 82 sources. The remaining 26 sources either are at too high redshift for the H α line to fall in our spectral coverage ($z \gtrsim 0.33$), or have spectra with poor signal-to-noise ratio. We calculate the uncertainties on the EWs as quadrature sum of the measurement error, estimated with a bootstrapping technique applied to the individual spectra, and the Poisson noise, estimated following Vollmann & Eversberg (2006, Equation 7).

We list the rest-frame EWs, $\text{EW}_{\text{rf}} = \text{EW}/(1+z)$, in Table B1, along with their uncertainties and the [NII]/H α line ratios. Note that we have applied a 1 \AA correction to the H α EW_{rf} for underlying stellar absorption (Hopkins et al. 2003; Balogh et al. 2004).

2.3. UV data

We identify near-UV (NUV) and far-UV (FUV) counterparts to BLAST IDs by searching for *GALEX* sources in the Deep Imaging Survey (DIS, Martin et al. 2005, data release GR-4/5) within 6" of the radio or 24 μm counterpart², a separation just slightly larger than the *GALEX* PSF FWHM (Morrissey et al. 2007). This choice is justified by the presence of a few extended objects, unresolved by the submillimetric beam, that contribute to the same BLAST source (see Section 7). After visual inspection of the UV images, we have added one additional interacting system extending beyond 6" from the BLAST ID (#2); in this case we integrate the UV magnitude from both the interacting objects, because they fall within the same BLAST beam. We estimate FUV and NUV magnitudes using the standard *GALEX* pipeline (Morrissey et al. 2007) for most IDs, whereas we perform aperture photometry on 13 extended objects. A magnitude is considered to be unreliable if the source is either confused or blended with a star.

We find that 144 BLAST IDs have a NUV counterpart (136 with reliable magnitude), and 113 have a FUV counterpart (107 with reliable magnitude). Three sources are outside the area covered by the DIS, and the remaining 80 BLAST IDs have no obvious counterpart. By comparing the flux estimates for objects detected in more than one *GALEX* tile (pointing), we find that the average uncertainty associated with the reproducibility of the measurement is 0.06 and 0.11 mag in NUV and FUV, respectively. For bright galaxies, these values are larger than the uncertainty in the calibration (0.03 and 0.05 mag in the NUV and FUV, respectively; Morrissey et al. 2007), and in the source extraction procedure (≤ 0.02 mag). The uncertainty on a quoted UV magnitude is therefore the sum in quadrature of these three terms, and it lies in the 1σ range of 0.07–0.25 mag and 0.12–0.5 mag in NUV

¹If only the 24 μm counterpart is present, we refine the position of the source by matching it with optical or IRAC 3.6 μm coordinates.

²If both counterparts are present, we use the arithmetic mean between the two sets of coordinates: $[\alpha_{\text{BLAST}}, \delta_{\text{BLAST}}]$.

and FUV, respectively.

GALEX postage-stamp images, $2' \times 2'$ wide, are used to study the UV-morphology of the BLAST IDs; a selection³ of these is shown in Figure A1. UV magnitudes and uncertainties are listed in Table B2.

2.4. SWIRE 70 and 160 μm MIPS maps

We use 70 and 160 μm fluxes extracted from SWIRE maps (Lonsdale et al. 2004) at positions $[\alpha_{\text{BLAST}}, \delta_{\text{BLAST}}]$ to constrain the SED of each BLAST source at wavelengths shorter than the emission peak (see Section 3.2). These maps overlap almost completely with BGS-Wide, and all the $\geq 5\sigma$ BLAST sources investigated in this work lie within them. The 1σ depth of the maps is 3.6 and 20.8 mJy at 70 and 160 μm , respectively.

2.5. MIR/NIR/optical images and catalogs

In addition to the aforementioned UV *GALEX* images, we investigate BLAST source morphology using optical and IR images. The latter are 3.6, 4.5, 5.8, and 8 μm IRAC (Fazio et al. 2004) images from the SWIRE survey. In the optical, we examine $(U\ g\ r\ i\ z)$ -band images, acquired with the 4m Cerro Tololo Inter-American Observatory (CTIO) as part of the SWIRE survey, and R -band images from the COMBO-17 survey (Wolf et al. 2004, 2008). In Figure A1 we show $2' \times 2'$ cut-outs for a selection³ of BLAST IDs.

For the purpose of studying the morphology, AGN fraction and stellar mass, we have also matched, using a search radius of $3''$ as in D09, the catalog of BLAST IDs to the following catalogs:

1. the SWIRE band-merged catalog consisting of optical $(U\ g\ r\ i\ z)$ and MIR IRAC fluxes⁴ (Surace et al. 2005);
2. the 17 band COMBO-17 optical catalog (Wolf et al. 2004, 2008);
3. the Multi-wavelength Survey by Yale-Chile (MUSYC; Gawiser et al. 2006) catalog for NIR photometry (J - and K -band).

As a result of this analysis, out of 227 BLAST IDs:

- 205 (90%) have an IRAC counterpart from the SWIRE survey;
- 114 (50%) have an optical (SWIRE and/or COMBO-17), and either a NIR (MUSYC) or MIR (3.6 or 4.5 μm , IRAC) counterpart⁵;

- 102 of the above 114 are detected in a minimum of 5 bands (optical, NIR and MIR);
- 52 of the above 102 have J - and K -band photometry from MUSYC.

We use the wealth of ancillary information for a variety of purposes: we refer to Sections 6, 7 and 8 for discussions on AGN fraction, morphology and stellar masses.

2.6. Redshifts

In addition to the 82 spectroscopic redshifts obtained with AAO for the BLAST primary IDs, we have found 5 additional spectroscopic redshifts by exploring the NASA/IPAC Extragalactic Database (NED) with a $1''$ search radius around each ID. For the other sources, we use photometric redshifts from the MUSYC-EAZY (Taylor et al. 2009), COMBO-17 (Wolf et al. 2004, 2008, only sources with $R \leq 24$) and Rowan-Robinson et al. (2008, RR08) catalogs, using again a $1''$ search radius. We carefully inspect each individual alignment by taking into account the imaging data in Figure A1, the UV photometry, the SED in the FIR/submm, and any additional information available from NED. In cases of BLAST IDs with more than one associated photometric redshift, priority is given in the order: EAZY, COMBO-17, and RR08. We have thereby acquired 53 additional photometric redshifts, of which 20 are from EAZY, 6 from COMBO-17 and 27 from RR08.

We have succeeded in assigning 140 redshifts out of 227 ($\sim 62\%$) objects in our sample. The redshifts are listed in Table B1, along with their provenance. Figure 1 shows the redshift distribution of the whole BLAST ID catalog, and of the UV subset used in Section 5 for discussion of the total star-formation rates. The number of sources with redshift is doubled with respect to the robust sample of D09⁶, but the median redshift is roughly halved. This apparent pronounced discrepancy, limited to the $z \lesssim 0.2$ bin, amounts to 40 sources and is due to the combination of two selection effects. First, roughly 15 sources in D09 with $z \lesssim 0.2$ (mostly from RR08) do not make it into the robust sample, mainly because the photometric redshift is intrinsically unreliable or, in a handful of cases, because the BLAST source has been spuriously identified with the counterpart. Second, 27 other sources with redshifts estimated in this work have no redshift in D09, because they have neither sky coverage from COMBO-17 nor from RR08; of these 27, 21 are from AAO, and 24 have $z \lesssim 0.25$. Therefore the apparent excess of low- z sources with respect to D09 partly reflects the inclusion of the AAO spectroscopic redshifts (naturally skewed towards low- z) and partly lies in the

³The complete set of full-color cut-outs can be found at http://blastexperiment.info/results_images/moncelsi/

⁴The lower limits for inclusion in the catalog are 7 (10σ), 7 (5σ), 41.8 (5σ) and 48.6 μJy (5σ) at 3.6, 4.5, 5.8 and 8 μm , respectively.

⁵We note that the sky overlap among BGS, SWIRE, COMBO-17 and MUSYC is limited to a $\sim 4.15 \text{ deg}^2$ region.

⁶The robustness of a source is assessed by D09 based solely on the goodness of the SED fit.

intrinsic robustness in D09 of either the photometric redshift or the counterpart itself.

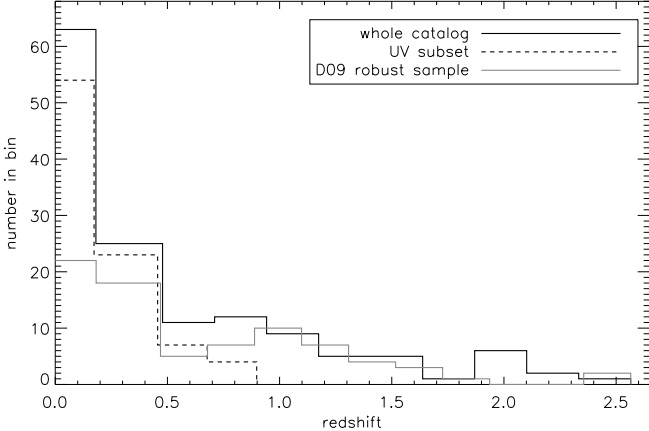


Fig. 1.— Redshift distributions for the whole catalog of BLAST IDs and for the subsample with UV data. The former has a median of 0.29 and an inter-quartile range of 0.12–0.84; the latter has a median of 0.18 and an inter-quartile range of 0.10–0.34. We also show the redshift distribution for the robust sample of D09, with median of 0.6 and an inter-quartile range of 0.2–1.0.

It is worth noting here that this study misses a large fraction of the high- z BLAST sources that are known to constitute an important part of the BLAST population (Devlin et al. 2009; Marsden et al. 2009; Pascale et al. 2009). This is again due to the combination of two factors. First, $\sim 38\%$ of the BLAST IDs presented in this paper do not have a redshift estimate; using information about the UV identification rate (similarly to D09), we can argue that more than half of the sources without a redshift estimate lie at $z \gtrsim 0.7$. In fact, 90 out of 99 (91%) sources at $z \leq 0.7$ (and 96 out of 115, 83%, sources at $z \leq 1$) have a *GALEX* counterpart; now, of the 87 sources with no redshift estimate, 57 (66%) do not have a *GALEx* counterpart. Under the assumption that the UV identification rate is a reasonable (if coarse) estimator of redshift, arguably more than half of the sources without a redshift estimate lie at $z \gtrsim 0.7$ and roughly half lie at $z \gtrsim 1$. Secondly, D09 starts with a catalog composed of bright, $\geq 5\sigma$ sources with flux densities $\geq 33\text{ mJy}$ at $250\mu\text{m}$, $\geq 27\text{ mJy}$ at $350\mu\text{m}$, and $\geq 19\text{ mJy}$ at $500\mu\text{m}$; Dunlop et al. (2010) and Chapin et al. (2010) clearly show the necessity of digging deeper into the BLAST maps, with the aid of the deepest available multi-wavelength data, in order to identify the faintest, high- z BLAST galaxies. Of course, this is done at the expense of the size of the submm sample, which inevitably drops to a few tens of sources.

Nonetheless, the present study is still unique in terms of size of the sample, wavelength coverage, depth and quality of the ancillary data. Indeed, *IRAS* sources have

been studied at many wavelengths (e.g. Della Valle et al. 2006; Mazzei et al. 2007), but with little knowledge of the details of the cold dust emission from which the FIR star-formation rate estimates come. Some improvements have been made with the SCUBA Local Universe and Galaxy Survey (SLUGS; Dunne et al. 2000; Vlahakis et al. 2005), but still with limited ability to estimate the bolometric FIR luminosity. The results in this paper probably will not be immediately replaced by deeper surveys undertaken by *Herschel*; in fact, even the much more sensitive observations carried out with SPIRE will have to face the lack of deeper ancillary data. This is especially true in the optical/NIR, where most of the $z > 2$ submm galaxies are much too faint to be detected by instruments like AAOmega, and in the radio, where the identification rate of the faintest $z > 2$ sources drops drastically, even when using the deepest available data (VLA).

3. FIR luminosities and SFRs

3.1. Deboosting the BLAST fluxes

The sources in the BLAST catalog used by D09 to identify counterparts in the radio and $24\mu\text{m}$ were detected directly from the maps of BGS-Deep and BGS-Wide. While the details of the catalog are discussed there, it is useful to summarize here the procedure to clarify what are the potential biases.

First, a catalog of BLAST sources with detection significance higher than 3σ is made at each wavelength, independently. Each entry in the catalog is then positionally matched across the three bands, with the requirement of a 5σ detection in at least one band. The significance here is relative to instrumental noise, and does not include confusion noise. A new position is assigned to the source by averaging its positions in the original single-wavelength catalogs, with weights estimated by taking into account the beam sizes and the signal-to-noise ratios (SNRs) of the detections at each wavelength. This combined catalog is then used to identify counterparts in the radio and at $24\mu\text{m}$, and a new flux density is measured from the 70 to $500\mu\text{m}$ maps at the accurate position of the counterpart.

The BLAST differential source counts fall very rapidly with flux density (approximately following $dN/dS \propto S^{-3}$, Patanchon et al. 2009), thus Eddington bias as well as source confusion will cause the fluxes to be boosted. This effect has to be estimated to properly compute the FIR luminosity of each source. Coppin et al. (2005) have proposed a Bayesian approach that can be applied to estimate the most likely flux distribution when the noise properties of the detection and the underlying source distribution are known. Their method is derived under the assumption that the flux density comes from just one source, plus noise. This cannot be applied to BLAST

sources because of blending: the measured flux density can either come from just one source, or more likely from several sources blended together by the beam, which then appear as one single source of larger flux density.

We have developed a different method to account for boosting of BLAST fluxes, which is entirely based on Monte Carlo simulations. We generate 100 noiseless sky maps using the BLAST measured count models (Patanchon et al. 2009), and no clustering. Noise is added to each simulated map to a realistic level for the BGS-Deep and BGS-Wide regions. Sources are then retrieved with the same method used on the real maps (Devlin et al. 2009). Considering all the input components within a FWHM beam distance from each retrieved source, we stipulate that the input component with largest flux density is the actual counterpart⁷ (ID). The source flux density is then remeasured at the position of the ID. Finally, we compare this flux density with that of the input source. By repeating this for each source detected in each simulation, we generate distributions of input/output SNR, where the relevant noise is the instrumental noise at the position of the ID. These simulations are similar to those used in Chapin et al. (2010) to study the effects of confusion for their deeper sample.

Figure 2 shows the result of this analysis. In each bin we display the median of the distribution of input SNR (labeled SNR_{ID}) corresponding to the measured SNR. The error bars define the first and third interquartiles. To obtain the deboosted flux density likelihood, it suffices to multiply the y -axis by the corresponding instrumental noise. It is clear from this figure that sources in the BGS-Wide region are only moderately affected by boosting. The situation is substantially different for BGS-Deep, and the effect of boosting increases with wavelength, as expected, due to the telescope PSF becoming larger. At the longest BLAST wavelength, the fluxes are severely affected by boosting: a source detected even with a 10σ significance level has a deboosted flux only about half of what is measured directly from the map. By comparing the deboosted values for BGS-Wide at 250 and 350 μm , we notice that the longer wavelength appears to be slightly less biased. This arises from the fact that the two PSFs are not very different in size (36 and 42'', respectively), but the 250 μm PSF has larger sidelobes (Truch et al. 2009).

3.2. SED fitting and FIR luminosities

In order to estimate the rest-frame FIR luminosity (L_{FIR}) of each BLAST source in our sample, we perform SED fitting using the MIPS flux densities (70 and 160 μm

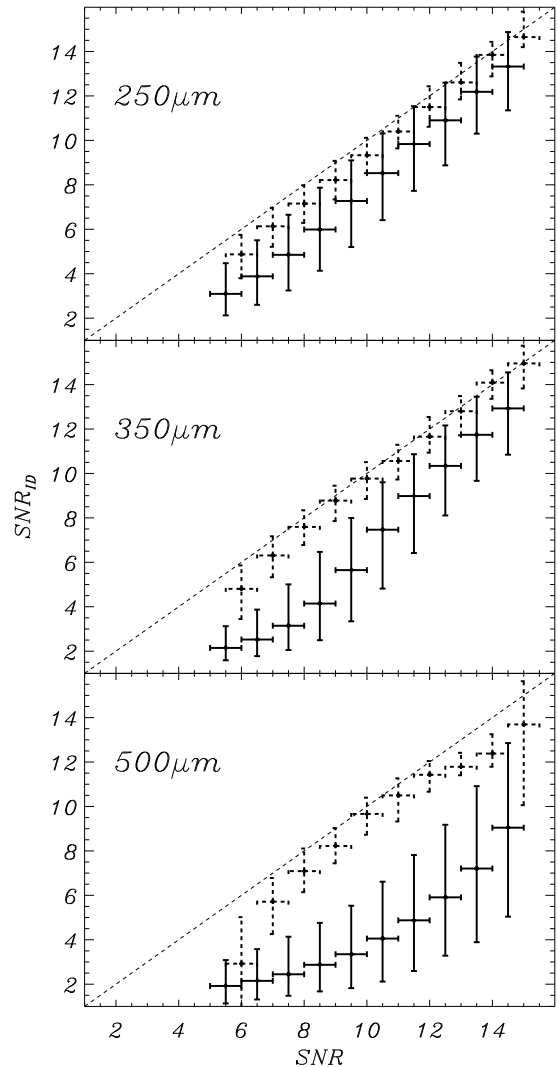


Fig. 2.— Effects of flux boosting, and source blending at BLAST wavelengths in BGS-Deep (solid error bars) and in BGS-Wide (dashed bars). For a source with a measured SNR at a given wavelength, the points show the distribution of the SNR_{ID} retrieved from simulations, binned in 1-SNR wide bins. Each point indicates the median value of the distribution in each bin, and the low and high error bars are the first and third interquartiles, respectively. The dashed line indicates where the points would lie in the absence of biases. The effects are mild in the wide region, where instrumental noise dominates, and get more severe in BGS-Deep, where confusion noise dominates, and source blending becomes more important. At the longest wavelength, the beam size blends fluxes from many adjacent sources, giving a strong bias. This is not a major problem for our analysis, which deals with sources identified at low, or moderate redshifts.

⁷We know that this assumption is always verified in BGS-Wide but less so in BGS-Deep, where, in 21% of the cases, the second brightest component contributes to more than 50% of the retrieved flux (see E09, Appendix B).

only) and the deboosted BLAST flux densities; the model template is a modified blackbody spectrum (with spectral index $\beta = 1.5$, Hildebrand 1983), with a power law $\nu^{-\alpha}$ replacing the Wien part of the spectrum, to account for the variability of dust-temperatures within a galaxy (we choose $\alpha = 2$, Blain et al. 2003; Viero et al. 2010). Pascale et al. (2009) have shown that the estimated FIR luminosities depend weakly on the choice of α , whereas the estimated dust temperatures are more sensitive to the template used. Since our analysis does not employ temperature measurements, the value of α we adopt is not critical. We also note here that the SED template chosen is the one that best performs in fitting the spectrum of two often-used IR-luminous local galaxies, Arp 220 and M82; by sampling their SEDs at the five observed wavelengths in question, the nominal FIR luminosities and dust temperatures are correctly retrieved (within uncertainties) not only at $z \sim 0$, but also when their spectra are redshifted up to $z = 2$.

The way each BLAST flux density is deboosted depends on its SNR. If this is larger than 15, no correction is applied. If the measured flux density is smaller than twice the square root of the sum in quadrature of instrumental and confusion noise (as reported in Marsden et al. 2009), the detection is treated as an upper limit. In all other cases, the above deboosting distributions are used. For sources in BGS-Deep the deboosting likelihood distribution is well approximated by a Gaussian function, but this is less true in BGS-Wide (especially at low SNR). Therefore, we use the sampled distribution for sources in BGS-Wide, and a Gaussian approximation in BGS-Deep.

The portion of noise arising from confusion is highly correlated among bands. The Pearson coefficients of the correlation matrix are listed in Table 1, and have been estimated from the (beam-convolved) BGS-Deep and BGS-Wide maps. As expected, the correlation effects are more important for sources in BGS-Deep, and we do take this into account in the SED fitting algorithm, whereas no correlations among bands are considered for sources in BGS-Wide. This turns out to be convenient, as in BGS-Deep the distributions are Gaussian, and a correlation analysis is relatively straightforward. This would not be the case for the sources in BGS-Wide.

MIPS fluxes at 70 and 160 μm were also used in the fitting routine to constrain the SED at wavelengths shorter than the emission peak. Deboosting these bands is beyond the scope of this paper, and it is less necessary because the source counts are shallower than the BLAST ones (see Frayer et al. 2009; Béthermin et al. 2010). The SED fitting procedure copes with the size of the photometric bands (color-correction), and the instrumental plus photometric uncertainties (Truch et al. 2009). Correlations are properly taken into account via a Monte Carlo procedure.

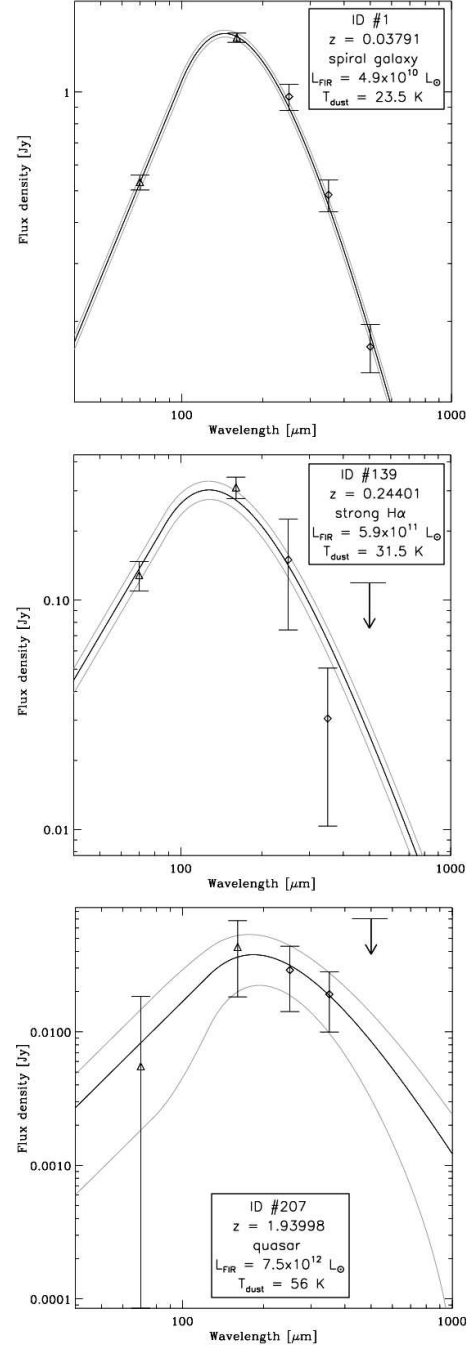


Fig. 3.— SED fitting of the FIR flux densities for three representative objects in our sample. Points with error bars are from BLAST (deboosted, color-corrected 250, 350, and 500 μm) and MIPS (70 and 160 μm); arrows indicate upper limits (see text). Black solid lines show the best-fit curves, with 68% confidence levels displayed as gray solid lines. The fitting routine accounts for the finite BLAST bandwidths and for the correlated calibration uncertainties. The model template is a modified graybody with an emissivity law $\beta = 1.5$ (Hildebrand 1983) and a power law $\nu^{-\alpha}$ replacing the Wien part of the spectrum ($\alpha = 2$, Blain et al. 2003; Viero et al. 2010).

TABLE 1
CORRELATIONS AMONG BLAST BANDS

Band [μm]	Pearson correlation matrix					
	BGS-Deep			BGS-Wide		
	250 μm	350 μm	500 μm	250 μm	350 μm	500 μm
250	1	0.68	0.66	1	0.26	0.29
350		1	0.69		1	0.29
500			1			1

In Figure 3 we show the fitted FIR SED for three representative objects in our sample: a low-redshift spiral galaxy; a mid-redshift strong $\text{H}\alpha$ emitter; and a high- z quasar. The resulting FIR luminosities, listed in Table B2, are the rest-frame SED integral between 8 and 1000 μm (Kennicutt 1998).

In Figure 4 we compare our estimates of rest-frame FIR luminosity with those obtained using only MIR flux densities, to investigate the level of uncertainty when data are not available in the submm. Following the prescription of Dale & Helou (2002), we calculate the FIR luminosities using only MIPS flux densities (24, 70 and 160 μm) for a $z \leq 2$ subset of 93 sources with 24 μm counterpart. There is considerable agreement up to $L_{\text{FIR}} \lesssim 5 \times 10^{11} L_{\odot}$ and $z \lesssim 0.5$. At higher redshifts (and luminosities) we find a poorer concordance; the MIPS-only estimates tend to overestimate the FIR luminosity, by as much as a factor of two in some cases. Other authors (Pope et al. 2006; Papovich et al. 2007; Kriek et al. 2008; Murphy et al. 2009; Muzzin et al. 2010; Elbaz et al. 2010; Nordon et al. 2010) find similar trends; this is expected as the MIPS bands sample the SED peak progressively less and less as redshift increases, thus pulling the SED toward shorter wavelengths, and resulting in a higher L_{FIR} . This emphasizes how essential the BLAST and SPIRE wavebands are to constrain the IR emission peak of star-forming galaxies at high redshift (see also e.g. Schulz et al. 2010; Elbaz et al. 2010).

3.3. FIR Star-Formation Rates

The FIR luminosities are a sensitive tracer of the young stellar population and, under some reasonable assumption, can be directly associated to the Star-Formation Rates (SFRs). This is particularly true for dusty starburst galaxies, because the optically thick dust surrounding star forming regions is very effective in absorbing the UV photons emitted by young, massive stars and converting this energy into IR emission.

Under the assumption that the above is the only physical process heating up the dust, Kennicutt (1998) has derived the following relation between SFR and bolometric

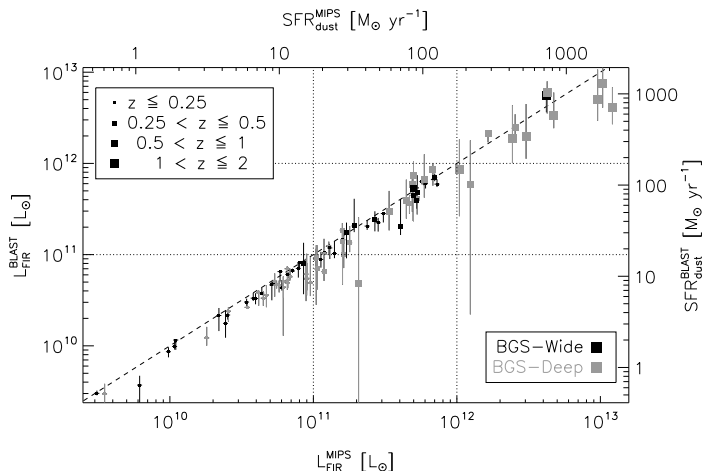


Fig. 4.— Comparison of estimates of total FIR luminosity for a $z \leq 2$ subset of 93 sources with 24 μm counterpart. On the x -axis we used the prescription of Dale & Helou (2002, Equation 4) based on 24, 70 and 160 μm MIPS fluxes; the error bars are set to 4%, which represents the mean discrepancy between their prescription and their model bolometric IR luminosities. On the y -axis we used the FIR luminosity estimates and uncertainties described in Section 3.2. Sources lying in the BGS-Wide region are in black and sources in BGS-Deep are in gray. Symbol sizes increase with redshift as shown in the legend. The secondary axes are both calculated using Equation 1. The dashed line shows $y = x$, for reference.

FIR luminosity:

$$\text{SFR}_{\text{dust}} \left[\frac{\text{M}_\odot}{\text{yr}} \right] = 1.73 \times 10^{-10} \times L_{\text{FIR}} [\text{L}_\odot]. \quad (1)$$

Our sample includes sources with a wide range of FIR luminosities. On one end, the FIR energy output is similar to the one found in Luminous IR galaxies (LIRGs, $L_{\text{FIR}} > 10^{11} \text{ L}_\odot$), and Ultra Luminous IR galaxies (ULIRGs, $L_{\text{FIR}} > 10^{12} \text{ L}_\odot$). In this type of source, AGN can play an important role in heating up the dust, resulting in a bias in the SFR calculation (an effect discussed further in Section 6). At lower FIR luminosities, we have strong additional evidence indicating that most of the galaxies sampled by BLAST are actively star-forming. This is shown in Figure 5: available $\text{H}\alpha$ rest-frame Equivalent Widths (EW_{rf}) are plotted against FIR luminosity for 56 sources at $z \lesssim 0.33$ (see Section 2.2). The horizontal dashed line at 4 \AA separates galaxies with ongoing star formation from quiescent ones (Balogh et al. 2004). All sources but one have $\text{H}\alpha$ signature of ongoing star formation. It is highly unlikely that, despite the poor statistics of this plot, we could be missing a population of quiescent objects with $L_{\text{FIR}} \lesssim 10^{10} \text{ L}_\odot$, whose FIR emission is due to a different physical process than the one described above.

Nonetheless, as the FIR luminosity decreases, our sources approach more normal star forming galaxies. In this type of source a non-negligible contribution to dust heating comes from older stellar populations, which would bias the SFR estimate high (Bell 2003; Hirashita et al. 2003; Iglesias-Páramo et al. 2004, 2006). The reduced optical depth of dust also needs to be taken into account or it would result in a lower estimate of SFRs (Inoue 2002). Both these effects are considered in the following discussion (Section 5) on the total SFR in our sample.

4. UV luminosities and SFRs

4.1. UV fluxes and rest-frame luminosities

The amount of unobscured star formation ongoing in each galaxy of our sample can be estimated in the UV for the BLAST IDs with a *GALEX* counterpart.

The (AB) UV magnitudes are corrected for extinction A_λ due to dust in our Galaxy, and converted into observed flux densities $S_{\nu_{\text{obs}}}$. Rest-frame UV luminosities are calculated as:

$$L_{\text{UV}}^{\text{rf}} = 4\pi S_{\nu_{\text{obs}}} D_{\text{L}}^2(z) \nu_{\text{obs}}, \quad (2)$$

where $D_{\text{L}}(z)$ is the luminosity distance.

The extinction coefficients used in the analysis are estimated following the prescription of Wyder et al. (2007), and the color excesses $E(B - V)$ as measured from DIRBE/IRAS dust maps (Schlegel et al. 1998) are listed in Table B2.

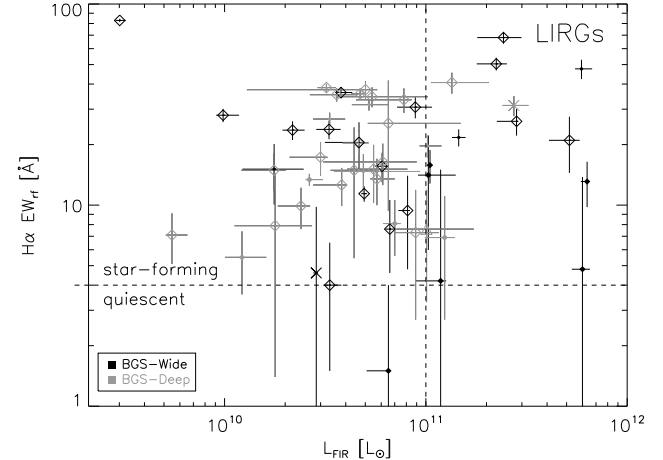


Fig. 5.— $\text{H}\alpha$ rest-frame Equivalent Widths (EW_{rf}) as a function of the FIR luminosity for the subset of 56 $z \lesssim 0.33$ sources described in Section 2.2. Note that we applied a 1 \AA correction to the $\text{H}\alpha$ EW_{rf} for underlying stellar absorption (Hopkins et al. 2003). Sources lying in the BGS-Wide region are in black, sources in BGS-Deep are in gray. We also encode here the morphological information discussed in Section 7: spiral galaxies are indicated with empty diamonds; compact objects with empty squares; ellipticals with triangles; interacting systems with crosses; Seyfert galaxies with filled diamonds; and objects without morphological classification with filled circles. The horizontal dashed line at 4 \AA separates galaxies with ongoing star formation from quiescent ones (Balogh et al. 2004). Clearly all galaxies in our sample but one are compatible with being actively forming stars.

4.2. UV Star-Formation Rates

Star-formation rates in the UV are estimated following the approach of Iglesias-Páramo et al. (2006, and references therein). These are related to rest-frame luminosities in the FUV and NUV by using a synthetic spectrum obtained with *starburst99*⁸ (*sb99*; Leitherer et al. 1999) for a star-forming galaxy. In the wavelength range 1000–3000 Å, the shape of the spectrum (shown in Figure 6) is very weakly dependent on the underlying stellar populations (e.g. Kennicutt 1998), and has a λ^{-2} slope.

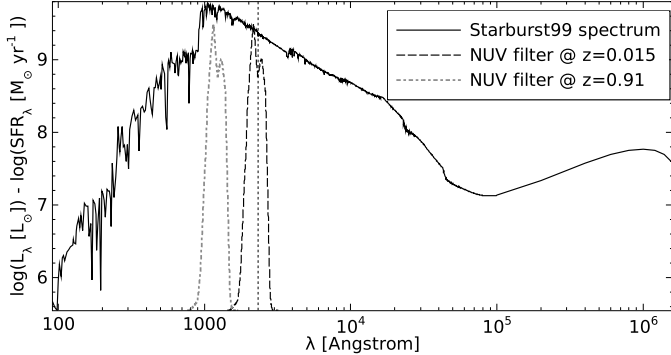


Fig. 6.— Synthetic spectrum computed with *starburst99* (Leitherer et al. 1999), under the assumptions of solar metallicity and Salpeter (1955) IMF from 0.1 to 100 M_{\odot} . Following Equations 3 and 4, the K -correction factor for the NUV, $K_{\text{NUV}}(z)$, is computed by averaging the synthetic spectrum over the broad *GALEX* filter profile, also shown (in arbitrary units), blueshifted for reference in the rest frame of the nearest and farthest object in our UV subsample. The same can be done for the FUV filter (not shown here).

NUV star-formation rates are estimated using the equation:

$$\log \text{SFR}_{\text{NUV}} \left[\frac{M_{\odot}}{\text{yr}} \right] = \log L_{\text{NUV}}^{\text{rf}} [\text{L}_{\odot}] - K_{\text{NUV}}(z), \quad (3)$$

where $L_{\text{NUV}}^{\text{rf}}$ is the rest-frame luminosity calculated from the observed near-UV magnitude using Equation 2. $K_{\text{NUV}}(z)$ is a redshift-dependent numerical factor which incorporates the K -correction, and is derived from *sb99*, integrating over the *GALEX* filter profile f_{NUV} :

$$K_{\text{NUV}}(z) = \frac{\int (\log L_{\lambda}^{\text{sb99}} [\text{L}_{\odot}] - \log \text{SFR}_{\lambda}^{\text{sb99}} [\frac{M_{\odot}}{\text{yr}}]) f_{\text{NUV}} d\lambda^{\text{rf}}}{\int f_{\text{NUV}} d\lambda^{\text{rf}}} \quad (4)$$

SFR_{FUV} and $K_{\text{FUV}}(z)$ are obtained in a totally analogous way. The values of $K_{\text{FUV}}(z=0)$ and $K_{\text{NUV}}(z=0)$ are the same as those used by Iglesias-Páramo et al.

(2006) at $z=0$. The photometric errors described in Section 2.3 are propagated in the estimate of the uncertainties on the UV SFRs.

A redshift limitation arises when the observed NUV and FUV sample the rest-frame Lyman continuum. This happens at $z \sim 0.36$ in the FUV, and $z \sim 0.91$ in the NUV. Hereafter we exclude sources beyond these redshift limits, as their inferred SFRs would be unreliable. In order to have a more uniform and sufficiently large sample, in what follows we only consider the NUV subset, which counts 89 sources (see Figure 1 for their redshift distribution). As anticipated, the UV luminosities/SFRs are not corrected for intrinsic dust extinction, and are combined in the next section with FIR luminosities to build an estimator of total SFR that is independent of extinction models.

5. Total SFR

We now have two separate estimators for the star-formation rates in our galaxy sample, SFR_{dust} and SFR_{NUV} . Each of these is expected to have different biases and short-comings. One can clearly do better at estimating the SFR by combining the two estimators in some way. The best way to do this is not obvious though, since it depends on how each of the estimators was calibrated, on the assumptions that went into them, on the range of galaxy SEDs being studied, and on how these relate to local galaxies that were used for calibration, including radiative transfer effects and other complications. Because of this, we choose to follow a prescription to estimate the total SFR in a galaxy which has already been used by several authors (Bell 2003; Hirashita et al. 2003; Iglesias-Páramo et al. 2006; Buat et al. 2007), so that we can at least compare our results to those of several related studies.

In order to estimate the total SFR (SFR_{tot}) in our sample, we combine the contribution from the obscured star formation with the unobscured star formation:

$$\text{SFR}_{\text{tot}} = \text{SFR}_{\text{NUV}} + (1 - \eta) \times \text{SFR}_{\text{dust}}. \quad (5)$$

A correction factor $(1 - \eta)$ is applied to the dust contribution to account for the IR emission from older stellar populations. Following Bell (2003) and Iglesias-Páramo et al. (2006), we use different values of η depending on whether the object in question is more likely to be a starburst ($\eta \sim 0.09$ for $L_{\text{FIR}} \geq 10^{11} \text{ L}_{\odot}$) or a normal star-forming galaxy ($\eta \sim 0.32$ for $L_{\text{FIR}} \leq 10^{11} \text{ L}_{\odot}$). As anticipated in Section 3.3, this method can account for both the contrasting effects that come into play when we try to estimate the total SFR budget for an inhomogeneous sample of objects. Namely, η parametrizes the contribution to dust heating from older stellar populations as a function of the integrated FIR luminosity, whereas the contribution from the UV luminosity guarantees that all

⁸Under the same assumptions of Iglesias-Páramo et al. (2006): continuous star formation, recent star-formation time scale $\sim 10^8$ yr, solar metallicity and Salpeter (1955) IMF from 0.1 to 100 M_{\odot} .

the UV photons that manage to escape the galaxy, due to the reduced optical depth of the dust, are actually taken into account.

We briefly recall here that the main selection effects of our sample are, on the one hand, that the rest-frame L_{FIR} increases steadily with redshift (see Figure 4 and D09), and on the other hand that the UV luminosity estimates are not reliable beyond $z \sim 0.9$. Moreover, we stress the importance of the blending effects reported in Section 3.1, which may lead to misidentifications, particularly in BGS-Deep (sources in gray).

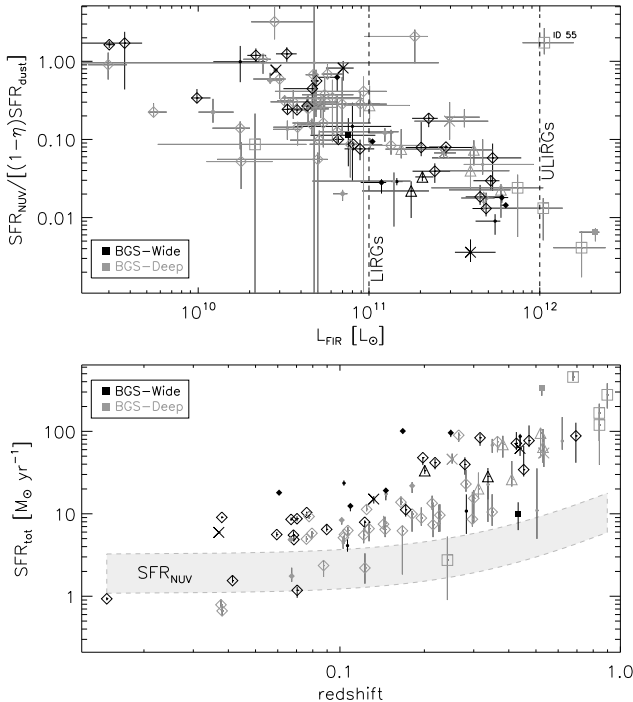


Fig. 7.— Top panel: ratio of SFR estimated from the NUV only to SFR estimated from dust only, as a function of the FIR luminosity. Note that SFR_{dust} is corrected by a factor $(1 - \eta)$ to account for the IR emission from old stellar populations (see text). Bottom panel: total SFR (SFR_{tot} , see Equation 5) as a function of redshift. The gray shaded area shows the 1σ confidence interval of a power-law fit to $SFR_{\text{NUV}} \propto z^{1.6}$. Symbols are as in Figure 5. Filled squares indicate that the source is a quasar (see Section 6).

The results of this analysis are shown in Figure 7. In the top panel we plot the ratio of SFR_{NUV} to $(1 - \eta)SFR_{\text{dust}}$ as a function of the FIR luminosity. With the exception of a few outliers⁹, there is a clear trend, namely the NUV contribution is more important at low- L_{FIR} (low- z), whereas star formation is mainly obscured

at $L_{\text{FIR}} \gtrsim 10^{11} L_{\odot}$, $z \gtrsim 0.5$. The same effect is evident in the bottom panel, where we plot SFR_{tot} as a function of redshift. The gray shaded area shows the 1σ confidence interval of a power-law fit $SFR_{\text{NUV}} \propto z^{1.6}$. Most sources with SFR_{tot} larger than a few $M_{\odot} \text{ yr}^{-1}$ have negligible contribution from the UV. This is consistent with what Takeuchi et al. (2009) find in the local Universe for a FIR-selected sample: at $SFR_{\text{tot}} > 20 M_{\odot} \text{ yr}^{-1}$, the fraction of directly visible SFR (SFR_{NUV}) decreases. A very similar trend is also observed at higher redshifts by Buat et al. (2008), with a $24 \mu\text{m}$ -selected sample at $0 \leq z \leq 0.7$ that closely resembles our sample at those redshifts, in terms of dynamic ranges and FIR-to-UV ratios.

Such a behavior in the individual BLAST IDs can be related to the greater evolution of the total FIR luminosity density with respect to the optical-UV one, as reported for instance by Pascale et al. (2009). On the other hand, we stress that at $L_{\text{FIR}} \lesssim 10^{11} L_{\odot}$, $z \lesssim 0.25$, FIR-only observations would lead to underestimates of the total SFR of at least a factor of 2.

By comparing our sample in Figure 7 with the *IRAS*/FIR-selected local sample of Iglesias-Páramo et al. (2006), we notice that the overlap is quite modest and limited to $L_{\text{FIR}} \lesssim 10^{10} L_{\odot}$, $z \lesssim 0.1$ sources. We point out that this conclusion should not be diminished by considerations on the extent of the local volume sampled by the BLAST survey.

At the very high luminosity end, only two objects (one of which is flagged as quasar, see Section 6) with $z \leq 0.91$ have a UV counterpart. We have thus investigated the 30 galaxies with $L_{\text{FIR}} \geq 10^{12} L_{\odot}$ in the full set of BLAST IDs, finding that 16 are flagged as quasars, most of which are optically bright. At $z > 1$, the optical U and g bands probe the rest-frame UV, and we calculate that these objects would virtually populate the top-right corner of the upper panel of Figure 7. However, the UV emission from quasars is strongly contaminated by the active nucleus, and cannot be directly associated with recent star formation. Of the remaining 14 ULIRGs with no AGN signatures, only 4 have optical magnitudes, and would occupy the bottom-right corner, indicating severe dust attenuation. We can therefore argue that, even if our subset of objects lacks the abundance of most luminous IR galaxies detected in the SHADES survey (see Coppin et al. 2008; Serjeant et al. 2008), SCUBA-like sources will likely lie in the bottom-right corner and beyond, following the same trend of increasing dust attenuation at higher FIR luminosities. This is a first hint that our analysis begins to detect SCUBA galaxies, which are known to overlap considerably with the fainter BLAST galaxy population, following joint studies of LABOCA $870 \mu\text{m}$ and BLAST data (Dunlop et al. 2010; Chapin et al. 2010). We will discuss this in more detail in Section 8.

⁹In particular, ID#55 could be a misidentification because there is a secondary counterpart, see E09.

The 24 μm -selected sample described by Le Floc'h et al. (2005) most resembles our $z \leq 0.9$ sample in terms of $L_{\text{FIR}}-z$ parameter space, although our objects are in general more massive, as we will see in Section 8. This, in combination with Figure 5, points to the conclusion that the BLAST counterparts detected in this survey at $z \lesssim 1$ are mostly run-of-the-mill star-forming galaxies. Finally, given the steep number counts at the BLAST wavelengths (Patanchon et al. 2009) and the smaller beam sizes of *Herschel*, we expect SPIRE to detect roughly a factor of 10 more sources than BLAST, probing fainter fluxes and therefore higher redshifts. Figure 7 suggest that SPIRE will likely fill the $10^{11} \lesssim L_{\text{FIR}} \lesssim 2 \times 10^{12} L_{\odot}$ region (see e.g. Chapin et al. 2010), but probably will not be dominated by SCUBA-like sources.

6. AGN fraction and quasars

In this section we describe the AGN and quasar content of our sample, and we investigate whether the submm emission that we see with BLAST is mainly due to the host galaxy or to the active nucleus.

AGN are identified using spectroscopic and photometric methods, and the information is listed in Table B1. Of the 82 sources in our sample with optical spectra, 56 have a measurement of the line ratio $[\text{NII}]/\text{H}\alpha$; 14 of these have $[\text{NII}]/\text{H}\alpha \gtrsim 0.6$ and we flag them as AGN (Kauffmann et al. 2003; Miller et al. 2003, and references therein). Broad emission lines, such as $\text{CIII}]$ 190.9 and CIV 154.9, which appear in the accessible waveband at $z > 1$, are used to identify 5 additional sources as quasars. A search on NED yields that 10 more sources in our sample are classified as AGN by other authors.

Active galaxies can also be identified using a number of photometric empirical methods. Quasars occupy a distinct region in the IRAC color space by virtue of their strong, red continua in the MIR (Lacy et al. 2004). IRAC fluxes are available for 205 sources and we use the 3 color-color cut prescriptions of Hatziminaoglou et al. (2005), Stern et al. (2005) and Marsden et al. (2009). Optical magnitudes and postage stamp images are also available for 114 sources, along with radio fluxes for 107 sources from D09. A source is considered a quasar when it is compact¹⁰ and satisfies the 3 aforementioned color-color cut prescriptions. If only 2 color-color cuts prescriptions are satisfied, we also require the source to be either radio-loud ($L_{1.4\text{GHz}} \gtrsim 10^{39} \text{ W}$), optically bright ($L_{U/g} \gtrsim 10^{11} L_{\odot}$), or one of the 10 NED AGN.

Using these empirical methods, we find 24 quasars plus 10 additional sources showing weaker yet significant quasar activity, when the above conditions are near the threshold. The 5 quasars identified spectroscopically are

all contained in this photometric list. Of the 14 spectroscopically identified AGN, 10 are definitely not compact, but rather spiral in shape (see next Section on morphology), and mostly radio-quiet. We believe that these objects are Seyfert galaxies (e.g. Cid Fernandes et al. 2010).

In conclusion, we have assessed that about 15% of the galaxies in our sample show strong indication of having an active nucleus and an additional 6% have weaker yet significant evidence. Chapin et al. (2010) found a comparable proportion¹¹ of sources with excess radio and/or MIR that can be interpreted as an AGN signature. Several recent observations find close association of AGN activity and young star formation (Silverman et al. 2009), consistent with a scenario in which the FIR/submm emission is mainly due to star formation ongoing in the host galaxy, rather than to emission from a dusty torus obscuring the inner regions of the active nucleus (Wiebe et al. 2009; Coppin et al. 2010; Muzzin et al. 2010; Hatziminaoglou et al. 2010; Shao et al. 2010; Elbaz et al. 2010). In addition, our AGN selection criteria, which use optical and MIR data, tend to favor type-1 AGN, i.e. unobscured Seyfert galaxies and quasars. This is definitely the case for the IRAC color-color selection methods, as reported by Hatziminaoglou et al. (2005) and Stern et al. (2005), but it is also corroborated by the fact that most of the quasars we have identified are optically bright. We aim to address this issue in greater detail in a future paper.

7. Morphology

We have assigned a broad morphological classification to 137 (60%) of the BLAST IDs presented in this paper, based upon visual inspection of UV, optical and MIR postage stamp images (see Section 2.5) centered at $[\alpha_{\text{BLAST}}, \delta_{\text{BLAST}}]$. A selection of cut-outs is shown in Figure A1.

In addition to the visual examination of the multi-wavelength images, we corroborated our choice with ancillary information (when available), such as: (a) location on the color-magnitude diagram, typically $(U-r)$ vs M_r ; (b) spectral features; (c) UV detection; (d) FIR luminosity. Our findings are listed in the “morphology” column in Table B1 and summarized in Table 2.

At low redshift we find predominantly spirals, whereas most of the BLAST sources identified at high redshift are compact and show AGN signatures. This is probably a selection bias, as the fraction of submm sources identified at other wavelengths is known to gradually decreases with z (see D09), and the most distant sources are often identified only thanks to their extreme radio and/or optical emission, due to the AGN. In fact, the study by Dunlop et al. (2010) shows that a deep survey

¹⁰By “compact” we mean objects unresolved in the optical and MIR, with linear sizes $\lesssim 3 \text{ kpc}$ at $z \gtrsim 1$.

¹¹Only sources with a redshift estimate.

TABLE 2
BROAD MORPHOLOGICAL CLASSIFICATION OF BLAST IDs

type	sub-type	number	frequency
spiral		69	50%
	Seyfert	8	6%
compact		52	38%
	quasar	31	23%
	blue compact	5	4%
elliptical	red compact	3	2%
		8	6%
interacting system		7	5%
irregular		1	<1%

NOTE.—Morphological classification available for 137 out of 227 BLAST IDs (60%), based upon visual inspection of UV, optical and mid-IR (MIR) postage stamp images (see Section 2.5). By “compact” here we mean objects unresolved in the optical and MIR, with linear sizes $\lesssim 3$ kpc. By “interacting system” we mean a visually obvious physical association of two or more objects.

at $250\mu\text{m}$ not only reveals low- z spirals, but also extreme dust-enshrouded starburst galaxies at $z \sim 2$. The latter tend to be missed in our selection, because they are typically extremely faint in the optical/UV, unless they also host an AGN.

We point out here that this broad morphological scheme should not be regarded as meaningful on a source-by-source basis, but rather be considered as guidance for interpreting the other results of this paper. For this purpose, we encoded the morphological information in Figures 5, 7, 8, 9 and 10.

8. Stellar masses

Stellar masses (M_\star) are computed by Dye et al. (2010b) for a subset of 92 sources in our sample with counterparts in a minimum of 5 bands, from the optical to NIR. The distribution has median of $10^{10.9} M_\odot$, and inter-quartile range of $10^{10.6} - 10^{11.2} M_\odot$.

These stellar masses are plotted vs. redshift in Figure 8; we also show for comparison the stellar masses of SCUBA sources in SHADES, computed by Dye et al. (2008) using a methodology and photometry almost identical to ours.

Except for 3 outliers (that may well be misidentifications as they all lie in BGS-Deep), the monotonic trend of increasing stellar masses is the result of multiple selection effects; sources at a given redshift are not detected with arbitrarily low, or arbitrarily high stellar masses. As

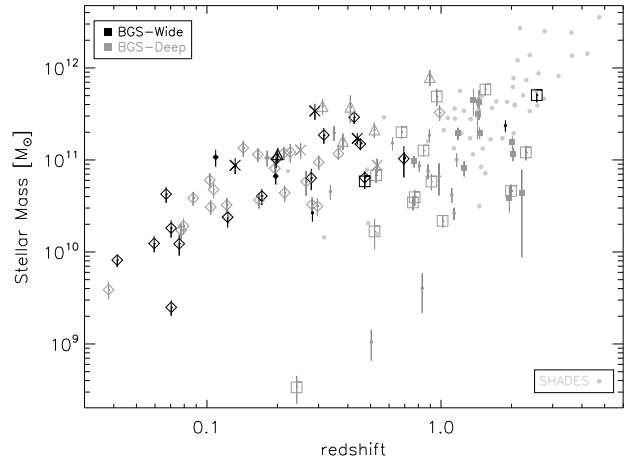


Fig. 8.— Stellar mass as a function of redshift for the whole subset of 92 sources described in Section 8. Symbols are as in Figure 5. Filled squares indicate that the source is a quasar. We overplot SHADES sources (Dye et al. 2008) as light gray filled circles.

we discuss later in this section, there is an approximately constant relation between L_{FIR} and stellar masses in our sample. Low-luminosity sources (with low stellar masses) are excluded at a given redshift because of sensitivity. On the other hand, sources with L_{FIR} (and stellar masses) above a certain threshold are excluded from our sample despite the well-documented strongly evolving FIR luminosity function (E09; Dye et al. 2010a; Eales et al. 2010); our present study simply does not go deep enough to start detecting the bulk of high- z (and higher volume density) k -corrected sources. In particular, sources with $M_{\star} \gtrsim 10^{12} M_{\odot}$, which are present in the SHADES sample, are absent from ours. Indeed, these very massive sources are not detected among 24 μm -selected samples, down to a flux density level of $\sim 20 \mu\text{Jy}$ (GOODS survey, see e.g. Le Floc'h et al. 2005; Pérez-González et al. 2005; Caputi et al. 2006; Elbaz et al. 2007; Santini et al. 2009)¹². The 24 μm catalog used by D09 to find counterparts to the BLAST sources goes down to the same depth, therefore we are only left with the radio catalogs. It is indeed possible that our analysis is missing very massive galaxies that, though having a radio ID, do not have an estimate of stellar mass because measurements are not available in a minimum of 5 optical/NIR bands. An accurate account of the selection effects at work for $M_{\star} \gtrsim 10^{12} M_{\odot}$, which is beyond the scope of this work, would not invalidate the results of the rest of this paper.

Our subsample is composed of relatively massive objects, with a significant fraction of sources (45%) with stellar masses greater than $10^{11} M_{\odot}$. This fraction soars to 84% in the SHADES survey, whereas the majority of sources detected at 24 μm in deep surveys of the CDFS (down to a flux density level of $\sim 20 \mu\text{Jy}$) have $M_{\star} \leq 10^{11} M_{\odot}$ (e.g. Le Floc'h et al. 2005; Pérez-González et al. 2005; Caputi et al. 2006; Elbaz et al. 2007; Santini et al. 2009). However, a direct comparison of the detection rates of massive galaxies among these surveys is very difficult because of the dissimilar comoving volumes probed; in fact, BLAST samples a volume roughly 14 (57) times larger than SHADES (GOODS)¹³. Furthermore, it would be necessary to quantify the numerous selection effects and the different shape of the stellar mass function at the wavelengths in question.

¹²All the authors cited above adopt a Salpeter (1955) IMF. Caputi et al. (2006), Santini et al. (2009), Dye et al. (2008, 2010b) estimate the stellar masses by means of an optical-to-NIR SED fit of each galaxy at the determined redshift. Le Floc'h et al. (2005) and Pérez-González et al. (2005) simply convert, respectively, V - and K -band luminosities into stellar masses. Finally, Elbaz et al. (2007) compute stellar masses by modeling the stellar populations of each galaxy using stellar absorption-line indices.

¹³Based on the following redshift depth and sky area covered by, respectively, the GOODS survey, the SHADES survey and the present BLAST study: $\sim 140 \text{ arcmin}^2$ out to $z \sim 3$; $\sim 320 \text{ arcmin}^2$ out to $z \sim 5$; and $\sim 4.15 \text{ deg}^2$ out to $z \sim 2$.

Nevertheless, BLAST observes a significant number of large, massive and actively star-forming galaxies (typically spirals, see Section 7), which qualitatively appear to link the 24 μm and SCUBA populations at $0 < z < 2$. With the deep 24 μm GOODS survey, other authors seem to be already detecting this linking population (in particular Caputi et al. 2006 and Elbaz et al. 2007), but their most massive sources at $0 < z < 1$ all have long ($\geq 4 \text{ Gyr}$) star-formation time scales (defined as the ratio of already assembled stellar mass over the recent SFR, see later in this section), indicating prolonged star formation histories. On the contrary, about 60% of our galaxies in the same $M_{\star}-z$ range have star-formation time scales shorter than 4 Gyr, consistent with the findings that submm-selected $M_{\star} \gtrsim 10^{11} M_{\odot}$ systems at $z \geq 0.5$ form their stellar mass predominantly at late and at early times, but less so when the galaxies are middle-aged (Dye et al. 2010b, 2008). These figures indicate that the moderately massive population detected at $0 < z < 1$ by BLAST is more actively forming stars than the equally massive 24 μm -selected galaxies in the same redshift range. One might wonder whether this observation arises just as a consequence of a selection effect in the shallower BLAST sample; although our data do not allow us to investigate the stellar masses of fainter BLAST galaxies, a thorough examination of the M_{\star} distribution at $0 < z < 1$ in the GOODS survey (e.g. Fig. 7 of Caputi et al. 2006) does not suggest that the exclusion of the fainter 24 μm sources (below e.g. $83 \mu\text{Jy}$, the 80% completeness limit in the CDFS) would dramatically alter the proportions of galaxies with stellar mass above and below $10^{11} M_{\odot}$. It is certainly possible that a cut at a brighter 24 μm flux density would bias high the detection rate of massive galaxies; however, the massive BLAST galaxies at $z \leq 1$ have a median SFR of $\sim 70 M_{\odot} \text{ yr}^{-1}$ that equals the maximum SFR among the likewise massive and aged galaxies in GOODS. This would still be true if the 24 μm sample were shallower.

Moreover, Figure 8 exhibits, in the range $1 < z < 2$, a substantial overlap between BLAST and SCUBA sources. Therefore, assuming that the BGS is a representative field, our data suggest that the BLAST galaxies seem to connect the 24 μm and SCUBA populations, in terms of both stellar mass and star-formation activity. Figures 9 and 10 further corroborate this conclusion. It is worth reminding the reader that the M_{\star} estimates are based on the optical/NIR fluxes of BLAST IDs and do not employ any BLAST-specific photometric data.

Figure 9 plots stellar masses (top panel) and SSFR_{tot} (bottom panel) vs. L_{FIR} for the subset of 55 sources at $z \leq 0.9$ that have an estimate of both these quantities. There are 37 additional sources in our catalog with $L_{\text{FIR}} \gtrsim 10^{11} L_{\odot}$ and stellar mass estimates, but no reliable SFR_{NUV} . These are included in Figure 9, because in this case $\text{SFR}_{\text{tot}} \simeq (1 - \eta) \text{SFR}_{\text{dust}}$ (see Sec-

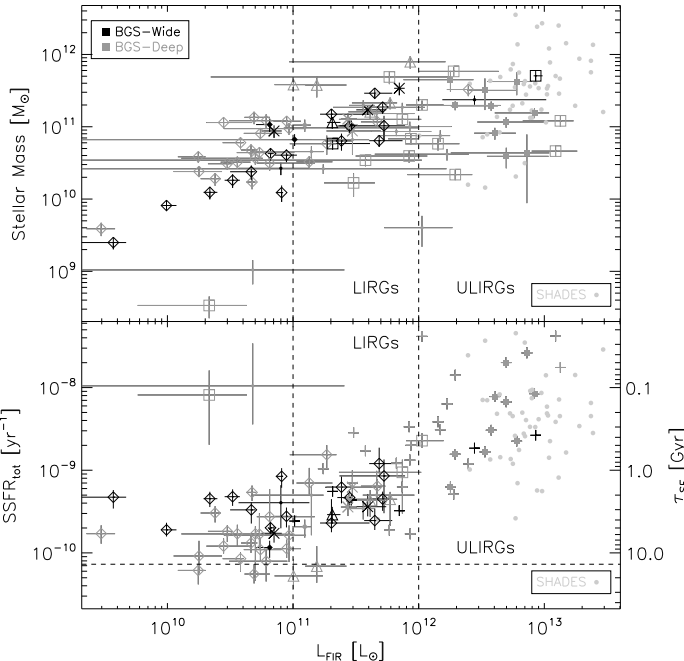


Fig. 9.— Top panel: stellar mass as a function of FIR luminosity for the whole subset of 92 sources described in Section 8. Bottom panel: specific total SFR (SSFR_{tot}) as a function of FIR luminosity for the subset of 55 sources at $z \leq 0.9$ that have an estimate of SFR_{tot} . Symbols are as in Figure 5. For the remaining 37 sources, we assume $\text{SFR}_{\text{tot}} = (1 - \eta) \text{SFR}_{\text{dust}}$ as they all have $L_{\text{FIR}} \gtrsim 10^{11} L_{\odot}$; these are shown as crosses without error bars. The right-hand ordinate shows the corresponding star-formation time scales, defined as $\tau_{\text{SF}} = \text{SSFR}^{-1}$. Filled squares indicate that the source is a quasar. The horizontal dashed line shows the inverse of the age of the Universe. We overplot in both panels SHADES sources (Dye et al. 2008) as light gray filled circles.

tion 5). SHADES sources are also shown in this figure. Dye (2010) estimates their FIR luminosities using a two-component SED fit from Dunne & Eales (2001) that has cold/hot ratio of 186, with $T_{\text{hot}} = 44$ K and $T_{\text{cold}} = 20$ K. SFRs are estimated using Equation 1 and corrected by $(1 - \eta)$. Finally, star-formation time scales, defined as $\tau_{\text{SF}} = \text{SSFR}^{-1}$, are shown as secondary y -axis.

BLAST IDs selected in BGS-Wide show a positive correlation between their stellar masses and L_{FIR} , but there is no strong evidence for a correlation between SSFR_{tot} and FIR luminosities. Although BLAST IDs selected in BGS-Deep appear to have different trends, one should be cautious as they are, in general, less reliable than the IDs in BGS-Wide. However, BGS-Deep sources can be used to study bulk properties under appropriate caveats. The emerging picture appears to confirm Figure 8, in which there is a non-negligible overlap between the BLAST and SCUBA populations in the range $1 < z < 2$. In particular, the high luminosity tail of the BLAST sample appears to encroach on the SHADES sources in terms of both L_{FIR} and M_{\star} , bridging the gap with the lower-redshift Universe populated by $24 \mu\text{m}$ sources and by run-of-the-mill star-forming BLAST galaxies, with τ_{SF} spanning the interval 1–10 Gyr. A considerable overlap between fainter BLAST sources and $870 \mu\text{m}$ -selected galaxies has already been established by Dunlop et al. (2010) and Chapin et al. (2010), but it is important to have confirmed an additional, less direct, connection with our shallower BLAST sample, by means of a comparable analysis to that of SHADES.

We have investigated if a temporal connection between the two populations is allowed by the data, in a scenario where the BLAST sources are SCUBA sources fading at the end of their late star-formation burst (Borys et al. 2005; Dye et al. 2008). However, Dye et al. (2010b) seem to rule out this possibility, because the higher- z , more massive BLAST IDs are observed during a star-formation burst lasting too briefly in redshift to allow this connection. This disconnection is consistent with the phenomenon of downsizing observed in optically-selected samples of galaxies (e.g. Heavens et al. 2004).

The approximately flat trend between SSFR_{tot} with FIR luminosity of Figure 9 evidenced by the BLAST IDs selected in BGS-Wide is consistent with Serjeant et al. (2008). The inclusion of BGS-Deep sources at high FIR luminosities seems to suggest a different, mild trend of increasing SSFR_{tot} , also reported by Santini et al. (2009) and Rodighiero et al. (2010). The data available to us do not manifest enough evidence to support either scenario. Larger samples now accessible with *Herschel* will shed more light on the evolution of the specific star-formation rate.

In Figure 10, we plot SSFR_{tot} vs. stellar mass, for

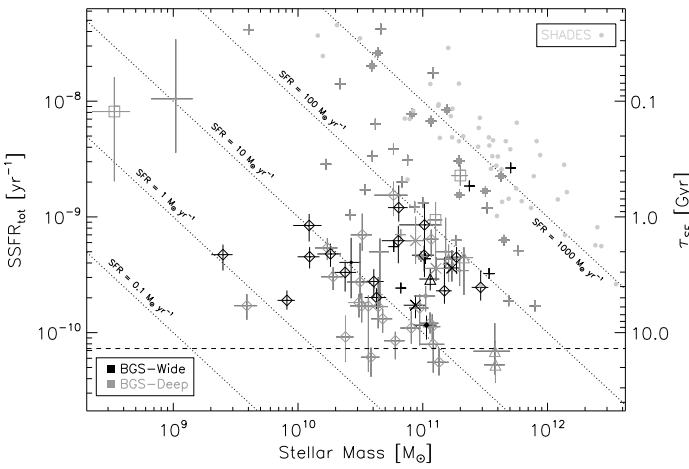


Fig. 10.— Specific total SFR (SSFR_{tot}) as a function of stellar mass for the subset of 55 sources at $z \leq 0.9$ that have an estimate of SFR_{tot}. Symbols are as in Figure 5. For the remaining 37 sources, we assume SFR_{tot} = $(1-\eta)$ SFR_{dust} as they all have $L_{\text{FIR}} \gtrsim 10^{11} L_{\odot}$; these are shown as crosses without error bars. The right-hand ordinate shows the corresponding star-formation time scales, defined as $\tau_{\text{SF}} = \text{SSFR}^{-1}$. Dotted isolines correspond to constant SFRs, under the assumption that M_{\star} is the galaxy's total stellar mass. The horizontal dashed line shows the inverse of the age of the Universe. We overplot SHADES sources (Dye et al. 2008) as light gray filled circles.

BLAST and SHADES sources. The dotted isolines correspond to constant SFRs, under the assumption that M_{\star} is the galaxy's total stellar mass. We do not find any clear correlation between specific total star-formation rate and stellar mass, which is not surprising as we are sampling a population of young, active, star-forming galaxies (see also Santini et al. 2009). Expectedly, the bulk of SHADES sources occupies a well-defined region of the plane, around the isoline of $\text{SFR} = 1000 M_{\odot} \text{ yr}^{-1}$, whereas practically all the BLAST counterparts at $z \leq 0.9$ lie below the isoline of $\text{SFR} = 100 M_{\odot} \text{ yr}^{-1}$. The gap is again filled by the BLAST IDs at higher redshift.

We can compare our results in Figure 10 with Buat et al. (2008), who derived mean relationships between observed SSFR and stellar mass at $z = 0$ and $z = 0.7$, and confronted these with models based on a progressive infall of gas into the galactic disk, starting at high z . Both their data and models exhibit a flat distribution of SSFR for galaxies with masses between 10^{10} and $10^{11} M_{\odot}$. Our $z \leq 0.9$ subset of star forming galaxies shares a similar behavior, as well as the dynamic ranges. On the other hand, we can also compare the high- z tail of the BLAST IDs with the $z > 0.85$ sample of Rodighiero et al. (2010): although the scatter is quite large in both subsets, we observe the same negative trend of SSFR with M_{\star} , again consistent with downsizing.

The in-depth analysis of the bright BLAST counterparts reveals a population with an intrinsic dichotomy in terms of star-formation rate, stellar mass and morphology. The bulk of BLAST counterparts at $z \lesssim 1$ appear to be run-of-the-mill star-forming spiral galaxies, with intermediate stellar masses (median $M_{\star} \sim 7 \times 10^{10} M_{\odot}$) and approximately constant specific star-formation rates (τ_{SF} in the range 1–10 Gyr); in addition, they form stars more actively than the equally massive and aged 24 μm sources. On the other hand, the high- z BLAST counterparts significantly overlap with the SCUBA population, and the observed trends of SSFR, albeit inconclusive, suggest stronger evolution and downsizing. In conclusion, our study suggests that the BLAST galaxies may act as linking population between the star-forming 24 μm sources and the more extreme SCUBA starbursts.

9. Concluding remarks

We have carried out a panchromatic study of individual bright BLAST galaxies identified at other wavelengths, extending the analysis of previous BLAST papers. Our basic results are as follows.

1. The flux densities of BLAST sources are boosted due to a combination of Eddington bias, source confusion and blending. We have developed a Monte Carlo method to quantify these biases, both in confusion-limited maps and in maps dominated

by instrumental noise. The boosting effects are more pronounced in the confusion-limited regime, and become more important as the wavelength increases. In addition, flux densities are heavily correlated among the BLAST bands, again more prominently in BGS-Deep. We account for all these effects coherently while calculating the FIR luminosities of BLAST galaxies. We have also shown how crucial the BLAST/SPIRE photometry is to estimate without bias the FIR luminosity of a galaxy, especially at high redshift.

2. We have measured that star formation is predominantly obscured at $L_{\text{FIR}} \gtrsim 10^{11} L_{\odot}$, $z \gtrsim 0.5$. On the other hand, unobscured star formation is important at $L_{\text{FIR}} \lesssim 10^{11} L_{\odot}$, $z \lesssim 0.25$ and FIR-only evaluations of SFR would lead to underestimates up to a factor of 2. This is probably a direct consequence of the well documented stronger evolution of the FIR luminosity density with respect to the optical-UV one.
3. We have compared, in terms of $L_{\text{FIR}}-z$ parameter space, the BLAST counterparts to the *IRAS*/FIR-selected sample of local galaxies, to the $24 \mu\text{m}$ -selected sample observed by *Spitzer*, and to the SCUBA $850 \mu\text{m}$ -selected sample. The overlap with the local *IRAS* sample is minimal and this conclusion should not be belittled by the extent of local volume surveyed by BLAST. Similarly, our sample lacks the abundance of most luminous IR galaxies detected in the SHADES survey, but the high- L_{FIR} , high- z tail of the BLAST counterparts seems to overlap with the SCUBA population. The $24 \mu\text{m}$ -selected sample resembles the most the bulk of BLAST IDs in terms of L_{FIR} and redshift distribution.
4. We have assessed that 15% of the galaxies in our sample show strong indication of an active nucleus and an additional 6% have weaker yet significant evidence. In particular, these are predominantly type-1 AGN, i.e. unobscured Seyfert galaxies and quasars. The AGN fraction and the SFRs inferred for these objects are comparable to recent observations at similar wavelengths and point to a scenario in which the submillimeter emission detected by BLAST is mainly due to star formation ongoing in the host galaxy, rather than to emission from a dusty torus obscuring the inner regions of the active nucleus.
5. We have computed stellar masses for a subset of 92 BLAST counterparts. These appear to be relatively massive objects, with median mass of $10^{10.9} M_{\odot}$, and inter-quartile range of $10^{10.6}-10^{11.2} M_{\odot}$. In particular, a significant fraction of them fill the region of $M_{\star} \sim 10^{11} M_{\odot}$ at $z \lesssim 1$ that is practically vacant in the SCUBA surveys,

and sparsely populated by $24 \mu\text{m}$ -selected samples. Although the dissimilar volumes sampled by these surveys discourage a direct comparison of the detection rates of massive galaxies, our study suggest that the BLAST counterparts seem to link the $24 \mu\text{m}$ and SCUBA populations, in terms of both stellar mass and star-formation activity.

6. We have highlighted a dichotomy in the BLAST population in terms of star-formation rate, stellar mass and morphology. The bulk of BLAST counterparts at $z \lesssim 1$ are run-of-the-mill star-forming galaxies, typically spiral in shape, with intermediate stellar masses and nearly constant specific star-formation rates. On the other hand, the higher redshift BLAST counterparts significantly overlap with the SCUBA population, and the observed trends of SSFR, albeit inconclusive, suggest stronger evolution. Other BLAST studies have already described the significant overlap existing between fainter BLAST sources and $870 \mu\text{m}$ -selected galaxies, but here we have established an additional link with a shallower BLAST sample, via an analysis equivalent to that of SHADES.

7. We rule out a temporal connection between the BLAST and SCUBA populations, in a scenario where BLAST sources would correspond to SCUBA galaxies whose burst of star formation is ceasing. This disconnection is consistent with the downsizing observed in optical samples.

The findings described in this paper represent a taste of what should be possible with a significantly larger sample of sources. The increased sensitivity and resolution of the *Herschel* Space Observatory, which recently started operation, will soon provide vastly increased numbers of sources. This will enable significantly reduced uncertainties and therefore much improved constraints on models of galaxy evolution and formation. Nevertheless, the BLAST data have provided a very valuable benchmark for the *Herschel* data and the various analyses that will emerge for some time to come. Furthermore, the results in this paper probably will not immediately become obsolete, as even the much more sensitive SPIRE surveys will have to face the lack of deeper ancillary data, especially in the optical/NIR and in the radio. Identifying the precise location of the submm sources will require either deep and very wide-area VLA data, or a combination of MIPS $24 \mu\text{m}$ and PACS, or ultimately ALMA. Finally, in order to study the rest-frame optical/NIR of the $z > 2$ submm galaxies in much more detail than BLAST or SCUBA, future studies will really require instruments like *WFC3* or *JWST*.

We acknowledge the support of NASA through grant numbers NAG5-12785, NAG5-13301, and NNGO-

6GI11G, the NSF Office of Polar Programs, the Canadian Space Agency, the Natural Sciences and Engineering Research Council (NSERC) of Canada, and the UK Science and Technology Facilities Council (STFC). This paper relies on observations made with the AAOmega spectrograph on the Anglo-Australian Telescope, and we thank the staff of the telescope and especially those involved in the development of the spectrograph. We are grateful to Heath Jones for his help with the observations and Rob Sharp for his help with the *2dfdr* data-reduction pipeline. This work makes use of the *Runz* redshift-fitting code developed by Will Sutherland, Will Saunders, Russell Cannon and Scott Croom, and we are grateful to Scott Croom for making this available to us. This research also made use of the NASA/IPAC Extragalactic Database (NED), operated by the Jet Propulsion Laboratory, under contract with NASA. Finally, this work is based in part on observations made with the *Spitzer* Space Telescope and the Galaxy Evolution Explorer *GALEX*, which are operated by the Jet Propulsion Laboratory, California Institute of Technology under a contract with NASA.

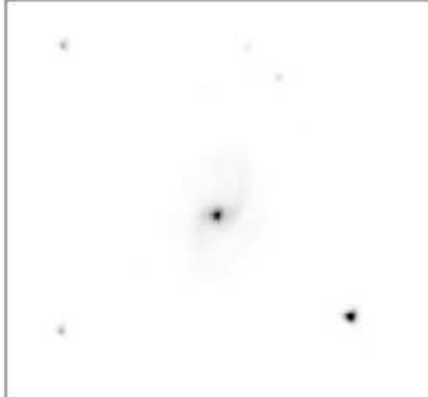
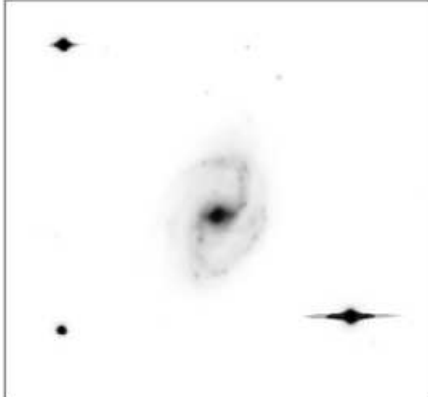
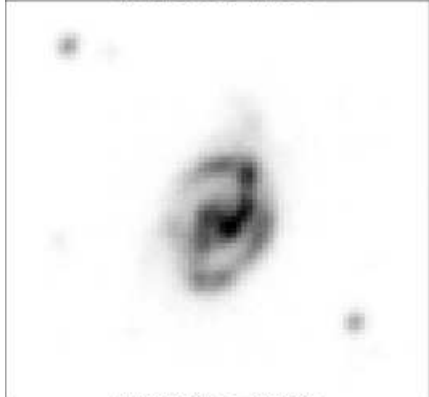
We acknowledge Stefanie Walch, Giorgio Savini, Locke Spencer and Karina Caputi for helpful discussions and comments. We thank David Shupe and Jason Surace for providing the depths of the SWIRE MIPS and IRAC maps of the CDFS. Finally, we thank the anonymous referee for his/her insightful comments and suggestions.

Facilities: BLAST, AAT (AAOmega), *GALEX*, *Spitzer* (MIPS, IRAC)

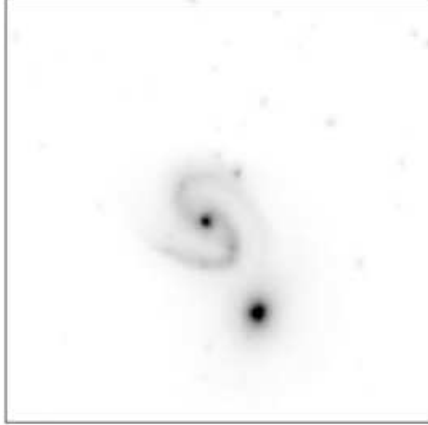
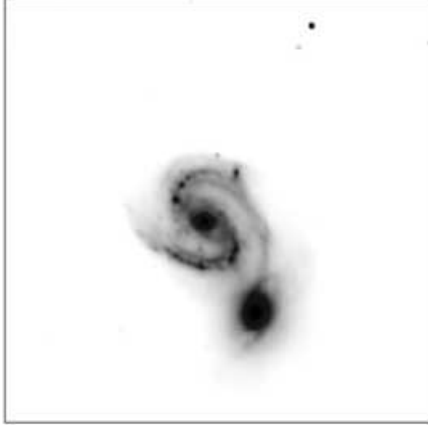
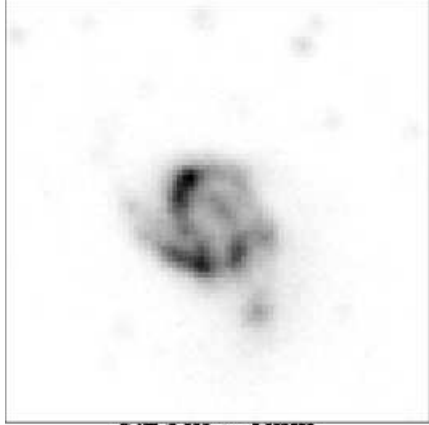
A. Postage stamps

Postage stamp images for a selection of low redshift BLAST IDs. The images are all $2' \times 2'$ in size. Every row shows a BLAST source, imaged at three different bands: *left*, GALEX NUV filter (centered at 2315 Å); *center*, RGB combination of the $U gr$ filters from the SWIRE optical survey; *right*, 3.6 μ m IRAC band. The complete set of full-color cut-outs can be found at http://blastexperiment.info/results_images/moncelsi/

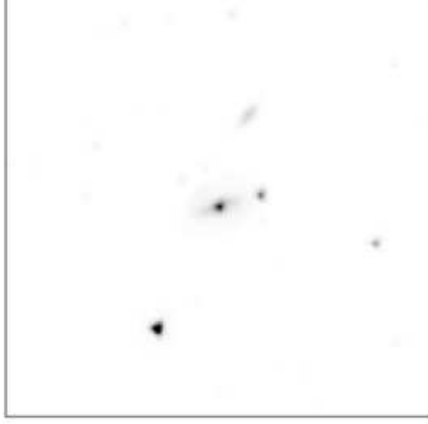
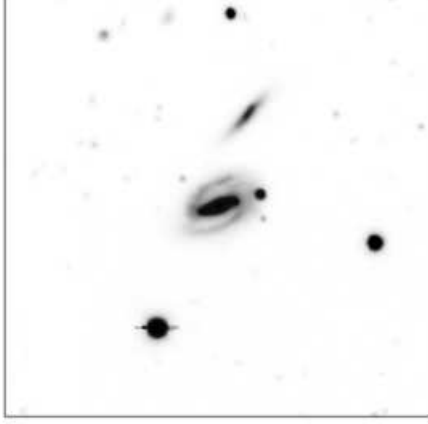
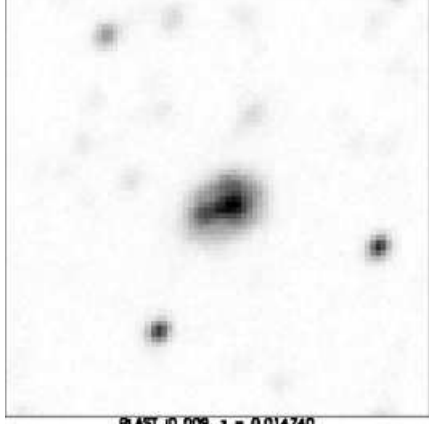
BLAST ID 001, $z = 0.057910$



BLAST ID 002, $z = 0.037000$



BLAST ID 003, $z = 0.060670$



BLAST ID 009, $z = 0.014740$

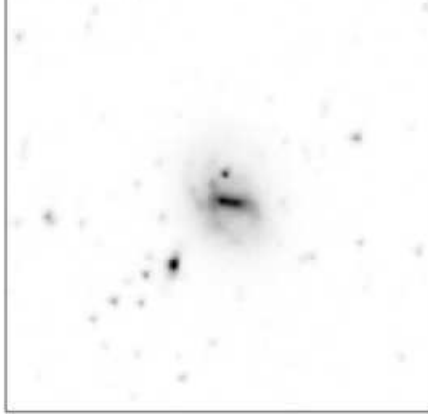
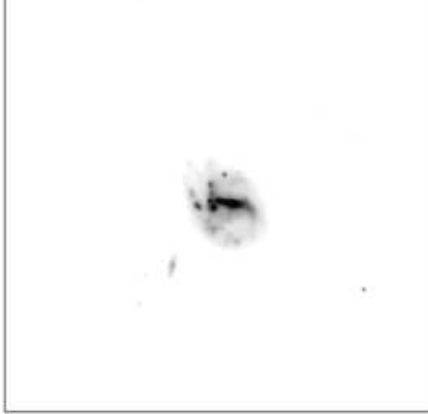
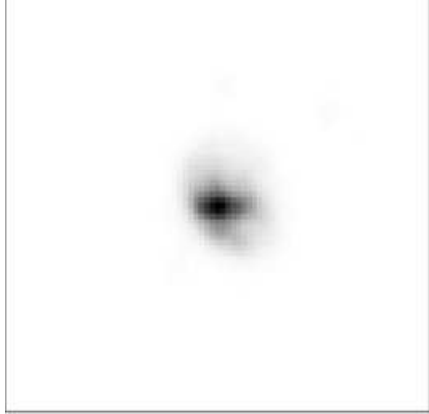
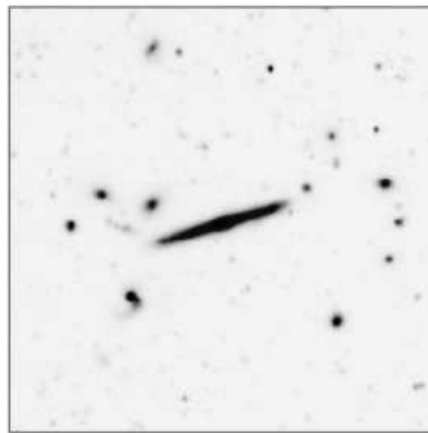
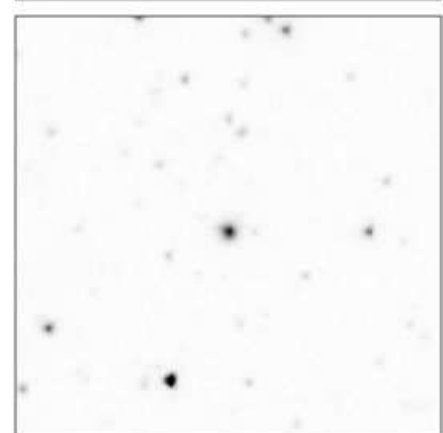
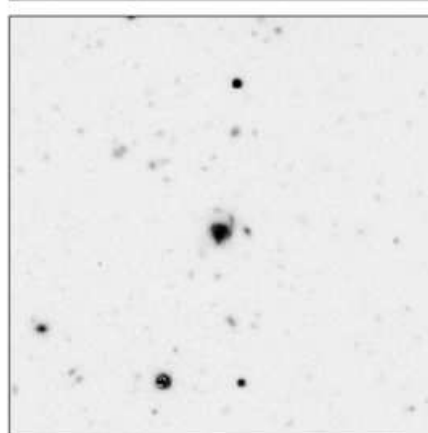
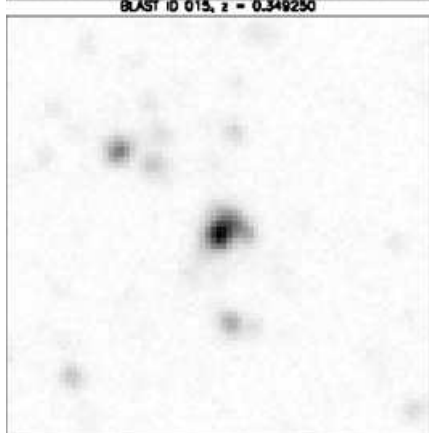


Fig. A1.—

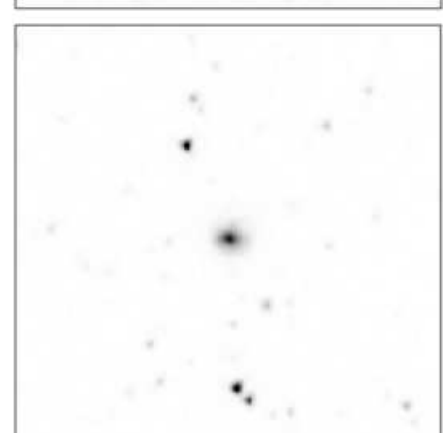
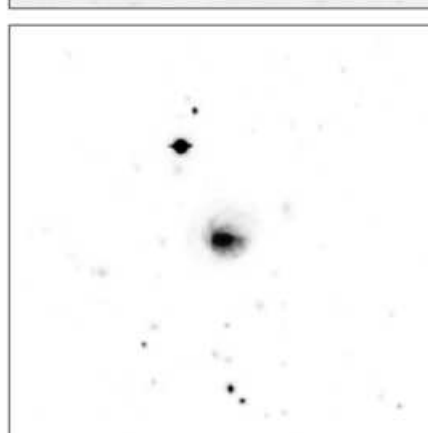
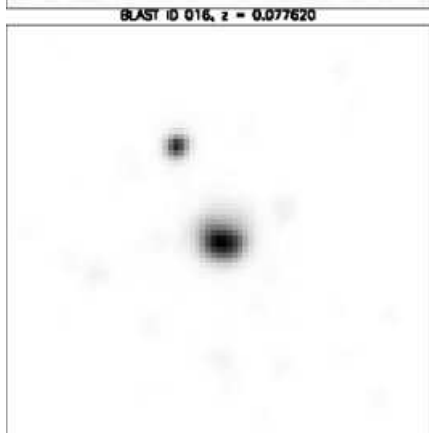
BLAST ID 015, $z = 0.076110$



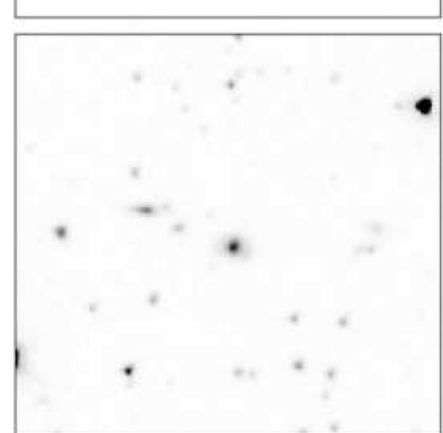
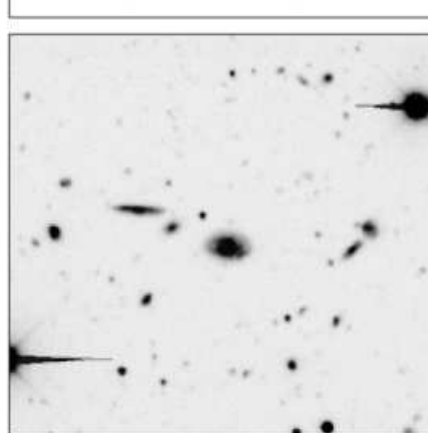
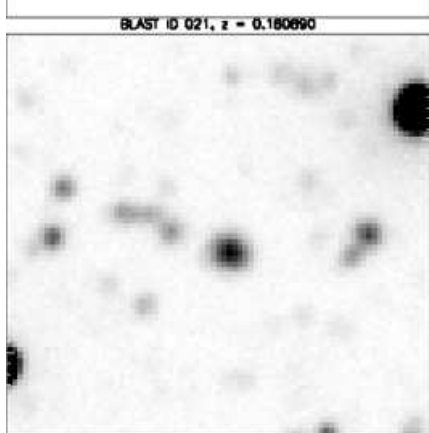
BLAST ID 015, $z = 0.349250$



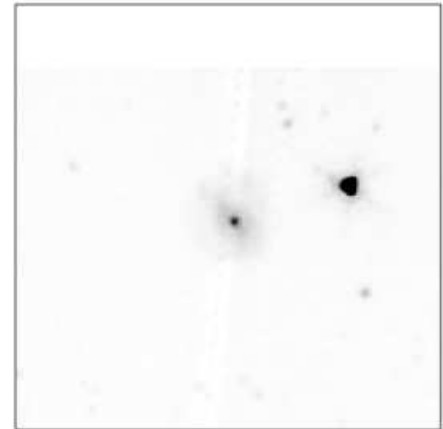
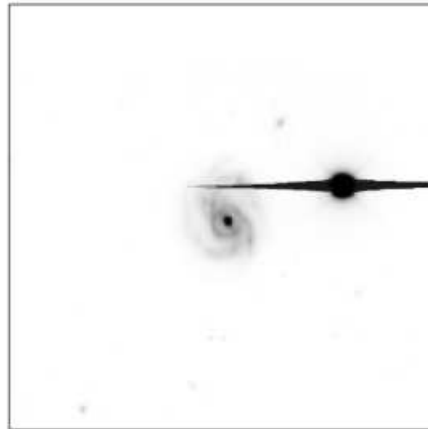
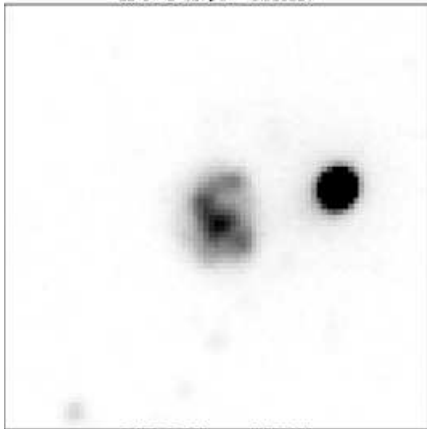
BLAST ID 016, $z = 0.077620$



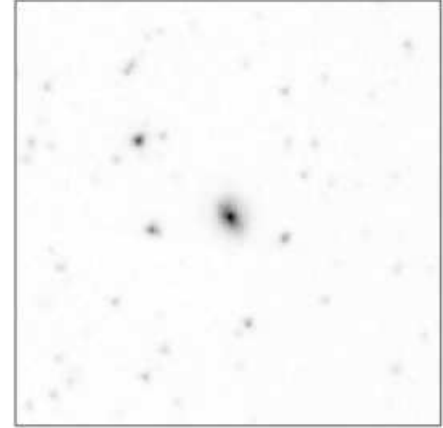
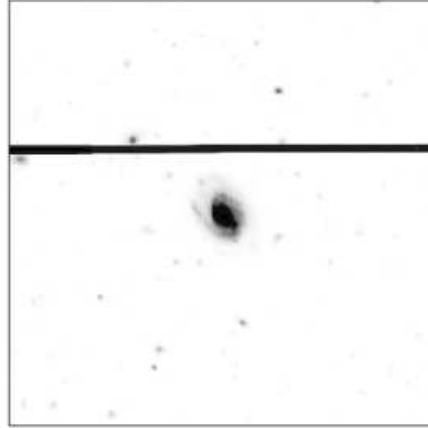
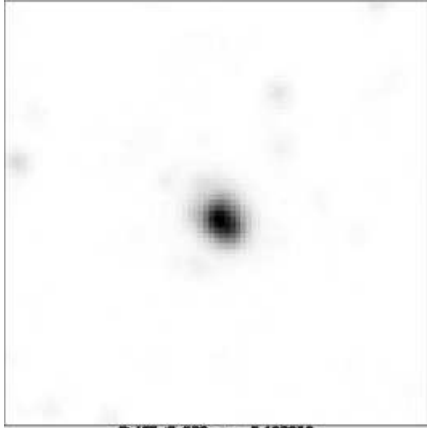
BLAST ID 021, $z = 0.180890$



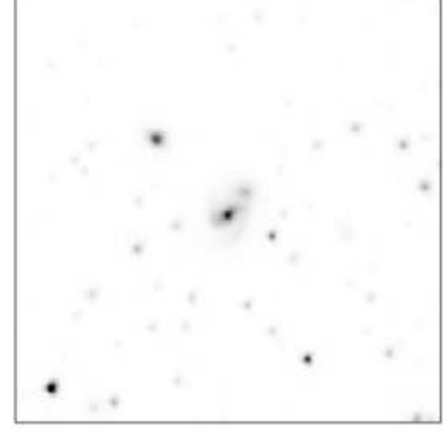
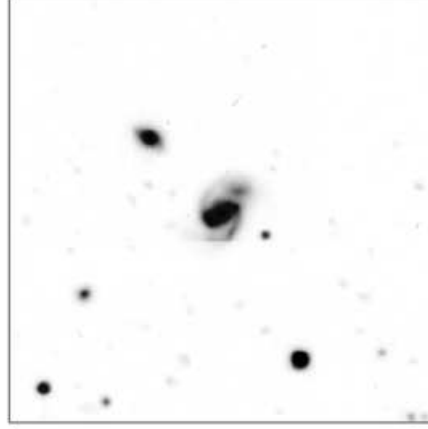
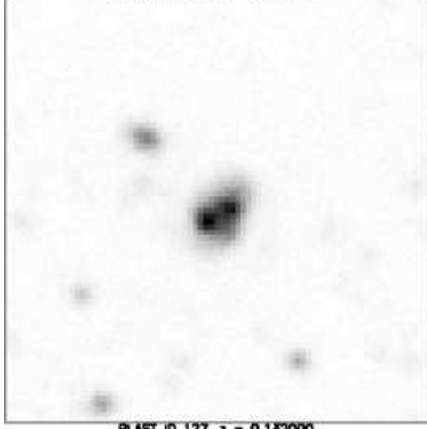
BLAST ID 027, z = 0.059520



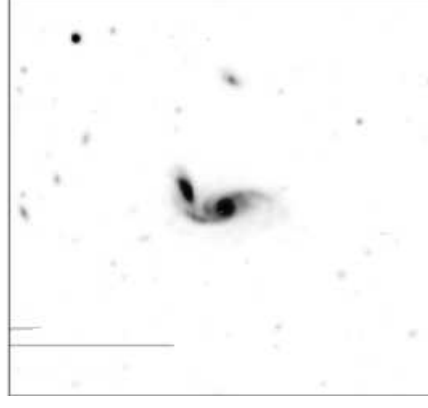
BLAST ID 065, z = 0.079480



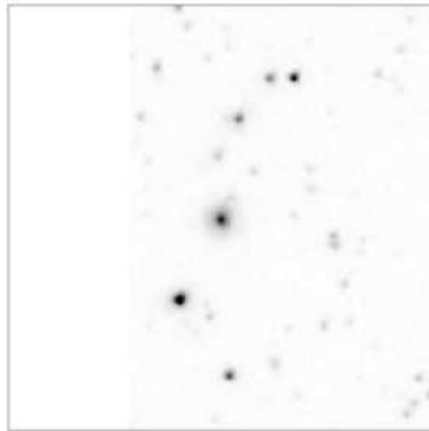
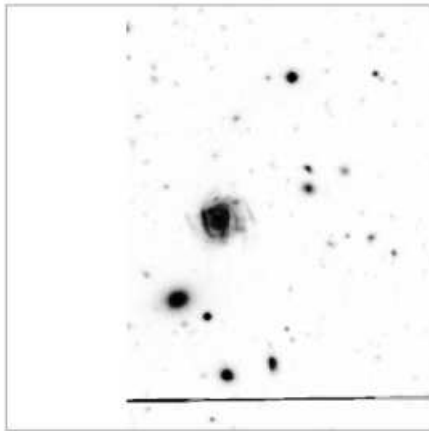
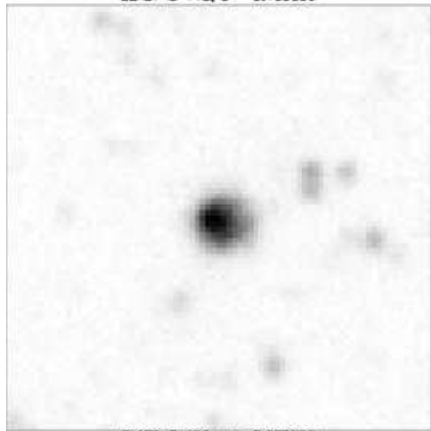
BLAST ID 070, z = 0.108950



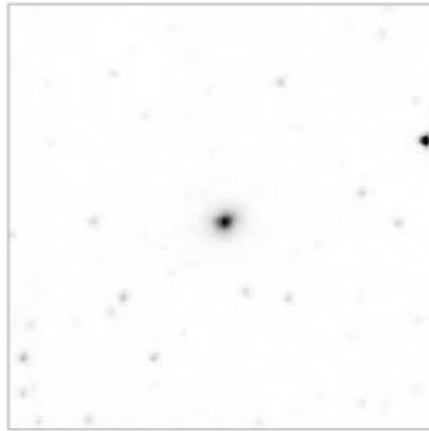
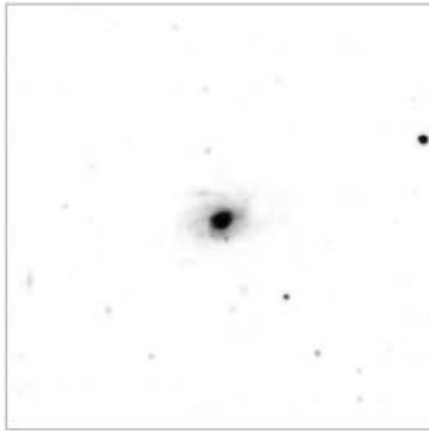
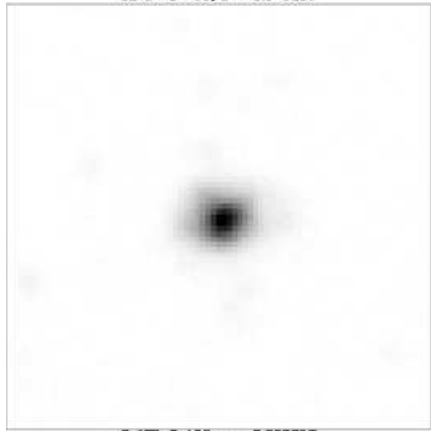
BLAST ID 127, z = 0.132000



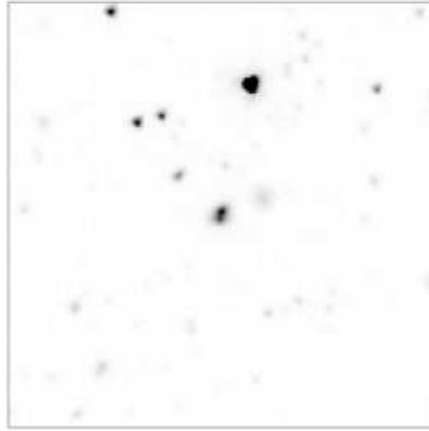
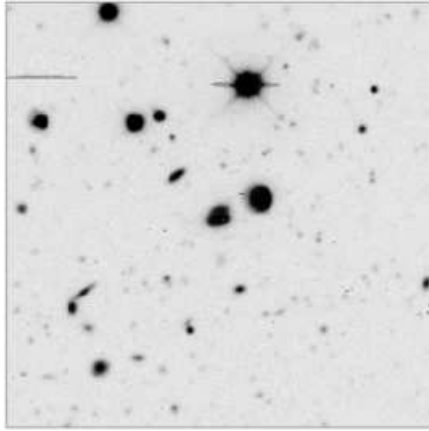
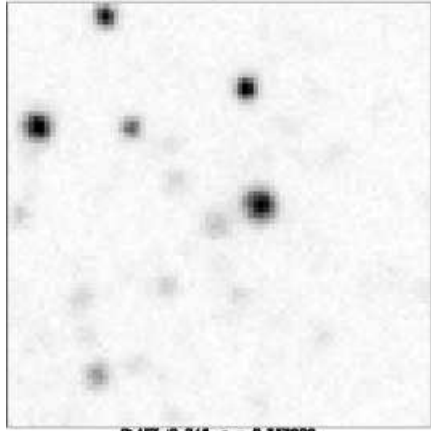
BLAST ID 145, $z = 0.165000$



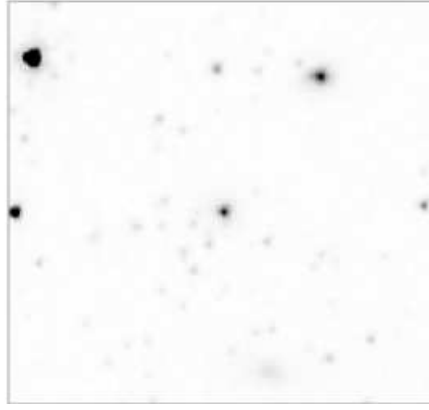
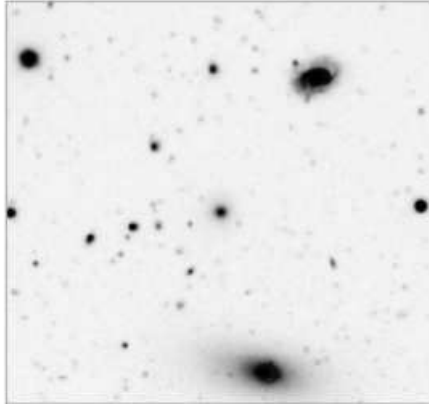
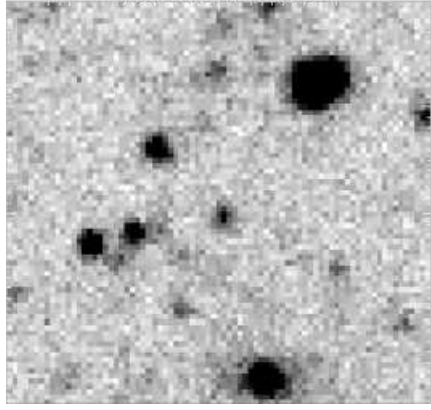
BLAST ID 155, $z = 0.070290$



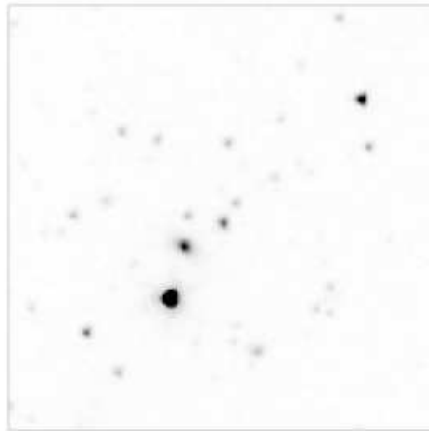
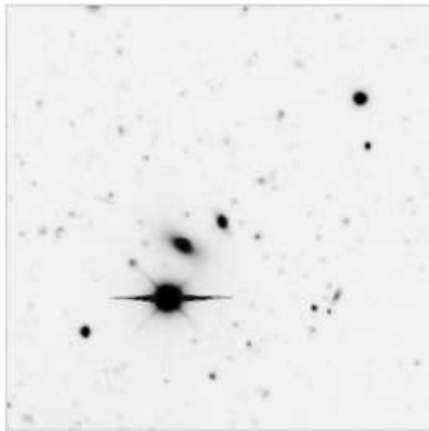
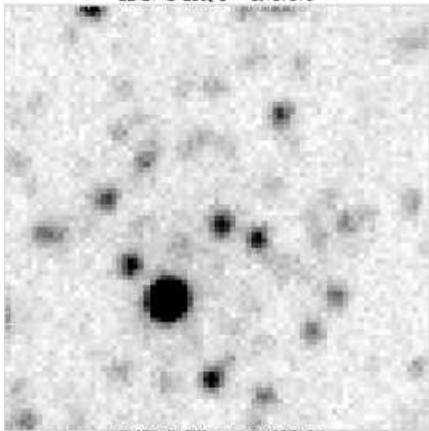
BLAST ID 166, $z = 0.200653$



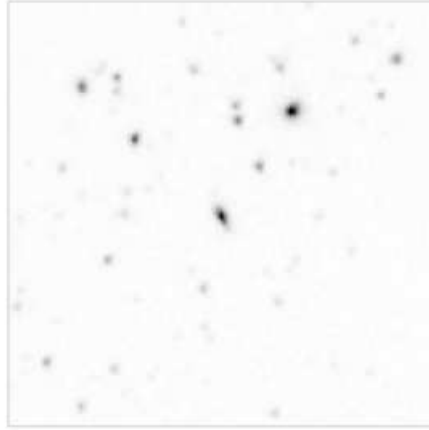
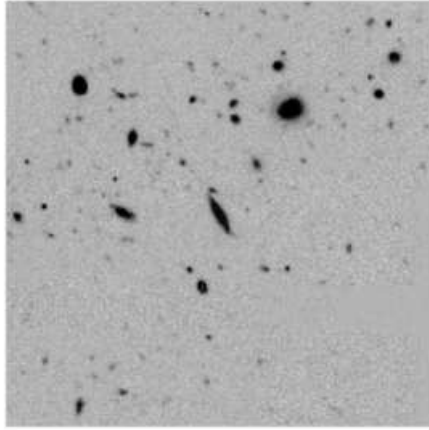
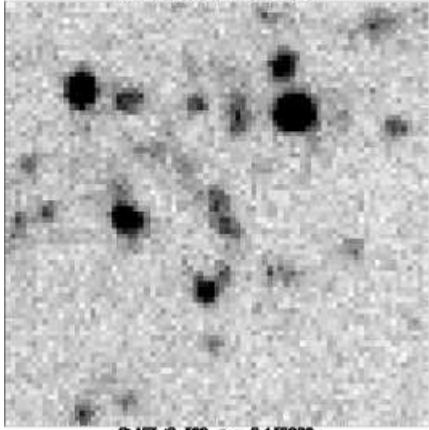
BLAST ID 245, $z = 0.357000$



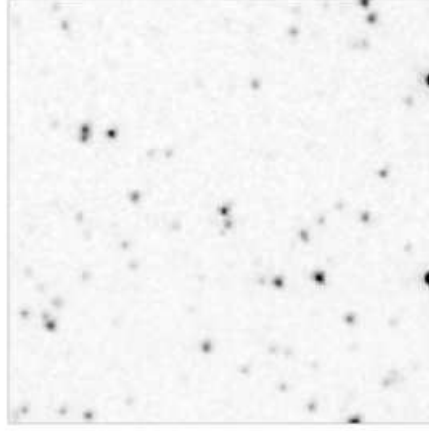
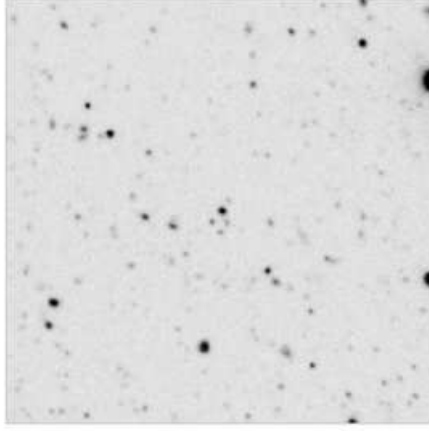
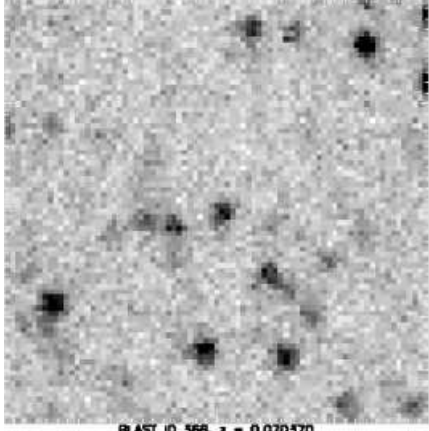
BLAST ID 259, z = 0.167010



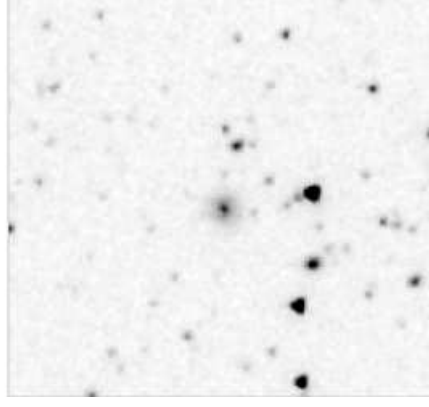
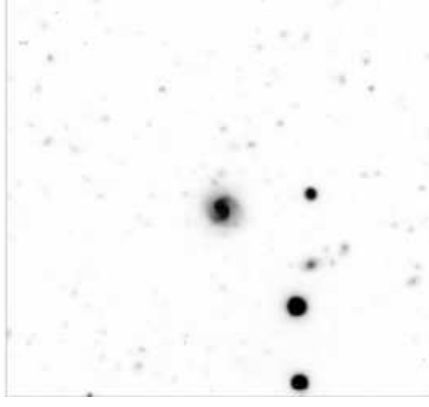
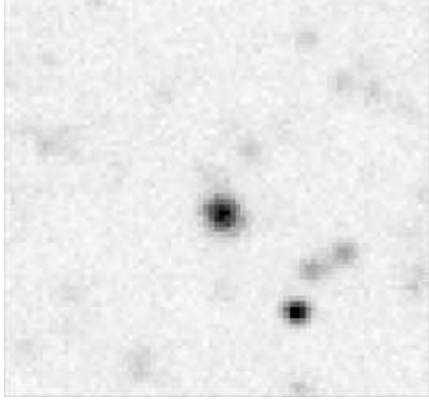
BLAST ID 335, z = 0.425610



BLAST ID 360, z = 0.452000



BLAST ID 568, z = 0.070570



B. Data tables

TABLE B1

PRIMARY COUNTERPARTS TO $\geq 5\sigma$ BLAST SOURCES: REDSHIFT, SPECTRAL AND MORPHOLOGICAL INFORMATION

ID	BLAST name	α_{BLAST}	δ_{BLAST}	deep	z	flag	spec- z	provenance	$\text{H}\alpha$	EW_{rf}	[NII]/H α	AGN flag	Q flag	morphology
1	BLAST J032921–280803	52.33792	–28.13348	0	0.03791	1		AAO	11.4 ± 1.0	0.64		AGN?	...	S
2	BLAST J032956–284631	52.48567	–28.77572	0	0.037	1		AAO	4.6 ± 5.2	0.56		IS
3	BLAST J032741–282325	51.92125	–28.38895	0	0.06067	1		AAO	15.8 ± 3.0	0.74		AGN	...	S
4	BLAST J033235–275530	53.14615	–27.92571	1	0.03764	1		AAO	7.1 ± 2.0	0.60		AGN	...	S
5	BLAST J033131–272842	52.880575	–27.479735	1	0.06668	1		AAO	13.4 ± 0.9	1.33		AGN	...	S
6	BLAST J033229–274415	53.12448	–27.740165	1	0.07593	1		AAO	38.4 ± 1.6	0.43		S
7	BLAST J033250–273420	53.20818	–27.57581	1	0.25126	1		AAO	31.3 ± 3.6	0.44		IS?
8	BLAST J033548–274920	53.954945	–27.821905	0	0.16752	1		AAO	13.1 ± 3.3	1.18		AGN
9	BLAST J032916–273919	52.31905	–27.65615	0	0.01474	1		AAO	82.9 ± 1.6	0.26		S
10	BLAST J032850–263654	52.20959	–26.61418	0	0.0431	1		NED ^a
11	BLAST J033424–274527	53.60242	–27.75861	1	0.12451	1		AAO	13.5 ± 3.5	0.45		S
12	BLAST J032907–284121	52.28185	–28.6882	0	0.06694	1		AAO	7.6 ± 3.0	0.58		S
13	BLAST J032950–285058	52.456265	–28.849455	0	0.07611	1		AAO	9.4 ± 4.6	0.57		S
15	BLAST J033341–280742	53.423975	–28.127015	1	0.34925	1		AAO	I?
16	BLAST J033059–280955	52.748	–28.166875	1	0.07762	1		AAO	35.8 ± 1.4	0.38		S
17	BLAST J033249–275838	53.20553	–27.97915	1	1.256	0		EAZY		Q	C	
18	BLAST J033123–275707	52.847915	–27.949675	1		Q	C	
19	BLAST J033417–273927	53.57377	–27.65889	1	0.14583	1		AAO	19.7 ± 2.4	0.53	
20	BLAST J033340–273811	53.422255	–27.63582	1	0.10148	1		AAO	8.1 ± 2.5	1.02		AGN
21	BLAST J033152–281235	52.96558	–28.20779	1	0.18089	1		AAO	6.9 ± 4.2	0.75		AGN	...	S
22	BLAST J033152–273929	52.967105	–27.6574	1	1.96	0		EAZY		AGN (NED)	Q	C
23	BLAST J033258–274324	53.24671	–27.72366	1	0.91	0		EAZY	C
24	BLAST J033129–275720	52.87454	–27.956275	1		Q?	C	
26	BLAST J033246–275743	53.191665	–27.962605	1	0.10378	1		AAO	17.3 ± 3.3	0.37		S
27	BLAST J032956–281843	52.48787	–28.31118	0	0.05952	1		AAO	23.6 ± 2.5	0.41		S
28	BLAST J033317–280901	53.32528	–28.15234	1		Q?	C	
29	BLAST J032822–283205	52.09467	–28.53271	0	0.07023	1		AAO	15.6 ± 2.6	0.43		S?
30	BLAST J033111–275820	52.79799	–27.97185	1
31	BLAST J033414–274217	53.56036	–27.706065	1	0.1027	1		AAO	26.8 ± 2.0	0.43	
32	BLAST J033332–272900	53.38416	–27.48815	1	0.14466	1		AAO	31.6 ± 2.0	0.49	
34	BLAST J033149–274335	52.95715	–27.724	1	0.62046	1		AAO
35	BLAST J033217–275905	53.071035	–27.97958	1	1.991	0		EAZY	C
36	BLAST J033317–274606	53.324045	–27.768385	1	2.303	0		EAZY	C
37	BLAST J032842–264107	52.17858	–26.6829	0
38	BLAST J033216–280350	53.066375	–28.06329	1	0.51928	1		AAO	E?
39	BLAST J033106–274508	52.77753	–27.75455	1
40	BLAST J032821–292636	52.08769	–29.44216	0	0.0897	1		AAO	S
41	BLAST J033430–271915	53.62789	–27.320845	0	0.10332	1		AAO	21.7 ± 2.1	0.49	
42	BLAST J033145–274635	52.939065	–27.777815	1	C
43	BLAST J033308–274809	53.29047	–27.800445	1	0.18081	1		AAO	33.4 ± 4.6	0.32		S
44	BLAST J033131–273235	52.88022	–27.544245	1		Q?	C	
45	BLAST J033150–281126	52.96289	–28.18947	1	0.21316	1		AAO	7.3 ± 4.6	0.56		S
46	BLAST J033110–265744	52.7943	–26.96136	0	S
47	BLAST J033111–275605	52.79519	–27.93269	1	C?/S?
48	BLAST J033054–275457	52.73177	–27.9168	1
49	BLAST J033032–273527	52.63694	–27.595065	1	0.10671	1		AAO	20.4 ± 2.8	0.43		S
50	BLAST J032904–284759	52.268575	–28.797885	0	0.2892	1		AAO		AGN (NED)	...	IS?/S?
51	BLAST J033046–275515	52.69288	–27.921775	1	0.52449	1		AAO		Q	C	
52	BLAST J033214–281133	53.06131	–28.19199	1	0.528	0		RR	C

TABLE B1—Continued

ID	BLAST name	α_{BLAST}	δ_{BLAST}	deep	z	flag spec- z	provenance	$\text{H}\alpha$	EW_{rf}	[NII]/ $\text{H}\alpha$	AGN flag	Q flag	morphology
53	BLAST J033419–265319	53.5817	–26.88803	0	S
54	BLAST J033151–274428	52.96448	–27.74109	1	1.016	0	EAZY	C
55	BLAST J033129–275557	52.87458	–27.93354	1	0.678	1	AAO	BC
56	BLAST J033034–274325	52.6438	–27.72466	1
57	BLAST J033432–275140	53.63655	–27.86255	1	IS?
58	BLAST J033110–280011	52.79956	–27.99783	1
60	BLAST J033421–275033	53.59264	–27.8454	1
61	BLAST J033148–280424	52.952355	–28.076205	1
62	BLAST J033119–275822	52.83376	–27.97194	1	0.898	0	COMBO17	BC
63	BLAST J033316–275045	53.318815	–27.844285	1	0.0874	1	AAO	14.9 ± 3.1	0.51	S
64	BLAST J033240–280310	53.16542	–28.05305	1
65	BLAST J033018–275500	52.57593	–27.91682	1	0.07946	1	AAO	9.9 ± 2.3	0.42	S
66	BLAST J033205–274648	53.020375	–27.779815	1	2.019	0	EAZY	Q?	C
68	BLAST J033146–275732	52.944085	–27.9597	1	0.3645	1	AAO	S
69	BLAST J033153–281036	52.97797	–28.1766	1	0.21472	1	AAO	34.6 ± 3.9	0.40	S
70	BLAST J033111–284835	52.79579	–28.80925	0	0.10895	1	AAO	1.5 ± 2.5	1.60	AGN	S
71	BLAST J033140–272937	52.91928	–27.493975	1	0.06728	1	AAO	5.5 ± 1.9	0.60	AGN (broad $\text{H}\alpha$)	S
72	BLAST J033120–273344	52.834745	–27.56287	1	0.19504	1	AAO	15.1 ± 4.8	0.50	S
73	BLAST J033158–273519	52.99226	–27.58947	1	2.034	0	EAZY	Q	C
75	BLAST J033115–273905	52.810675	–27.651895	1	0.31183	1	AAO	7.6 ± 4.3	0.44	E
76	BLAST J033228–273949	53.37102	–27.66589	1	0.808	0	EAZY
77	BLAST J033218–273138	53.07989	–27.52747	1	0.22716	1	AAO	16.4 ± 3.8	0.41	S?
78	BLAST J033401–274759	53.50673	–27.79859	1
80	BLAST J033156–284241	52.99144	–28.70857	0	AGN (NED)	Q?	C
83	BLAST J033633–284223	54.14349	–28.70855	0	0.19754	1	AAO	26.1 ± 3.9	0.41	S
84	BLAST J033318–281436	53.329275	–28.242505	1	0.10287	1	AAO	12.6 ± 2.7	0.48	S
85	BLAST J033153–274950	52.97289	–27.83057	1	0.8409	1	AAO	C?
86	BLAST J033447–283013	53.700025	–28.502715	0	0.04139	1	AAO	28.0 ± 2.1	0.47	S
87	BLAST J032746–265801	51.94289	–26.96452	0	0.043304	1	NED ^a	S?
88	BLAST J033636–284115	54.15564	–28.68673	0	0.06828	1	AAO	36.3 ± 2.4	0.43	S
90	BLAST J032818–274311	52.07546	–27.719205	0	0.24845	1	AAO	4.8 ± 9.0	1.38	AGN	S?
92	BLAST J033241–280557	53.1742	–28.09777	1	0.29663	1	AAO	25.5 ± 16.1	0.45	S
93	BLAST J033408–273514	53.5334	–27.59049	1
94	BLAST J033351–274357	53.46998	–27.72938	1	0.22496	1	AAO	14.7 ± 3.2
95	BLAST J033343–270918	53.4297	–27.15331	0	0.0685	1	AAO	4.0 ± 2.5	0.65	AGN?	S
96	BLAST J033336–272854	53.40486	–27.48539	1	0.14489	1	AAO	14.9 ± 9.4	0.49	S
97	BLAST J033117–280220	53.317655	–28.03985	1	0.34897	1	AAO	S?
98	BLAST J033214–273053	53.0595	–27.51728	1
99	BLAST J033247–270716	53.19616	–27.11917	0
100	BLAST J033203–281015	53.01636	–28.17114	1	1.432	0	RR	Q	C
101	BLAST J033127–281009	52.86677	–28.16924	1	Q?	C
102	BLAST J033124–275207	52.85381	–27.868845	1	1.182	0	RR	AGN (NED)	Q	C
103	BLAST J032707–270516	51.78465	–27.09038	0
106	BLAST J032704–280713	51.76851	–28.12049	0	0.089978	1	NED ^a	S
109	BLAST J033408–275415	53.53403	–27.90217	1	S
110	BLAST J033217–275054	53.074425	–27.849725	1	0.12275	1	AAO	7.9 ± 6.5	0.55	S
112	BLAST J033241–273818	53.17499	–27.63874	1	0.832	0	COMBO17
113	BLAST J033347–273848	53.4544	–27.64381	1	AGN (NED)
115	BLAST J033128–280508	52.86134	–28.08199	1	S
118	BLAST J033238–273151	53.158495	–27.53339	1

TABLE B1—Continued

ID	BLAST name	α_{BLAST}	δ_{BLAST}	deep	z	flag	spec- z	provenance	$\text{H}\alpha$	EW_{rf}	[NII]/H α	AGN flag	Q flag	morphology
119	BLAST J033606–272311	54.0313	−27.38652	0	Q	...
120	BLAST J032703–282950	51.76878	−28.49448	0
122	BLAST J033025–275014	52.60716	−27.83824	1	0.12152	1	AAO	35.4 ± 2.7	0.35	S
123	BLAST J033112–265716	52.8017	−26.95459	0
125	BLAST J033229–273505	53.12247	−27.58556	1	0.52	0	EAZY	C
126	BLAST J033211–283251	53.05272	−28.54705	0	0.69385	1	AAO	S?
127	BLAST J033224–291707	53.10425	−29.28513	0	0.132	0	RR	IS
128	BLAST J033100–275310	52.75566	−27.8887	1	0.959	0	RR	RC
129	BLAST J033225–284148	53.11398	−28.6995	0	0.17159	1	AAO	30.7 ± 3.7	0.47	S
130	BLAST J033505–274027	53.76858	−27.6737	0	0.472	0	RR	C
131	BLAST J033200–273604	53.00352	−27.59926	1	0.767	0	EAZY	AGN (NED)	Q?	...	C
132	BLAST J033225–273818	53.104395	−27.63964	1	0.772	0	EAZY	RC
134	BLAST J032813–270453	52.05436	−27.08062	0	0.037356	1	NED ^b	S
135	BLAST J033134–282344	52.89175	−28.40077	0	0.27897	1	AAO	68.1 ± 4.6	0.38	S
136	BLAST J033228–273547	53.118995	−27.59364	1	0.41	0	EAZY	AGN (NED)	Q?	...	E?
137	BLAST J032822–280809	52.08978	−28.136615	0	0.21831	1	AAO	50.4 ± 3.7	0.44	S
138	BLAST J033348–275015	53.45399	−27.83728	1
139	BLAST J033626–270939	54.10876	−27.15997	0	0.24401	1	AAO	47.6 ± 5.2	0.66	...	AGN?
140	BLAST J032644–285106	51.69027	−28.84995	0
143	BLAST J033148–280958	52.950265	−28.169025	1	0.3809	1	AAO	E?
145	BLAST J033211–275859	53.04655	−27.98295	1	0.165	0	EAZY	S
146	BLAST J033000–275347	52.50169	−27.89651	1	0.143	0	RR	S
147	BLAST J033110–274302	52.79279	−27.71546	1
148	BLAST J033104–275001	52.76799	−27.83581	1
149	BLAST J033612–281046	54.05851	−28.18294	0	0.1967	1	AAO	14.1 ± 8.1	0.81	AGN	S?	...
152	BLAST J033648–271936	54.20443	−27.3274	0	0.1458	1	AAO	4.2 ± 10.8	1.09	AGN	S?	...
153	BLAST J033116–263428	52.81561	−26.57759	0
154	BLAST J033541–285524	53.9221	−28.92295	0	0.12255	1	AAO	20.5 ± 5.3	0.46	S
155	BLAST J032929–284222	52.37317	−28.705265	0	0.07029	1	AAO	23.8 ± 2.5	0.38	S
157	BLAST J033609–280942	54.03839	−28.16214	0	0.31589	1	AAO	21.0 ± 6.5	0.62	...	AGN?	...	S	...
158	BLAST J033307–281412	53.280815	−28.2363	1	0.038	0	RR	S
160	BLAST J032843–274414	52.18251	−27.73569	0	S?
162	BLAST J033154–274406	52.979145	−27.73628	1	0.7584	1	AAO	BC?
163	BLAST J033114–273412	52.80916	−27.570105	1	0.53355	1	AAO	IS?
165	BLAST J033605–293357	54.02465	−29.5702	0	0.45211	0	RR	S
166	BLAST J033053–293431	52.72938	−29.57429	0	0.200653	1	AAO	E?
167	BLAST J033247–274221	53.199495	−27.709135	1	0.98054	1	AAO	AGN (NED)	Q	...	C
168	BLAST J033110–275303	52.79792	−27.88302	1	0.2652	1	AAO	S
169	BLAST J033235–280626	53.14828	−28.10735	1	1.547	0	RR	C
170	BLAST J033039–275805	52.66032	−27.96378	1	0.337	0	RR
173	BLAST J033132–281257	52.88347	−28.21739	1
174	BLAST J033229–273948	53.12323	−27.66337	1
175	BLAST J033619–272415	54.08544	−27.40627	0
178	BLAST J033600–265102	54.00227	−26.8485	0
179	BLAST J033259–273536	53.24711	−27.59284	1	0.892	0	EAZY
180	BLAST J033304–271943	53.27217	−27.33042	0
183	BLAST J033245–281104	53.18489	−28.18372	1	0.30017	0	RR	S
184	BLAST J033350–273520	53.459	−27.58877	1
185	BLAST J033424–274514	53.60793	−27.75361	1
188	BLAST J033111–275546	52.795145	−27.93146	1	0.28145	1	AAO	40.7 ± 4.8	0.39	S

TABLE B1—Continued

ID	BLAST name	α_{BLAST}	δ_{BLAST}	deep	z	flag spec- z	provenance	$H\alpha$	EW_{rf}	[NII]/H α	AGN flag	Q flag	morphology
196	BLAST J033211-280514	53.05099	-28.087925	1
197	BLAST J033335-273244	53.39648	-27.54589	1
198	BLAST J033215-273930	53.06753	-27.65851	1	1.32358	1	AAO	Quasar	Q	C
200	BLAST J033440-275630	53.67054	-27.94207	1	0.127	0	RR	S?
202	BLAST J032742-281911	51.9274	-28.3152	0
203	BLAST J033529-281053	53.875965	-28.18574	0	AGN (NED)	Q?	C
204	BLAST J033336-274359	53.401885	-27.731985	1	1.461	0	EAZY	AGN (NED)	Q	C
205	BLAST J032713-285101	51.80349	-28.85086	0
207	BLAST J033553-275555	53.47468	-27.930105	1	1.93998	1	AAO	Quasar	Q	C
208	BLAST J033015-273940	52.56557	-27.66277	1
210	BLAST J033335-274827	53.39681	-27.805595	1	1.165	0	COMBO17
212	BLAST J033127-281027	52.86584	-28.17471	1	0.986	0	RR	S?
213	BLAST J033402-273916	53.51502	-27.656585	1
218	BLAST J033141-275530	52.924145	-27.927055	1	1.111	0	EAZY
219	BLAST J033150-270007	52.95915	-27.00111	0
220	BLAST J033440-274905	53.6662	-27.81678	1
221	BLAST J033211-273729	53.048555	-27.62394	1	1.56472	1	AAO	Quasar	Q	C
222	BLAST J032753-284023	51.9713	-28.67426	0	1.128	0	RR	RC?
223	BLAST J033423-274409	53.59818	-27.74068	1
225	BLAST J033123-275233	52.84398	-27.88026	1
226	BLAST J033723-274021	54.34546	-27.67242	0	1.80174	1	AAO	Quasar	Q	C
231	BLAST J033409-275213	53.541355	-27.870135	1
232	BLAST J033213-272619	53.05288	-27.43903	1
235	BLAST J033302-275635	53.26098	-27.94549	1
236	BLAST J033336-275328	53.39511	-27.88722	1
238	BLAST J032813-285930	52.06044	-28.98913	0	0.439	0	RR
239	BLAST J033120-274933	52.83408	-27.82483	1	0.842	0	COMBO17	BC?
240	BLAST J033306-274415	53.27565	-27.73757	1	0.879	0	EAZY
245	BLAST J032752-290904	51.96693	-29.1531	0	0.337	0	RR	E
246	BLAST J033053-275704	52.72465	-27.95224	1
248	BLAST J033346-271431	53.44989	-27.24417	0	S?
250	BLAST J033138-274122	52.91475	-27.68874	1	2.212	0	EAZY	Q	...	C
252	BLAST J033545-290948	53.9439	-29.16091	0	0.28233	0	RR
253	BLAST J032726-291936	51.86079	-29.32844	0	Q	...	C
254	BLAST J033141-273107	52.91843	-27.51704	1
255	BLAST J033122-275130	52.840975	-27.856485	1	1.337	0	COMBO17	Q	...	C
257	BLAST J032550-284919	51.46241	-28.82178	0
259	BLAST J033105-280634	52.77208	-28.10434	1	0.16701	1	AAO	37.5 ± 3.8	0.54	S
261	BLAST J033306-272831	53.27457	-27.47684	1	Q?	...	C
262	BLAST J033242-275511	53.179985	-27.920665	1	Q	...	C
264	BLAST J033306-271435	53.27784	-27.24149	0
265	BLAST J033127-274430	52.86584	-27.74164	1	0.216	1	NED ^c	C?
266	BLAST J033342-275117	53.43335	-27.85256	1
270	BLAST J033251-273417	53.21302	-27.56991	1
274	BLAST J033053-275513	52.71999	-27.91641	1	0.89505	1	AAO	E
275	BLAST J033149-280936	52.95832	-28.16156	1	1.455	0	RR	Q	...	C
277	BLAST J033254-273308	53.2304	-27.55273	1
280	BLAST J033351-273306	53.46829	-27.55235	1
288	BLAST J033507-275242	53.78062	-27.88157	0
289	BLAST J033102-273948	52.75508	-27.66077	1	0.24165	0	RR	BC?

TABLE B1—Continued

ID	BLAST name	α_{BLAST}	δ_{BLAST}	deep	z	flag	spec- z	provenance	$\text{H}\alpha$	EW_{rf}	$[\text{NII}]/\text{H}\alpha$	AGN flag	Q flag	morphology
294	BLAST J033324–273432	53.354965	−27.57337	1	0.504	0		COMBO17
302	BLAST J033552–275511	53.97283	−27.91971	0	1.884	0		RR
303	BLAST J033121–275803	52.84267	−27.965485	1	0.52975	1		AAO	E
304	BLAST J033231–280437	53.1321	−28.07667	1
307	BLAST J033210–270531	53.04573	−27.09132	0
309	BLAST J033113–273016	52.80434	−27.50111	1	Q	...
311	BLAST J033017–283020	52.57364	−28.50466	0	2.565	0		RR	C?
318	BLAST J033210–280711	53.04041	−28.12135	1	0.9805	1		AAO
319	BLAST J033036–273717	52.64954	−27.62388	1
320	BLAST J032656–291615	51.74249	−29.27044	0	Q	C
322	BLAST J033321–280333	53.34598	−28.05703	1	1.1365	0		EAZY
323	BLAST J033557–283540	53.98524	−28.59187	0	0.4388	0		RR	IS?
329	BLAST J033332–281348	53.39012	−28.23444	1	1.37631	1		AAO	Quasar	Q	C
332	BLAST J033038–274738	52.66361	−27.79376	1	Q	C
333	BLAST J033649–275932	54.20814	−27.99234	0	0.698	0		RR
335	BLAST J033611–290528	54.05066	−29.08868	0	0.42561	0		RR	S
339	BLAST J033018–285124	52.57649	−28.85588	0	0.47231	0		RR	S
341	BLAST J033445–275038	53.69046	−27.84443	1
342	BLAST J032745–292408	51.9383	−29.39774	0
343	BLAST J033430–273704	53.62629	−27.61929	1
344	BLAST J033239–280553	53.16118	−28.09707	1
346	BLAST J032702–281055	51.7626	−28.18012	0
355	BLAST J033117–272006	52.8241	−27.33796	0	0.1064	1		AAO	15.1 ± 5.0	0.37
359	BLAST J033545–272937	53.94254	−27.49272	0
360	BLAST J032735–285902	51.89937	−28.98942	0	0.432	0		RR	Q	C
368	BLAST J032957–290321	52.48499	−29.05382	0	0.07037	1		AAO	S
369	BLAST J033359–293715	53.49599	−29.62169	0	S
376	BLAST J033031–264922	52.63121	−26.82185	0

NOTE.—Reading from the left, the columns are: the BLAST identification number; the full IAU name of the BLAST source; the position of the counterpart (the arithmetic mean between the two sets of coordinates if both the radio and 24 μm counterparts are present); flag indicating whether the source is located within BGS-Deep; the redshift; flag indicating whether the redshift is spectroscopic or photometric; the provenance of the redshift (see Section 2.6 for details); the $\text{H}\alpha$ rest-frame Equivalent Width (EW_{rf}) from AAOmega spectra, in Å, with uncertainty; the ratio of the flux in the [NII] 658.3 line to the flux in the $\text{H}\alpha$ line, from AAOmega spectra; column assessing the presence of an AGN in the host galaxy, based on line ratios ($[\text{NII}]/\text{H}\alpha > 0.6$, Kauffmann et al. 2003; Miller et al. 2003), or of a quasar, based solely on the broadness of the lines (we also indicate with “NED” objects flagged as AGN in NED); column assessing whether the objects is a quasar (Q), based solely on optical and mid-IR (IRAC) colors (see Section 6 for details); morphological classification: S=spiral, IS=interacting system, E=elliptical, C=compact, RC=red compact, BC=blue compact (see Section 7 for details).

^aColless et al. (2003)

^bRatcliffe et al. (1998)

^cRavikumar et al. (2007)

TABLE B2

PRIMARY COUNTERPARTS TO $\geq 5\sigma$ BLAST SOURCES: UV AND FIR PROPERTIES

ID	GALEX name	α_{GALEX}	δ_{GALEX}	FUV	NUV	$E(B - V)$	SFR_{FUV}	SFR_{NUV}	L_{FIR}	M_{\star}
1	GALEX J032920.6-280800	52.336213	-28.133591	17.23 \pm 0.12	16.795 \pm 0.067	0.0071	2.01 \pm 0.22	3.25 \pm 0.2	4.94 $^{+0.17}_{-0.16}$...
2	GALEX J032956.4-284633	52.485265	-28.775954	17.78 \pm 0.12	17.051 \pm 0.067	0.01456	1.22 \pm 0.14	2.59 \pm 0.16	2.85 $^{+0.06}_{-0.10}$...
3	GALEX J032740.9-282320	51.920727	-28.389056	19.09 \pm 0.12	18.637 \pm 0.067	0.00862	0.94 \pm 0.1	1.55 \pm 0.1	10.5 $^{+0.2}_{-0.4}$...
4	GALEX J033235.0-275532	53.14599	-27.925756	20.49 \pm 0.12	20.176 \pm 0.068	0.00864	0.1 \pm 0.01	0.14 \pm 0.01	0.55 $^{+0.10}_{-0.04}$...
5	GALEX J033131.3-272846	52.880468	-27.479551	19.23 \pm 0.12	18.716 \pm 0.067	0.00995	1.01 \pm 0.11	1.76 \pm 0.11	2.64 $^{+0.44}_{-0.11}$...
6	GALEX J033229.8-274423	53.124378	-27.73994	19.97 \pm 0.12	19.435 \pm 0.067	0.0092	0.66 \pm 0.07	1.17 \pm 0.07	3.21 $^{+0.31}_{-0.37}$...
7	GALEX J033249.8-273433	53.207886	-27.575957	22.08 \pm 0.13	21.065 \pm 0.068	0.00827	1.16 \pm 0.14	2.89 \pm 0.18	27.4 $^{+4.9}_{-3.3}$	12.791 \pm 2.442
8	GALEX J033549.0-274919	53.95423	-27.822048	21.95 \pm 0.13	20.976 \pm 0.073	0.01343	0.56 \pm 0.07	1.43 \pm 0.1	63.2 $^{+1.2}_{-4.4}$...
9	GALEX J032916.5-273921	52.318753	-27.655832	17.01 \pm 0.12	16.65 \pm 0.067	0.01112	0.38 \pm 0.04	0.58 \pm 0.04	0.30 $^{+0.02}_{-0.01}$...
10	3.02 $^{+0.27}_{-0.28}$...
11	GALEX J033424.5-274530	53.602409	-27.758395	19.44 \pm 0.12	19.018 \pm 0.067	0.00853	2.94 \pm 0.33	4.61 \pm 0.29	5.71 $^{+1.29}_{-0.40}$...
12	GALEX J032907.6-284117	52.281953	-28.688087	20.41 \pm 0.12	19.625 \pm 0.067	0.01167	0.35 \pm 0.04	0.78 \pm 0.05	6.62 $^{+0.40}_{-0.32}$	4.253 \pm 0.837
13	GALEX J032949.4-285057	52.455946	-28.849296	20.45 \pm 0.12	19.843 \pm 0.068	0.0121	0.44 \pm 0.05	0.83 \pm 0.05	8.11 $^{+0.22}_{-0.81}$	1.228 \pm 0.315
15	GALEX J033341.7-280736	53.423854	-28.126769	21.42 \pm 0.12	20.352 \pm 0.068	0.00853	4.47 \pm 0.5	10.97 \pm 0.69	36.2 $^{+8.3}_{-8.2}$	19.742 \pm 3.56
16	GALEX J033059.4-281000	52.74774	-28.166835	18.64 \pm 0.12	18.225 \pm 0.067	0.00926	2.34 \pm 0.26	3.73 \pm 0.23	4.72 $^{+0.31}_{-0.46}$	1.718 \pm 0.35
17	GALEX J033249.5-275839	53.206398	-27.977736	...	23.738 \pm 0.125	0.00806	...	9.67 \pm 1.11	404 $^{+190}_{-127}$	8.151 \pm 1.516
18
19	GALEX J033417.6-273931	53.57366	-27.658699	21.42 \pm 0.12	20.682 \pm 0.068	0.00846	0.66 \pm 0.07	1.37 \pm 0.09	10.2 $^{+1.8}_{-0.9}$...
20	GALEX J033341.2-273808	53.421869	-27.635593	22.98 \pm 0.13	22.176 \pm 0.072	0.00802	0.07 \pm 0.01	0.17 \pm 0.01	7.00 $^{+0.47}_{-0.84}$...
21	GALEX J033151.5-281227	52.964884	-28.207763	21.05 \pm 0.12	20.562 \pm 0.068	0.00938	1.47 \pm 0.16	2.37 \pm 0.15	12.4 $^{+1.5}_{-2.5}$	10.541 \pm 2.014
22	498 $^{+582}_{-148}$	3.896 \pm 1.228
23	142 $^{+68}_{-64}$	5.825 \pm 1.132
24
26	GALEX J033245.9-275745	53.191281	-27.962535	19.88 \pm 0.12	19.477 \pm 0.067	0.00806	1.34 \pm 0.15	2.09 \pm 0.13	3.00 $^{+0.25}_{-0.89}$	3.08 \pm 0.536
27	GALEX J032957.0-281840	52.48763	-28.311293	18.52 \pm 0.12	17.865 \pm 0.067	0.00898	1.53 \pm 0.17	3.05 \pm 0.19	2.18 $^{+0.32}_{-0.24}$	1.238 \pm 0.246
28	GALEX J033318.1-280908	53.3254	-28.152402	25.7 \pm 0.33	25.746 \pm 0.246	0.00841
29	6.06 $^{+0.39}_{-0.49}$...
30
31	GALEX J033414.4-274221	53.560362	-27.706052	21.78 \pm 0.12	20.954 \pm 0.068	0.00844	0.23 \pm 0.03	0.53 \pm 0.03	3.33 $^{+0.65}_{-0.58}$...
32	GALEX J033332.1-272917	53.383843	-27.488205	21.15 \pm 0.12	20.51 \pm 0.068	0.0083	0.83 \pm 0.09	1.57 \pm 0.1	5.22 $^{+1.29}_{-0.93}$...
34	GALEX J033149.6-274325	52.956886	-27.723754	...	22.887 \pm 0.083	0.00904	...	3.48 \pm 0.27	46.3 $^{+46.1}_{-10.4}$	15.243 \pm 2.493
35	1229 $^{+599}_{-436}$	4.604 \pm 0.784
36	1344 $^{+365}_{-670}$	12.073 \pm 2.149
37
38	GALEX J033215.7-280348	53.065624	-28.063464	...	23.01 \pm 0.1	0.00764	...	2.11 \pm 0.19	59.2 $^{+8.1}_{-29.8}$	21.382 \pm 3.922
39
40	GALEX J032821.0-292631	52.087587	-29.442053	19.67 \pm 0.12	19.146 \pm 0.067	0.00854	0.78 \pm 0.09	1.37 \pm 0.08	4.34 $^{+0.92}_{-0.31}$...
41	GALEX J033430.6-271914	53.627691	-27.320708	22.18 \pm 0.13	20.743 \pm 0.069	0.01122	0.16 \pm 0.02	0.66 \pm 0.04	14.6 $^{+1.2}_{-1.1}$...
42
43	GALEX J033309.7-274800	53.290632	-27.800154	22.38 \pm 0.12	21.741 \pm 0.07	0.00814	0.43 \pm 0.05	0.79 \pm 0.05	7.78 $^{+0.73}_{-3.28}$...
44	GALEX J033131.2-273236	52.879954	-27.543585	...	23.862 \pm 0.105	0.00871
45	GALEX J033150.9-281120	52.96221	-28.18901	21.02 \pm 0.12	20.68 \pm 0.068	0.00938	2.17 \pm 0.24	2.97 \pm 0.19	8.89 $^{+2.67}_{-1.89}$	11.915 \pm 1.891
46	GALEX J033110.5-265740	52.79395	-26.961304	18.9 \pm 0.12	18.524 \pm 0.067	0.00774
47	GALEX J033110.8-275552	52.795045	-27.931179	22.53 \pm 0.12	21.851 \pm 0.07	0.0086
48	GALEX J033055.6-275501	52.732045	-27.917032	...	21.0 \pm 0.068	0.0090
49	GALEX J033032.8-273539	52.636808	-27.594438	21.19 \pm 0.12	20.536 \pm 0.069	0.00936	0.43 \pm 0.05	0.84 \pm 0.05	4.63 $^{+0.57}_{-0.77}$	4.769 \pm 0.916
50	70.1 $^{+7.3}_{-6.3}$	34.049 \pm 6.752
51	GALEX J033046.2-275518	52.692639	-27.921688	25.13 \pm 0.32	23.015 \pm 0.105	0.0090	0.49 \pm 0.15	2.17 \pm 0.21	212 $^{+12}_{-41}$...
52	86.6 $^{+13.3}_{-29.6}$	6.812 \pm 1.202
53	GALEX J033419.6-265318	53.581519	-26.888353	19.08 \pm 0.12	18.701 \pm 0.067	0.00995

TABLE B2—Continued

ID	GALEX name	α_{GALEX}	δ_{GALEX}	FUV	NUV	$E(B-V)$	SFR_{FUV}	SFR_{NUV}	L_{FIR}	M_{\star}
54	195^{+71}_{-114}	2.177 ± 0.349
55	GALEX J033130.0–275602	52.87525	−27.933952	24.46 ± 0.19	22.243 ± 0.078	0.00828	137.04 ± 24.31	288.87 ± 20.78	106^{+52}_{-27}	20.026 ± 3.013
56	GALEX J033034.4–274328	52.643648	−27.72453	...	24.576 ± 0.194	0.00846
57	GALEX J033432.9–275148	53.637466	−27.863358	23.54 ± 0.14	22.283 ± 0.076	0.00905
58
60	GALEX J033422.1–275042	53.592338	−27.845121	...	22.939 ± 0.094	0.00871
61
62	GALEX J033120.1–275819	52.833759	−27.971939	...	24.442 ± 0.504	0.0080	...	1.14 ± 0.53	176^{+67}_{-56}	...
63	GALEX J033316.4–275039	53.318678	−27.844186	21.93 ± 0.12	21.247 ± 0.069	0.00738	0.14 ± 0.02	0.29 ± 0.02	$1.76^{+0.25}_{-0.55}$	3.845 ± 0.65
64
65	GALEX J033018.2–275500	52.575918	−27.916683	18.88 ± 0.12	18.508 ± 0.067	0.00827	1.96 ± 0.22	2.99 ± 0.18	$2.40^{+0.26}_{-0.56}$	1.911 ± 0.381
66	835^{+256}_{-432}	15.543 ± 2.356
68	GALEX J033146.6–275734	52.944236	−27.959632	24.44 ± 0.19	22.748 ± 0.099	0.00818	0.31 ± 0.05	1.31 ± 0.12	$46.9^{+7.4}_{-12.2}$	11.692 ± 1.66
69	GALEX J033154.6–281035	52.977711	−28.176491	22.74 ± 0.23	21.844 ± 0.12	0.00909	0.45 ± 0.1	1.03 ± 0.11	$5.40^{+4.82}_{-0.83}$	4.392 ± 0.85
70	GALEX J033110.9–284832	52.795552	−28.80897	19.06 ± 0.12	18.7 ± 0.067	0.01024	3.21 ± 0.36	4.79 ± 0.3	$6.51^{+0.33}_{-0.33}$	10.717 ± 2.23
71	GALEX J033140.6–272938	52.919358	−27.494078	21.62 ± 0.12	20.574 ± 0.068	0.00888	0.11 ± 0.01	0.32 ± 0.02	$1.22^{+0.39}_{-0.22}$...
72	GALEX J033120.3–273346	52.834738	−27.562779	21.31 ± 0.12	20.713 ± 0.069	0.00973	1.37 ± 0.16	2.41 ± 0.15	$5.50^{+2.60}_{-1.44}$	8.098 ± 1.493
73	497^{+573}_{-204}	11.63 ± 1.93
75	GALEX J033114.5–273906	52.810475	−27.651857	22.46 ± 0.12	21.119 ± 0.07	0.00914	1.32 ± 0.15	4.31 ± 0.28	$10.1^{+7.2}_{-3.0}$	38.27 ± 7.201
76	$66.5^{+59.3}_{-24.3}$	8.598 ± 1.161
77	GALEX J033219.1–273138	53.079817	−27.527321	21.62 ± 0.12	21.032 ± 0.068	0.00952	1.44 ± 0.16	2.45 ± 0.15	$6.11^{+2.90}_{-3.01}$	12.134 ± 2.735
78	GALEX J033401.5–274754	53.506405	−27.798424	...	23.327 ± 0.504	0.00754
80
83	GALEX J033634.3–284230	54.143208	−28.708474	21.53 ± 0.12	20.353 ± 0.07	0.01355	1.18 ± 0.13	3.55 ± 0.23	$28.2^{+0.6}_{-5.7}$	10.255 ± 2.071
84	GALEX J033318.9–281434	53.329027	−28.242794	21.3 ± 0.12	20.741 ± 0.069	0.00852	0.36 ± 0.04	0.64 ± 0.04	$3.82^{+0.23}_{-1.06}$	6.028 ± 1.128
85	GALEX J033153.4–274950	52.972841	−27.830587	...	23.772 ± 0.102	0.00798	...	2.17 ± 0.2	105^{+31}_{-58}	...
86	GALEX J033447.9–283009	53.699655	−28.502527	19.8 ± 0.12	19.295 ± 0.068	0.00847	0.23 ± 0.03	0.39 ± 0.02	$0.98^{+0.20}_{-0.08}$	0.815 ± 0.129
87	GALEX J032746.7–265745	51.944804	−26.962548	19.37 ± 0.12	19.027 ± 0.067	0.01328	$1.16^{+0.33}_{-0.25}$...
88	GALEX J033637.3–284112	54.155408	−28.686825	19.89 ± 0.12	19.342 ± 0.068	0.01355	0.59 ± 0.07	1.06 ± 0.07	$3.79^{+0.19}_{-0.19}$...
90	GALEX J032818.0–274307	52.07511	−27.718748	22.99 ± 0.16	21.647 ± 0.073	0.01206	0.51 ± 0.07	1.7 ± 0.12	$60.0^{+5.4}_{-6.9}$...
92	GALEX J033241.8–280550	53.17437	−28.097491	23.45 ± 0.14	22.624 ± 0.079	0.00717	0.47 ± 0.06	0.96 ± 0.07	$6.51^{+8.38}_{-1.36}$	3.142 ± 0.674
93
94	GALEX J033352.8–274347	53.470297	−27.729779	22.21 ± 0.12	21.255 ± 0.069	0.0071	0.8 ± 0.09	1.92 ± 0.12	$4.89^{+4.45}_{-1.38}$...
95	GALEX J033343.0–270910	53.429287	−27.153012	20.0 ± 0.12	19.456 ± 0.067	0.01134	0.53 ± 0.06	0.95 ± 0.06	$3.33^{+0.47}_{-0.23}$...
96	GALEX J033337.1–272906	53.404714	−27.485016	21.35 ± 0.12	20.749 ± 0.068	0.00896	0.69 ± 0.08	1.27 ± 0.08	$4.40^{+1.42}_{-1.04}$...
97	GALEX J033316.2–280223	53.317712	−28.039773	23.1 ± 0.13	22.024 ± 0.072	0.00675	0.93 ± 0.11	2.32 ± 0.15	$6.97^{+5.74}_{-2.85}$...
98	GALEX J033214.3–273102	53.059692	−27.517126	22.98 ± 0.15	22.574 ± 0.091	0.00924
99	GALEX J033247.0–270708	53.195852	−27.11912	19.86 ± 0.12	19.29 ± 0.067	0.00891
100	GALEX J033203.8–281015	53.016063	−28.17096	...	23.483 ± 0.094	0.00843	...	25.3 ± 2.19	337^{+262}_{-94}	31.822 ± 14.775
101
102	GALEX J033125.1–275211	52.85488	−27.869679	23.83 ± 0.13	22.265 ± 0.073	0.00772	48.93 ± 6.04	32.23 ± 2.16	378^{+50}_{-197}	19.499 ± 2.896
103	GALEX J032708.3–270524	51.784617	−27.090199	20.55 ± 0.12	19.824 ± 0.068	0.01335
106	GALEX J032704.4–280713	51.768423	−28.120328	23.8 ± 0.19	22.645 ± 0.099	0.00944	$2.15^{+0.45}_{-0.70}$...
109	GALEX J033408.0–275407	53.533691	−27.902007	21.4 ± 0.12	20.924 ± 0.068	0.00744
110	GALEX J033217.7–275058	53.07384	−27.84969	23.95 ± 0.17	23.043 ± 0.097	0.00776	0.04 ± 0.01	0.11 ± 0.01	$1.78^{+0.94}_{-0.66}$	2.402 ± 0.384
112	106^{+79}_{-53}	0.402 ± 0.183
113	GALEX J033349.0–273843	53.454251	−27.645331	...	22.678 ± 0.088	0.00802
115
118
119

TABLE B2—Continued

ID	GALEX name	α_{GALEX}	δ_{GALEX}	FUV	NUV	$E(B - V)$	SFR_{FUV}	SFR_{NUV}	L_{FIR}	M_{\star}
120
122	GALEX J033025.7–275017	52.607255	−27.838082	20.98 ± 0.12	20.351 ± 0.067	0.00826	0.68 ± 0.08	1.28 ± 0.08	3.60 ^{+0.97} _{−0.95}	3.238 ± 0.628
123
125	30.3 ^{+14.5} _{−12.7}	1.672 ± 0.598
126	GALEX J033212.5–283248	53.052314	−28.546836	23.26 ± 0.18	22.781 ± 0.1	0.0082	10.69 ± 1.82	4.83 ± 0.45	53.0 ^{+29.6} _{−25.0}	10.32 ± 3.849
127	GALEX J033225.7–291709	53.107192	−29.285858	19.14 ± 0.12	18.734 ± 0.067	0.00979	4.43 ± 0.49	6.8 ± 0.42	7.06 ^{+1.07} _{−1.46}	8.745 ± 1.719
128	58.5 ^{+120.5} _{−56.2}	48.841 ± 9.912
129	GALEX J033227.3–284157	53.113772	−28.699345	22.89 ± 0.14	21.648 ± 0.072	0.00999	0.24 ± 0.03	0.79 ± 0.05	8.86 ^{+1.87} _{−1.67}	4.049 ± 0.806
130	20.6 ^{+20.3} _{−3.0}	5.854 ± 1.023
131	28.0 ^{+1.3} _{−1.5}	9.677 ± 1.357
132	84.0 ^{+52.5} _{−33.1}	3.939 ± 0.763
134	GALEX J032813.0–270449	52.054388	−27.080549	18.37 ± 0.12	18.001 ± 0.067	0.01253	0.86 ^{+0.10} _{−0.11}	...
135	GALEX J033133.9–282403	52.891282	−28.400861	23.29 ± 0.14	22.015 ± 0.07	0.0087	0.48 ± 0.06	1.5 ± 0.1	24.3 ^{+5.6} _{−6.3}	6.369 ± 1.671
136	GALEX J033228.5–273536	53.11883	−27.593592	25.92 ± 0.3	23.828 ± 0.121	0.0097	0.89 ± 0.24	1.82 ± 0.2	15.4 ^{+11.2} _{−2.9}	37.782 ± 12.281
137	GALEX J032821.5–280811	52.089837	−28.136439	20.49 ± 0.12	19.866 ± 0.068	0.00842	3.69 ± 0.41	6.55 ± 0.41	22.4 ^{+2.9} _{−4.5}	...
138	GALEX J033348.9–275014	53.453949	−27.837456	...	25.064 ± 0.252	0.00622
139	59.3 ^{+7.7} _{−4.2}	...
140
143	GALEX J033147.9–281007	52.949911	−28.168868	24.71 ± 0.24	21.189 ± 0.07	0.00939	0.2 ± 0.04	4.75 ± 0.31	41.1 ^{+12.0} _{−13.5}	16.095 ± 3.185
145	GALEX J033211.1–275858	53.046532	−27.982875	20.08 ± 0.12	19.678 ± 0.067	0.00852	7.45 ± 0.83	10.53 ± 0.65	2.80 ^{+1.92} _{−0.76}	11.444 ± 1.915
146	GALEX J033000.4–275346	52.501809	−27.896302	21.02 ± 0.12	20.379 ± 0.068	0.00844	0.91 ± 0.1	1.74 ± 0.11	4.90 ^{+1.64} _{−0.79}	13.495 ± 2.621
147
148
149	10.3 ^{+3.8} _{−1.1}	6.664 ± 1.246
152	GALEX J033649.0–271938	54.204385	−27.327469	22.28 ± 0.13	21.756 ± 0.078	0.01227	0.31 ± 0.04	0.52 ± 0.04	11.8 ^{+0.8} _{−2.9}	...
153
154	GALEX J033541.2–285521	53.921886	−28.922714	20.12 ± 0.12	19.681 ± 0.068	0.00957	1.53 ± 0.17	2.44 ± 0.15	4.65 ^{+0.33} _{−1.50}	2.386 ± 0.537
155	GALEX J032929.4–284218	52.372851	−28.705028	18.09 ± 0.12	17.747 ± 0.067	0.01159	3.26 ± 0.36	4.83 ± 0.3	3.30 ^{+0.47} _{−0.45}	1.821 ± 0.392
157	GALEX J033609.1–280944	54.037984	−28.162246	23.24 ± 0.19	21.793 ± 0.094	0.01055	0.67 ± 0.12	2.4 ± 0.21	51.6 ^{+6.4} _{−10.8}	18.643 ± 3.62
158	GALEX J033307.3–281409	53.280691	−28.235987	19.82 ± 0.12	19.343 ± 0.067	0.00824	0.19 ± 0.02	0.32 ± 0.02	0.30 ^{+0.09} _{−0.07}	0.389 ± 0.081
160	GALEX J032843.6–274409	52.182047	−27.735859	22.57 ± 0.13	21.426 ± 0.07	0.00847
162	37.7 ^{+68.2} _{−39.8}	3.452 ± 0.616
163	GALEX J033114.1–273411	52.809126	−27.569857	23.38 ± 0.13	21.643 ± 0.073	0.00979	2.63 ± 0.33	7.99 ± 0.54	29.7 ^{+20.2} _{−11.2}	8.753 ± 1.525
165	GALEX J033605.9–293413	54.024817	−29.570388	22.86 ± 0.16	21.547 ± 0.102	0.01119	0.78 ± 0.12	2.51 ± 0.23	20.2 ^{+20.4} _{−3.8}	14.919 ± 2.152
166	GALEX J033055.0–293426	52.729487	−29.574	23.39 ± 0.15	22.279 ± 0.075	0.01019	0.39 ± 0.06	1.07 ± 0.07	20.5 ^{+5.3} _{−1.9}	11.484 ± 2.099
167	GALEX J033247.9–274232	53.199576	−27.709084	...	23.291 ± 0.093	0.00866	...	6.65 ± 0.57	76.6 ^{+86.0} _{−60.1}	...
168	GALEX J033111.4–275257	52.797751	−27.882512	21.24 ± 0.12	20.616 ± 0.068	0.00836	220.07 ± 24.58	60.6 ± 3.79	18.5 ^{+3.6} _{−9.1}	5.826 ± 1.729
169	190 ⁺²⁴³ _{−89}	58.348 ± 8.475
170	GALEX J033038.4–275748	52.660132	−27.963382	25.29 ± 0.24	23.346 ± 0.09	0.00808	0.12 ± 0.03	0.64 ± 0.05	14.0 ^{+3.5} _{−9.3}	4.535 ± 0.814
173	GALEX J033131.7–281304	52.882415	−28.21781	...	23.887 ± 0.145	0.00964
174
175	GALEX J033620.4–272422	54.085237	−27.406153	22.2 ± 0.14	21.557 ± 0.075	0.01406
178
179	74.0 ^{+37.9} _{−53.2}	18.559 ± 2.851
180	GALEX J033305.2–271948	53.271911	−27.330179	23.24 ± 0.13	21.85 ± 0.07	0.00741
183	GALEX J033244.3–281100	53.184679	−28.183461	21.47 ± 0.12	20.878 ± 0.068	0.00699	2.7 ± 0.3	4.5 ± 0.28	9.29 ^{+3.40} _{−6.47}	9.438 ± 1.682
184
185	GALEX J033425.7–274515	53.60709	−27.754291	24.57 ± 0.36	23.602 ± 0.164	0.00853
188	GALEX J033110.8–275552	52.795045	−27.931179	22.53 ± 0.12	21.851 ± 0.07	0.0086	0.99 ± 0.11	1.77 ± 0.11	13.5 ^{+7.1} _{−2.8}	3.276 ± 0.627
196

TABLE B2—Continued

ID	GALEX name	α_{GALEX}	δ_{GALEX}	FUV	NUV	$E(B-V)$	SFR_{FUV}	SFR_{NUV}	L_{FIR}	M_{\star}
197	GALEX J033335.1–273244	53.39624	−27.5457	24.86 ± 0.23	22.901 ± 0.12	0.00817
198	GALEX J033216.3–273930	53.067966	−27.658439	23.93 ± 0.12	21.822 ± 0.067	0.00956	62.19 ± 6.92	79.73 ± 4.93	$83.3^{+267.0}_{-54.9}$...
200	GALEX J033440.8–275630	53.670371	−27.941711	21.85 ± 0.12	21.294 ± 0.068	0.0084	0.33 ± 0.04	0.59 ± 0.04	$5.12^{+1.11}_{-1.66}$...
202
203
204	195^{+253}_{-83}	19.701 ± 2.747
205
207	GALEX J033353.7–275544	53.473739	−27.929006	22.4 ± 0.12	22.126 ± 0.071	0.00648	1120.62 ± 127.35	424.35 ± 27.59	749^{+398}_{-341}	...
208	GALEX J033015.8–273949	52.566056	−27.663656	25.13 ± 0.51	24.129 ± 0.146	0.0081
210	GALEX J033352.2–274815	53.396965	−27.8043	24.46 ± 0.16	22.928 ± 0.126	0.00673	25.97 ± 3.86	16.4 ± 1.9	$85.0^{+97.7}_{-58.6}$	10.078 ± 1.671
212	GALEX J033127.9–281028	52.866437	−28.174512	...	23.496 ± 0.093	0.00923	...	5.62 ± 0.48	248^{+97}_{-81}	32.754 ± 6.222
213	GALEX J033403.8–273926	53.515887	−27.657481	...	23.696 ± 0.114	0.00826
218	168^{+83}_{-123}	4.173 ± 0.755
219
220
221	GALEX J033211.6–273726	53.04849	−27.623971	...	21.167 ± 0.068	0.00958	...	341.74 ± 21.35	222^{+228}_{-140}	...
222	549^{+122}_{-186}	...
223
225	GALEX J033122.5–275248	52.843749	−27.880162	23.78 ± 0.16	20.06 ± 0.067	0.00813
226	GALEX J033722.8–274020	54.345093	−27.672332	...	21.275 ± 0.071	0.01087	...	661.27 ± 43.19	536^{+315}_{-176}	...
231
232	GALEX J033212.3–272616	53.051583	−27.437917	...	23.925 ± 0.106	0.00866
235
236
238	GALEX J032814.4–285920	52.060386	−28.989039	...	23.721 ± 0.231	0.00724	...	0.78 ± 0.16	$54.7^{+4.0}_{-12.7}$...
239	GALEX J033120.0–274931	52.833483	−27.825427	...	23.816 ± 0.136	0.00778	...	2.8 ± 0.35	$74.2^{+30.6}_{-51.0}$	12.658 ± 1.65
240	149^{+29}_{-101}	7.556 ± 1.381
245	GALEX J032752.0–290911	51.96666	−29.153239	23.63 ± 0.17	23.416 ± 0.148	0.00888	0.54 ± 0.08	0.61 ± 0.08	$17.7^{+4.8}_{-8.5}$...
246
248	GALEX J033347.8–271439	53.449416	−27.244119	21.01 ± 0.12	20.521 ± 0.068	0.00896
250	726^{+371}_{-546}	4.35 ± 3.472
252	GALEX J033546.3–290940	53.943079	−29.161188	23.14 ± 0.16	22.404 ± 0.088	0.00962	0.75 ± 0.11	1.38 ± 0.11	$8.00^{+5.49}_{-4.32}$	2.664 ± 0.52
253
254
255	GALEX J033121.8–275123	52.840984	−27.85649	...	23.72 ± 0.164	0.00778	...	5.19 ± 0.79	414^{+272}_{-145}	...
257
259	GALEX J033105.2–280614	52.771873	−28.103937	23.7 ± 0.14	22.53 ± 0.076	0.00833	0.11 ± 0.01	0.33 ± 0.02	$5.01^{+0.72}_{-3.72}$	3.666 ± 0.697
261	GALEX J033305.8–272836	53.274333	−27.476814	...	24.034 ± 0.109	0.0066
262
264
265	GALEX J033127.8–274429	52.865944	−27.741601	23.01 ± 0.13	22.982 ± 0.084	0.00734	$1.40^{+1.78}_{-1.29}$...
266
270
274	$85.6^{+77.9}_{-76.3}$	79.278 ± 15.63
275	603^{+192}_{-250}	42.26 ± 14.891
277
280	GALEX J033352.3–273313	53.468291	−27.553668	...	23.359 ± 0.101	0.00898
288
289	GALEX J033101.4–273934	52.756057	−27.659615	...	23.94 ± 0.138	0.00861	...	0.22 ± 0.03	$2.15^{+2.15}_{-1.57}$	0.034 ± 0.011
294	GALEX J033325.1–273421	53.35491	−27.572659	22.46 ± 0.12	21.921 ± 0.07	0.00693	4.91 ± 0.56	5.37 ± 0.35	$4.78^{+20.84}_{-5.10}$	0.105 ± 0.038

TABLE B2—Continued

ID	GALEX name	α_{GALEX}	δ_{GALEX}	FUV	NUV	$E(B - V)$	SFR_{FUV}	SFR_{NUV}	L_{FIR}	M_{\star}
302	278^{+758}_{-124}	23.653 ± 3.354
303	GALEX J033122.2–275755	52.842805	−27.965377	24.3 ± 0.16	22.897 ± 0.089	0.00851	1.09 ± 0.16	2.45 ± 0.2	$39.3^{+27.1}_{-14.5}$...
304
307
309
311	853^{+115}_{-31}	50.648 ± 8.308
318	GALEX J033209.5–280716	53.039879	−28.121257	...	24.553 ± 0.174	0.0078	...	2.07 ± 0.33	$29.7^{+10.6}_{-32.4}$	6.636 ± 2.516
319
320
322	$17.4^{+149.1}_{-55.8}$	2.625 ± 0.397
323	GALEX J033556.4–283531	53.98499	−28.591981	...	24.087 ± 0.147	0.01151	...	0.22 ± 0.03	$39.3^{+15.8}_{-7.4}$	17.128 ± 2.448
329	GALEX J033333.6–281403	53.390188	−28.234378	25.3 ± 0.31	23.153 ± 0.12	0.00909	19.92 ± 5.7	28.16 ± 3.12	179^{+94}_{-103}	44.785 ± 14.422
332
333	$29.2^{+3.6}_{-3.9}$	10.517 ± 1.675
335	GALEX J033612.1–290520	54.05074	−29.089025	23.03 ± 0.17	22.304 ± 0.09	0.01016	0.69 ± 0.11	1.29 ± 0.11	$44.7^{+16.9}_{-7.9}$	29.11 ± 4.433
339	GALEX J033018.2–285120	52.576305	−28.855675	24.8 ± 0.37	22.842 ± 0.107	0.00979	0.18 ± 0.06	1.0 ± 0.1	$48.5^{+25.9}_{-8.1}$	6.416 ± 1.152
341
342	GALEX J032745.1–292350	51.93792	−29.397395	...	22.528 ± 0.143	0.00822
343
344
346
355	GALEX J033117.7–272016	52.824134	−27.337986	19.84 ± 0.12	19.571 ± 0.068	0.00994	1.49 ± 0.17	2.04 ± 0.13	$1.76^{+0.71}_{-0.54}$...
359
360	GALEX J032735.8–285921	51.899171	−28.989387	23.39 ± 0.16	23.418 ± 0.125	0.00902	1.25 ± 0.18	1.01 ± 0.12	$7.57^{+3.33}_{-3.03}$...
368	GALEX J032956.2–290313	52.484512	−29.053836	21.28 ± 0.12	20.769 ± 0.069	0.00904	0.44 ± 0.05	0.75 ± 0.05	$0.37^{+0.10}_{-0.19}$	0.25 ± 0.048
369
376

NOTE.—Reading from the left, the columns are: the BLAST identification number; the full IAU name of the GALEX counterpart to the BLAST source; the position of the GALEX counterpart; the flux in the FUV filter, in magnitudes, with uncertainty; the flux in the NUV filter, in magnitudes, with uncertainty; Galactic extinction correction as from Schlegel et al. (1998), in magnitudes; star-formation rate as estimated from the FUV flux (see Equation 3), in $\text{M}_{\odot} \text{yr}^{-1}$, with uncertainty (note that we listed SFR_{FUV} for all FUV sources, even if only those with $z < 0.36$ are to be considered reliable, see Section 4.2); star-formation rate as estimated from the NUV flux (see Equation 3), in $\text{M}_{\odot} \text{yr}^{-1}$, with uncertainty (note that we listed SFR_{NUV} for all NUV sources, even if only those with $z < 0.91$ are to be considered reliable, see Section 4.2); rest-frame bolometric FIR luminosity of the BLAST ID, in 10^{10}L_{\odot} , with upper and lower uncertainties (note that we quote the mode, and 68% c.l. of the distribution obtained, see Section 3.2 for details); stellar mass of the BLAST ID, in 10^{10}M_{\odot} (see Section 8 for details), with uncertainty.

REFERENCES

Balogh, M., Eke, V., Miller, C., Lewis, I., Bower, R., Couch, W., Nichol, R., Bland-Hawthorn, J., Baldry, I. K., Baugh, C., Bridges, T., Cannon, R., Cole, S., Colless, M., Collins, C., Cross, N., Dalton, G., de Propris, R., Driver, S. P., Efstathiou, G., Ellis, R. S., Frenk, C. S., Glazebrook, K., Gomez, P., Gray, A., Hawkins, E., Jackson, C., Lahav, O., Lumsden, S., Maddox, S., Madgwick, D., Norberg, P., Peacock, J. A., Percival, W., Peterson, B. A., Sutherland, W., & Taylor, K. 2004, MNRAS, 348, 1355

Barger, A. J., Cowie, L. L., Sanders, D. B., Fulton, E., Taniguchi, Y., Sato, Y., Kawara, K., & Okuda, H. 1998, Nature, 394, 248

Bell, E. F. 2003, ApJ, 586, 794

Béthermin, M., Dole, H., Beelen, A., & Aussel, H. 2010, A&A, 512, A78+

Blain, A. W., Barnard, V. E., & Chapman, S. C. 2003, MNRAS, 338, 733

Blain, A. W., Kneib, J., Ivison, R. J., & Smail, I. 1999, ApJ, 512, L87

Borys, C., Smail, I., Chapman, S. C., Blain, A. W., Alexander, D. M., & Ivison, R. J. 2005, ApJ, 635, 853

Buat, V., Boissier, S., Burgarella, D., Takeuchi, T. T., Le Floc'h, E., Marcillac, D., Huang, J., Nagashima, M., & Enoki, M. 2008, A&A, 483, 107

Buat, V., Giovannoli, E., Burgarella, D., Altieri, B., Amblard, A., Arumugam, V., Aussel, H., Babbedge, T., Blain, A., Bock, J., Boselli, A., Castro-Rodriguez, N., Cava, A., Chanial, P., Clements, D. L., Conley, A., Conversi, L., Cooray, A., Dowell, C. D., Dwek, E., Eales, S., Elbaz, D., Fox, M., Franceschini, A., Gear, W., Glenn, J., Griffin, M., Halpern, M., Hatziminaoglou, E., Heinis, S., Ibar, E., Isaak, K., Ivison, R. J., Lagache, G., Levenson, L., Lonsdale, C. J., Lu, N., Madden, S., Maffei, B., Magdis, G., Mainetti, G., Marchetti, L., Morrison, G. E., Nguyen, H. T., O'Halloran, B., Oliver, S. J., Omont, A., Owen, F. N., Page, M. J., Pannella, M., Panuzzo, P., Papageorgiou, A., Pearson, C. P., Perez-Fournon, I., Pohlen, M., Rigopoulou, D., Rizzo, D., Roseboom, I. G., Rowan-Robinson, M., Sanchez Portal, M., Schulz, B., Seymour, N., Shupe, D. L., Smith, A. J., Stevens, J. A., Strazzullo, V., Symeonidis, M., Trichas, M., Tugwell, K. E., Vaccari, M., Valiante, E., Valtchanov, I., Viagroux, L., Wang, L., Ward, R., Wright, G., Xu, C. K., & Zemcov, M. 2010, ArXiv e-prints

Buat, V., Takeuchi, T. T., Iglesias-Páramo, J., Xu, C. K., Burgarella, D., Boselli, A., Barlow, T., Bianchi, L., Donas, J., Forster, K., Friedman, P. G., Heckman, T. M., Lee, Y., Madore, B. F., Martin, D. C., Milliard, B., Morissey, P., Neff, S., Rich, M., Schiminovich, D., Seibert, M., Small, T., Szalay, A. S., Welsh, B., Wyder, T., & Yi, S. K. 2007, ApJS, 173, 404

Caputi, K. I., Dole, H., Lagache, G., McLure, R. J., Puget, J., Rieke, G. H., Dunlop, J. S., Le Floc'h, E., Papovich, C., & Pérez-González, P. G. 2006, ApJ, 637, 727

Chapin, E. L., Chapman, S. C., Coppin, K. E., Devlin, M. J., Dunlop, J. S., Greve, T. R., Halpern, M., Hasselfield, M. F., Hughes, D. H., Ivison, R. J., Marsden, G., Moncelsi, L., Netterfield, C. B., Pascale, E., Scott, D., Smail, I., Viero, M., Walter, F., Weiss, A., & van der Werf, P. 2010, ArXiv e-prints

Chapman, S. C., Blain, A. W., Smail, I., & Ivison, R. J. 2005, ApJ, 622, 772

Chary, R. & Elbaz, D. 2001, ApJ, 556, 562

Cid Fernandes, R., Stasińska, G., Schlickmann, M. S., Mateus, A., Vale Asari, N., Schoenell, W., & Sodré, L. 2010, MNRAS, 403, 1036

Colless, M., Peterson, B. A., Jackson, C., Peacock, J. A., Cole, S., Norberg, P., Baldry, I. K., Baugh, C. M., Bland-Hawthorn, J., Bridges, T., Cannon, R., Collins, C., Couch, W., Cross, N., Dalton, G., De Propris, R., Driver, S. P., Efstathiou, G., Ellis, R. S., Frenk, C. S., Glazebrook, K., Lahav, O., Lewis, I., Lumsden, S., Maddox, S., Madgwick, D., Sutherland, W., & Taylor, K. 2003, ArXiv Astrophysics e-prints

Coppin, K., Chapin, E. L., Mortier, A. M. J., Scott, S. E., Borys, C., Dunlop, J. S., Halpern, M., Hughes, D. H., Pope, A., Scott, D., Serjeant, S., Wagg, J., Alexander, D. M., Almaini, O., Aretxaga, I., Babbedge, T., Best, P. N., Blain, A., Chapman, S., Clements, D. L., Crawford, M., Dunne, L., Eales, S. A., Edge, A. C., Farrah, D., Gaztañaga, E., Gear, W. K., Granato, G. L., Greve, T. R., Fox, M., Ivison, R. J., Jarvis, M. J., Jeness, T., Lacey, C., Lepage, K., Mann, R. G., Marsden, G., Martinez-Sansigre, A., Oliver, S., Page, M. J., Peacock, J. A., Pearson, C. P., Percival, W. J., Priddey, R. S., Rawlings, S., Rowan-Robinson, M., Savage, R. S., Seigar, M., Sekiguchi, K., Silva, L., Simpson, C., Smail, I., Stevens, J. A., Takagi, T., Vaccari, M., van Kampen, E., & Willott, C. J. 2006, MNRAS, 372, 1621

Coppin, K., Halpern, M., Scott, D., Borys, C., & Chapman, S. 2005, MNRAS, 357, 1022

Coppin, K., Halpern, M., Scott, D., Borys, C., Dunlop, J., Dunne, L., Ivison, R., Wagg, J., Aretxaga, I., Battistelli, E., Benson, A., Blain, A., Chapman, S., Clements, D., Dye, S., Farrah, D., Hughes, D., Jenness, T., van Kampen, E., Lacey, C., Mortier, A., Pope, A., Priddey, R., Serjeant, S., Smail, I., Stevens, J., & Vaccari, M. 2008, MNRAS, 384, 1597

Coppin, K., Pope, A., Menéndez-Delmestre, K., Alexander, D. M., Dunlop, J. S., Egami, E., Gabor, J., Ibar, E., Ivison, R. J., Austermann, J. E., Blain, A. W., Chapman, S. C., Clements, D. L., Dunne, L., Dye, S., Farrah, D., Hughes, D. H., Mortier, A. M. J., Page, M. J., Rowan-Robinson, M., Scott, D., Simpson, C., Smail, I., Swinbank, A. M., Vaccari, M., & Yun, M. S. 2010, ApJ, 713, 503

Dale, D. A. & Helou, G. 2002, ApJ, 576, 159

Della Valle, A., Mazzei, P., Bettoni, D., Aussel, H., & de Zotti, G. 2006, A&A, 454, 453

Devlin, M. J., Ade, P. A. R., Aretxaga, I., Bock, J. J., Chapin, E. L., Griffin, M., Gundersen, J. O., Halpern, M., Hargrave, P. C., Hughes, D. H., Klein, J., Marsden, G., Martin, P. G., Mauskopf, P., Moncelsi, L., Netterfield, C. B., Ngo, H., Olmi, L., Pascale, E., Patanchon, G., Rex, M., Scott, D., Semisch, C., Thomas, N., Truch, M. D. P., Tucker, C., Tucker, G. S., Viero, M. P., & Wiebe, D. V. 2009, Nature, 458, 737

Devlin, M. J., Ade, P. A. R., Aretxaga, I., Bock, J. J., Chung, J., Chapin, E., Dicker, S. R., Griffin, M., Gundersen, J., Halpern, M., Hargrave, P., Hughes, D., Klein, J., Marsden, G., Martin, P., Mauskopf, P. D., Netterfield, B., Olmi, L., Pascale, E., Rex, M., Scott, D., Semisch, C., Truch, M., Tucker, C., Tucker, G., Turner, A. D., & Wiebe, D. 2004, in Presented at the Society of Photo-Optical Instrumentation Engineers (SPIE) Conference, Vol. 5498, Millimeter and Submillimeter Detectors for Astronomy II. Edited by Jonas Zmuidzinas, Wayne S. Holland and Stafford Withington Proceedings of the SPIE, Volume 5498, pp. 42-54 (2004)., ed. J. Zmuidzinas, W. S. Holland, & S. Withington, 42–54

Dickinson, M. & FIDEL team. 2007, in Bulletin of the American Astronomical Society, Vol. 38, Bulletin of the American Astronomical Society, 822–+

Dickinson, M., Giavalisco, M., & The Goods Team. 2003, in The Mass of Galaxies at Low and High Redshift, ed. R. Bender & A. Renzini, 324–+

Dole, H., Lagache, G., Puget, J.-L., Caputi, K. I., Fernández-Conde, N., Le Floc'h, E., Papovich, C., Pérez-González, P. G., Rieke, G. H., & Blaylock, M. 2006, A&A, 451, 417

Dunlop, J. S., Ade, P. A. R., Bock, J. J., Chapin, E. L., Cirasuolo, M., Coppin, K. E. K., Devlin, M. J., Griffin, M., Greve, T. R., Gundersen, J. O., Halpern, M., Hargrave, P. C., Hughes, D. H., Ivison, R. J., Klein, J., Kovacs, A., Marsden, G., Mauskopf, P., Netterfield, C. B., Olmi, L., Pascale, E., Patanchon, G., Rex, M., Scott, D., Semisch, C., Smail, I., Targett, T. A., Thomas, N., Truch, M. D. P., Tucker, C., Tucker, G. S., Viero, M. P., Walter, F., Wardlow, J. L., Weiss, A., & Wiebe, D. V. 2010, MNRAS, 1354

Dunne, L., Eales, S., Edmunds, M., Ivison, R., Alexander, P., & Clements, D. L. 2000, MNRAS, 315, 115

Dunne, L. & Eales, S. A. 2001, MNRAS, 327, 697

Dwek, E., Arendt, R. G., Hauser, M. G., Fixsen, D., Kelsall, T., Leisawitz, D., Pei, Y. C., Wright, E. L., Mather, J. C., Moseley, S. H., Odegard, N., Shafer, R., Silverberg, R. F., & Weiland, J. L. 1998, ApJ, 508, 106

Dye, S. 2008, MNRAS, 389, 1293

Dye, S. 2010, private communication

Dye, S., Ade, P. A. R., Bock, J. J., Chapin, E. L., Devlin, M. J., Dunlop, J. S., Eales, S. A., Griffin, M., Gundersen, J. O., Halpern, M., Hargrave, P. C., Hughes, D. H., Klein, J., Magnelli, B., Marsden, G., Mauskopf, P., Moncelsi, L., Netterfield, C. B., Olmi, L., Pascale, E., Patanchon, G., Rex, M., Scott, D., Semisch, C., Targett, T., Thomas, N., Truch, M. D. P., Tucker, C., Tucker, G. S., Viero, M. P., & Wiebe, D. V. 2009, ApJ, 703, 285

Dye, S., Dunne, L., Eales, S., Smith, D. J. B., Amblard, A., Auld, R., Baes, M., Baldry, I. K., Bamford, S., Blain, A. W., Bonfield, D. G., Bremer, M., Burgarella, D., Buttiglione, S., Cameron, E., Cava, A., Clements, D. L., Cooray, A., Croom, S., Dariush, A., de Zotti, G., Driver, S., Dunlop, J. S., Frayer, D., Fritz, J., Gardner, J. P., Gomez, H. L., Gonzalez-Nuevo, J., Herranz, D., Hill, D., Hopkins, A., Ibar, E., Ivison, R. J., Jarvis, M. J., Jones, D. H., Kelvin, L., Lagache, G., Leeuw, L., Liske, J., Lopez-Caniego, M., Loveday, J., Maddox, S., Michałowski, M. J., Negrello, M., Norberg, P., Page, M. J., Parkinson, H., Pascale, E., Peacock, J. A., Pohlen, M., Popescu, C., Prescott, M., Rigopoulou, D., Robotham, A., Rigby, E., Rodighiero, G., Samui, S., Scott, D., Serjeant, S., Sharp, R., Sibthorpe, B., Temi, P., Thompson, M. A., Tuffs, R., Valtchanov, I., van der Werf, P. P., van Kampen, E., & Verma, A. 2010a, A&A, 518, L10+

Dye, S., Eales, S., Moncelsi, L., & Pascale, E. 2010b, MNRAS, L104+

Dye, S., Eales, S. A., Aretxaga, I., Serjeant, S., Dunlop, J. S., Babbedge, T. S. R., Chapman, S. C., Cirasuolo, M., Clements, D. L., Coppin, K. E. K., Dunne, L., Egami, E., Farrah, D., Ivison, R. J., van Kampen, E., Pope, A., Priddey, R., Rieke, G. H., Schael, A. M., Scott, D., Simpson, C., Takagi, T., Takata, T., & Vacari, M. 2008, MNRAS, 386, 1107

Dye, S., Eales, S. A., Ashby, M. L. N., Huang, J., Egami, E., Brodwin, M., Lilly, S., & Webb, T. 2007, MNRAS, 375, 725

Eales, S., Chapin, E. L., Devlin, M. J., Dye, S., Halpern, M., Hughes, D. H., Marsden, G., Mauskopf, P., Moncelsi, L., Netterfield, C. B., Pascale, E., Patanchon, G., Raymond, G., Rex, M., Scott, D., Semisch, C., Siana, B., Truch, M. D. P., & Viero, M. P. 2009, ApJ, 707, 1779

Eales, S. A., Raymond, G., Roseboom, I. G., Altieri, B., Amblard, A., Arumugam, V., Auld, R., Aussel, H., Babbedge, T., Blain, A., Bock, J., Boselli, A., Brisbin, D., Buat, V., Burgarella, D., Castro-Rodríguez, N., Cava, A., Chanial, P., Clements, D. L., Conley, A., Conversi, L., Cooray, A., Dowell, C. D., Dwek, E., Dye, S., Elbaz, D., Farrah, D., Fox, M., Franceschini, A., Gear, W., Glenn, J., González Solares, E. A., Griffin, M., Harwit, M., Hatziminaoglou, E., Huang, J., Ibar, E., Isaak, K., Ivison, R. J., Lagache, G., Levenson, L., Lonsdale, C. J., Lu, N., Madden, S., Maffei, B., Mainetti, G., Marchetti, L., Morrison, G. E., Mortier, A. M. J., Nguyen, H. T., O'Halloran, B., Oliver, S. J., Omont, A., Owen, F. N., Page, M. J., Pannella, M., Panuzzo, P., Papageorgiou, A., Pearson, C. P., Pérez-Fournon, I., Pohlen, M., Rawlings, J. I., Rigopoulou, D., Rizzo, D., Rowan-Robinson, M., Sánchez Portal, M., Schulz, B., Scott, D., Seymour, N., Shupe, D. L., Smith, A. J., Stevens, J. A., Strazzullo, V., Symeonidis, M., Trichas, M., Tugwell, K. E., Vaccari, M., Valtchanov, I., Vieira, J., Vigroux, L., Wang, L., Ward, R., Wright, G., Xu, C. K., & Zemcov, M. 2010, A&A, 518, L29+

Eales, S. A., Raymond, G., Roseboom, I. G., Altieri, B., Amblard, A., Arumugam, V., Auld, R., Aussel, H., Babbedge, T., Blain, A., Bock, J., Boselli, A., Brisbin, D., Buat, V., Burgarella, D., Castro-Rodríguez, N., Cava, A., Chanial, P., Clements, D. L., Conley, A., Conversi, L., Cooray, A., Dowell, C. D., Dwek, E., Dye, S., Elbaz, D., Farrah, D., Fox, M., Franceschini, A., Gear, W., Glenn, J., González Solares, E. A., Griffin, M., Harwit, M., Hatziminaoglou, E., Huang, J., Ibar, E., Isaak, K., Ivison, R. J., Lagache, G., Levenson, L., Lonsdale, C. J., Lu, N., Madden, S., Maffei, B., Mainetti, G., Marchetti, L., Morrison, G. E., Mortier, A. M. J., Nguyen, H. T., O'Halloran, B., Oliver, S. J., Omont, A., Owen, F. N., Page, M. J., Pannella, M., Panuzzo, P., Papageorgiou, A., Pearson, C. P., Pérez-Fournon, I., Pohlen, M., Rawlings, J. I., Rigopoulou, D., Rizzo, D., Rowan-Robinson, M., Sánchez Portal, M., Schulz, B., Scott, D., Seymour, N., Shupe, D. L., Smith, A. J., Stevens, J. A., Sturm, E., Symeonidis, M., Tacconi, L., Trichas, M., Tugwell, K. E., Vaccari, M., Valtchanov, I., Vieira, J., Vigroux, L., Wang, L., Ward, R., Wright, G., Xu, C. K., & Zemcov, M. 2010, A&A, 518, L29+

Fazio, G. G., Hora, J. L., Allen, L. E., Ashby, M. L. N., Barmby, P., Deutsch, L. K., Huang, J., Kleiner, S., Marengo, M., Megeath, S. T., Melnick, G. J., Pahre, M. A., Patten, B. M., Polizotti, J., Smith, H. A., Taylor, R. S., Wang, Z., Willner, S. P., Hoffmann, W. F., Pipher, J. L., Forrest, W. J., McMurtty, C. W., McCreight, C. R., McKelvey, M. E., McMurray, R. E., Koch, D. G., Moseley, S. H., Arendt, R. G., Mentzell, J. E., Marx, C. T., Losch, P., Mayman, P., Eichhorn, W., Krebs, D., Jhabvala, M., Gezari, D. Y., Fixsen, D. J., Flores, J., Shakoorzadeh, K., Jungo, R., Hakun, C., Workman, L., Karpati, G., Kichak, R., Whitley, R., Mann, S., Tollestrup, E. V., Eisenhardt, P., Stern, D., Gorjian, V., Bhattacharya, B., Carey, S., Nelson, B. O., Glaccum, W. J., Lacy, M., Lowrance, P. J., Laine, S., Reach, W. T., Stauffer, J. A., Surace, J. A., Wilson, G., Wright, E. L., Hoffman, A., Domingo, G., & Cohen, M. 2004, ApJS, 154, 10

Fixsen, D. J., Dwek, E., Mather, J. C., Bennett, C. L., & Shafer, R. A. 1998, ApJ, 508, 123

Frayer, D. T., Sanders, D. B., Surace, J. A., Aussel, H., Salvato, M., Le Floc'h, E., Huynh, M. T., Scoville, N. Z., Afonso-Luis, A., Bhattacharya, B., Capak, P., Fadda, D., Fu, H., Helou, G., Ilbert, O., Kartaltepe, J. S., Koekemoer, A. M., Lee, N., Murphy, E., Sargent, M. T., Schinnerer, E., Sheth, K., Shopbell, P. L., Shupe, D. L., & Yan, L. 2009, AJ, 138, 1261

Gawiser, E., van Dokkum, P. G., Herrera, D., Maza, J., Castander, F. J., Infante, L., Lira, P., Quadri, R., Toner, R., Treister, E., Urry, C. M., Altmann, M., Assef, R., Christlein, D., Coppi, P. S., Durán, M. F., Franx, M., Galaz, G., Huerta, L., Liu, C., López, S.,

Méndez, R., Moore, D. C., Rubio, M., Ruiz, M. T., Toft, S., & Yi, S. K. 2006, *ApJS*, 162, 1

Gispert, R., Lagache, G., & Puget, J. L. 2000, *A&A*, 360, 1

Griffin, M. J., Abergel, A., Abreu, A., Ade, P. A. R., André, P., Auguera, J., Babbedge, T., Bae, Y., Baille, T., Baluteau, J., Barlow, M. J., Bendo, G., Benielli, D., Bock, J. J., Bonhomme, P., Brisbin, D., Brockley-Blatt, C., Caldwell, M., Cara, C., Castro-Rodríguez, N., Cerulli, R., Chanial, P., Chen, S., Clark, E., Clements, D. L., Clerc, L., Coker, J., Communal, D., Conversi, L., Cox, P., Crumb, D., Cunningham, C., Daly, F., Davis, G. R., de Antoni, P., Delderfield, J., Devin, N., di Giorgio, A., Didschuns, I., Dohlen, K., Donati, M., Dowell, A., Dowell, C. D., Duband, L., Dumaye, L., Emery, R. J., Ferlet, M., Ferrand, D., Fontignie, J., Fox, M., Franceschini, A., Frerking, M., Fulton, T., Garcia, J., Gastaud, R., Gear, W. K., Glenn, J., Goizel, A., Griffin, D. K., Grundy, T., Guest, S., Guillet, L., Hargrave, P. C., Harwit, M., Hastings, P., Hatziminaoglou, E., Herman, M., Hinde, B., Hristov, V., Huang, M., Imhof, P., Isaak, K. J., Israelsson, U., Ivison, R. J., Jennings, D., Kiernan, B., King, K. J., Lange, A. E., Latter, W., Laurent, G., Laurent, P., Leeks, S. J., Lellouch, E., Levenson, L., Li, B., Li, J., Lilienthal, J., Lim, T., Liu, S. J., Lu, N., Madden, S., Mainetti, G., Marliani, P., McKay, D., Mercier, K., Molinari, S., Morris, H., Moseley, H., Mulder, J., Mur, M., Naylor, D. A., Nguyen, H., O'Halloran, B., Oliver, S., Olofsson, G., Olofsson, H., Orfei, R., Page, M. J., Pain, I., Panuzzo, P., Papageorgiou, A., Parks, G., Parr-Burman, P., Pearce, A., Pearson, C., Pérez-Fournon, I., Pinsard, F., Pisano, G., Podosek, J., Pohlen, M., Polehampton, E. T., Pouliquen, D., Rigopoulou, D., Rizzo, D., Roseboom, I. G., Roussel, H., Rowan-Robinson, M., Rownd, B., Saraceno, P., Sauvage, M., Savage, R., Savini, G., Sawyer, E., Scharnberg, C., Schmitt, D., Schneider, N., Schulz, B., Schwartz, A., Shafer, R., Shupe, D. L., Sibthorpe, B., Sidher, S., Smith, A., Smith, A. J., Smith, D., Spencer, L., Stobie, B., Sudiwala, R., Sukhatme, K., Surace, C., Stevens, J. A., Swinyard, B. M., Trichas, M., Tourette, T., Triou, H., Tseng, S., Tucker, C., Turner, A., Vaccari, M., Valtchanov, I., Vigroux, L., Virique, E., Voellmer, G., Walker, H., Ward, R., Waskett, T., Weilert, M., Wesson, R., White, G. J., Whitehouse, N., Wilson, C. D., Winter, B., Woodcraft, A. L., Wright, G. S., Xu, C. K., Zavagno, A., Zemcov, M., Zhang, L., & Zonca, E. 2010, *A&A*, 518, L3+

Hatziminaoglou, E., Omont, A., Stevens, J. A., Amblard, A., Arumugam, V., Auld, R., Aussel, H., Babbedge, T., Blain, A., Bock, J., Boselli, A., Buat, V., Bur-
garella, D., Castro-Rodríguez, N., Cava, A., Charnier, P., Clements, D. L., Conley, A., Conversi, L., Cooray, A., Dowell, C. D., Dwek, E., Dye, S., Eales, S., Elbaz, D., Farrah, D., Fox, M., Franceschini, A., Gear, W., Glenn, J., González Solares, E. A., Griffin, M., Halpern, M., Ibar, E., Isaak, K., Ivison, R. J., Lagache, G., Levenson, L., Lu, N., Madden, S., Maffei, B., Mainetti, G., Marchetti, L., Mortier, A. M. J., Nguyen, H. T., O'Halloran, B., Oliver, S. J., Page, M. J., Panuzzo, P., Papageorgiou, A., Pearson, C. P., Pérez-Fournon, I., Pohlen, M., Rawlings, J. I., Rigopoulou, D., Rizzo, D., Roseboom, I. G., Rowan-Robinson, M., Sanchez Portal, M., Schulz, B., Scott, D., Seymour, N., Shupe, D. L., Smith, A. J., Symeonidis, M., Trichas, M., Tugwell, K. E., Vaccari, M., Valtchanov, I., Vigroux, L., Wang, L., Ward, R., Wright, G., Xu, C. K., & Zemcov, M. 2010, *A&A*, 518, L33+

Hatziminaoglou, E., Pérez-Fournon, I., Polletta, M., Afonso-Luis, A., Hernán-Caballero, A., Montenegro-Montes, F. M., Lonsdale, C., Xu, C. K., Franceschini, A., Rowan-Robinson, M., Babbedge, T., Smith, H. E., Surace, J., Shupe, D., Fang, F., Farrah, D., Oliver, S., González-Solares, E. A., & Serjeant, S. 2005, *AJ*, 129, 1198

Hauser, M. G. & Dwek, E. 2001, *ARA&A*, 39, 249

Heavens, A., Panter, B., Jimenez, R., & Dunlop, J. 2004, *Nature*, 428, 625

Hildebrand, R. H. 1983, *QJRAS*, 24, 267

Hinshaw, G., Weiland, J. L., Hill, R. S., Odegard, N., Larson, D., Bennett, C. L., Dunkley, J., Gold, B., Greason, M. R., Jarosik, N., Komatsu, E., Nolta, M. R., Page, L., Spergel, D. N., Wollack, E., Halpern, M., Kogut, A., Limon, M., Meyer, S. S., Tucker, G. S., & Wright, E. L. 2009, *ApJS*, 180, 225

Hirashita, H., Buat, V., & Inoue, A. K. 2003, *A&A*, 410, 83

Hopkins, A. M., Miller, C. J., Nichol, R. C., Connolly, A. J., Bernardi, M., Gómez, P. L., Goto, T., Tremonti, C. A., Brinkmann, J., Ivezić, Ž., & Lamb, D. Q. 2003, *ApJ*, 599, 971

Hughes, D. H., Serjeant, S., Dunlop, J., Rowan-Robinson, M., Blain, A., Mann, R. G., Ivison, R., Peacock, J., Efstathiou, A., Gear, W., Oliver, S., Lawrence, A., Longair, M., Goldschmidt, P., & Jeness, T. 1998, *Nature*, 394, 241

Iglesias-Páramo, J., Buat, V., Donas, J., Boselli, A., & Milliard, B. 2004, *A&A*, 419, 109

Iglesias-Páramo, J., Buat, V., Takeuchi, T. T., Xu, K., Boissier, S., Boselli, A., Burgarella, D., Madore, B. F., Gil de Paz, A., Bianchi, L., Barlow, T. A., Byun, Y.-I., Donas, J., Forster, K., Friedman, P. G., Heckman, T. M., Jelinski, P. N., Lee, Y.-W., Malina, R. F., Martin, D. C., Milliard, B., Morrissey, P. F., Neff, S. G., Rich, R. M., Schiminovich, D., Seibert, M., Siegmund, O. H. W., Small, T., Szalay, A. S., Welsh, B. Y., & Wyder, T. K. 2006, *ApJS*, 164, 38

Inoue, A. K. 2002, *ApJ*, 570, L97

Ivison, R. J., Alexander, D. M., Biggs, A. D., Brandt, W. N., Chapin, E. L., Coppin, K. E. K., Devlin, M. J., Dickinson, M., Dunlop, J., Dye, S., Eales, S. A., Frayer, D. T., Halpern, M., Hughes, D. H., Ibar, E., Kovács, A., Marsden, G., Moncelsi, L., Netterfield, C. B., Pascale, E., Patanchon, G., Rafferty, D. A., Rex, M., Schinnerer, E., Scott, D., Semisch, C., Smail, I., Swinbank, A. M., Truch, M. D. P., Tucker, G. S., Viero, M. P., Walter, F., Weiß, A., Wiebe, D. V., & Xue, Y. Q. 2010, *MNRAS*, 402, 245

Kauffmann, G., Heckman, T. M., Tremonti, C., Brinchmann, J., Charlot, S., White, S. D. M., Ridgway, S. E., Brinkmann, J., Fukugita, M., Hall, P. B., Ivezić, Ž., Richards, G. T., & Schneider, D. P. 2003, *MNRAS*, 346, 1055

Kennicutt, Jr., R. C. 1998, *ARA&A*, 36, 189

Kriek, M., van Dokkum, P. G., Franx, M., Illingworth, G. D., Marchesini, D., Quadri, R., Rudnick, G., Taylor, E. N., Förster Schreiber, N. M., Gawiser, E., Labbé, I., Lira, P., & Wuyts, S. 2008, *ApJ*, 677, 219

Lacy, M., Storrie-Lombardi, L. J., Sajina, A., Appleton, P. N., Armus, L., Chapman, S. C., Choi, P. I., Fadda, D., Fang, F., Frayer, D. T., Heinrichsen, I., Helou, G., Im, M., Marleau, F. R., Masci, F., Shupe, D. L., Soifer, B. T., Surace, J., Teplitz, H. I., Wilson, G., & Yan, L. 2004, *ApJS*, 154, 166

Le Floc'h, E., Papovich, C., Dole, H., Bell, E. F., Lagache, G., Rieke, G. H., Egami, E., Pérez-González, P. G., Alonso-Herrero, A., Rieke, M. J., Blaylock, M., Engelbracht, C. W., Gordon, K. D., Hines, D. C., Miseit, K. A., Morrison, J. E., & Mould, J. 2005, *ApJ*, 632, 169

Leitherer, C., Schaerer, D., Goldader, J. D., González Delgado, R. M., Robert, C., Kune, D. F., de Mello, D. F., Devost, D., & Heckman, T. M. 1999, *ApJS*, 123, 3

Lonsdale, C., Polletta, M. d. C., Surace, J., Shupe, D., Fang, F., Xu, C. K., Smith, H. E., Siana, B., Rowan-Robinson, M., Babbedge, T., Oliver, S., Pozzi, F., Davoodi, P., Owen, F., Padgett, D., Frayer, D., Jarrett, T., Masci, F., O'Linger, J., Conrow, T., Farrah, D., Morrison, G., Gautier, N., Franceschini, A., Berta, S., Perez-Fournon, I., Hatziminaoglou, E., Afonso-Luis, A., Dole, H., Stacey, G., Serjeant, S., Pierre, M., Griffin, M., & Puetter, R. 2004, *ApJS*, 154, 54

Magnelli, B., Elbaz, D., Chary, R. R., Dickinson, M., Le Borgne, D., Frayer, D. T., & Willmer, C. N. A. 2009, *A&A*, 496, 57

Marsden, G., Ade, P. A. R., Bock, J. J., Chapin, E. L., Devlin, M. J., Dicker, S. R., Griffin, M., Gundersen, J. O., Halpern, M., Hargrave, P. C., Hughes, D. H., Klein, J., Mauskopf, P., Magnelli, B., Moncelsi, L., Netterfield, C. B., Ngo, H., Olmi, L., Pascale, E., Patanchon, G., Rex, M., Scott, D., Semisch, C., Thomas, N., Truch, M. D. P., Tucker, C., Tucker, G. S., Viero, M. P., & Wiebe, D. V. 2009, *ApJ*, 707, 1729

Martin, D. C., Fanson, J., Schiminovich, D., Morrissey, P., Friedman, P. G., Barlow, T. A., Conrow, T., Grange, R., Jelinsky, P. N., Milliard, B., Siegmund, O. H. W., Bianchi, L., Byun, Y., Donas, J., Forster, K., Heckman, T. M., Lee, Y., Madore, B. F., Malina, R. F., Neff, S. G., Rich, R. M., Small, T., Surber, F., Szalay, A. S., Welsh, B., & Wyder, T. K. 2005, *ApJ*, 619, L1

Mazzei, P., Della Valle, A., & Bettoni, D. 2007, *A&A*, 462, 21

Miller, C. J., Nichol, R. C., Gómez, P. L., Hopkins, A. M., & Bernardi, M. 2003, *ApJ*, 597, 142

Miller, N. A., Fomalont, E. B., Kellermann, K. I., Mainieri, V., Norman, C., Padovani, P., Rosati, P., & Tozzi, P. 2008, *ApJS*, 179, 114

Morrissey, P., Conrow, T., Barlow, T. A., Small, T., Seibert, M., Wyder, T. K., Budavári, T., Arnouts, S., Friedman, P. G., Forster, K., Martin, D. C., Neff, S. G., Schiminovich, D., Bianchi, L., Donas, J., Heckman, T. M., Lee, Y., Madore, B. F., Milliard, B., Rich, R. M., Szalay, A. S., Welsh, B. Y., & Yi, S. K. 2007, *ApJS*, 173, 682

Murphy, E. J., Chary, R., Alexander, D. M., Dickinson, M., Magnelli, B., Morrison, G., Pope, A., & Teplitz, H. I. 2009, *ApJ*, 698, 1380

Muzzin, A., van Dokkum, P., Kriek, M., Labbe, I., Cury, I., Marchesini, D., & Franx, M. 2010, ArXiv e-prints

Nordon, R., Lutz, D., Shao, L., Magnelli, B., Berta, S., Altieri, B., Andreani, P., Aussel, H., Bongiovanni, A., Cava, A., Cepa, J., Cimatti, A., Daddi, E., Dominguez, H., Elbaz, D., Förster Schreiber,

N. M., Genzel, R., Grazian, A., Magdis, G., Maiolino, R., Pérez García, A. M., Poglitsch, A., Popesso, P., Pozzi, F., Riguccini, L., Rodighiero, G., Saintonge, A., Sanchez-Portal, M., Santini, P., Sturm, E., Tacconi, L., Valtchanov, I., Wetzstein, M., & Wiprecht, E. 2010, *A&A*, 518, L24+

Norris, R. P., Afonso, J., Appleton, P. N., Boyle, B. J., Ciliegi, P., Croom, S. M., Huynh, M. T., Jackson, C. A., Koekemoer, A. M., Lonsdale, C. J., Middelberg, E., Mobasher, B., Oliver, S. J., Polletta, M., Siana, B. D., Smail, I., & Voronkov, M. A. 2006, *AJ*, 132, 2409

Papovich, C., Rudnick, G., Le Floc'h, E., van Dokkum, P. G., Rieke, G. H., Taylor, E. N., Armus, L., Gawiser, E., Huang, J., Marcillac, D., & Franx, M. 2007, *ApJ*, 668, 45

Pascale, E., Ade, P. A. R., Bock, J. J., Chapin, E. L., Chung, J., Devlin, M. J., Dicker, S., Griffin, M., Gundersen, J. O., Halpern, M., Hargrave, P. C., Hughes, D. H., Klein, J., MacTavish, C. J., Marsden, G., Martin, P. G., Martin, T. G., Mauskopf, P., Netterfield, C. B., Olmi, L., Patanchon, G., Rex, M., Scott, D., Semisch, C., Thomas, N., Truch, M. D. P., Tucker, C., Tucker, G. S., Viero, M. P., & Wiebe, D. V. 2008, *ApJ*, 681, 400

Pascale, E., Ade, P. A. R., Bock, J. J., Chapin, E. L., Devlin, M. J., Dye, S., Eales, S. A., Griffin, M., Gundersen, J. O., Halpern, M., Hargrave, P. C., Hughes, D. H., Klein, J., Marsden, G., Mauskopf, P., Moncelsi, L., Ngo, H., Netterfield, C. B., Olmi, L., Patanchon, G., Rex, M., Scott, D., Semisch, C., Thomas, N., Truch, M. D. P., Tucker, C., Tucker, G. S., Viero, M. P., & Wiebe, D. V. 2009, *ApJ*, 707, 1740

Patanchon, G., Ade, P. A. R., Bock, J. J., Chapin, E. L., Devlin, M. J., Dicker, S. R., Griffin, M., Gundersen, J. O., Halpern, M., Hargrave, P. C., Hughes, D. H., Klein, J., Marsden, G., Mauskopf, P., Moncelsi, L., Netterfield, C. B., Olmi, L., Pascale, E., Rex, M., Scott, D., Semisch, C., Thomas, N., Truch, M. D. P., Tucker, C., Tucker, G. S., Viero, M. P., & Wiebe, D. V. 2009, *ApJ*, 707, 1750

Pérez-González, P. G., Rieke, G. H., Egami, E., Alonso-Herrero, A., Dole, H., Papovich, C., Blaylock, M., Jones, J., Rieke, M., Rigby, J., Barmby, P., Fazio, G. G., Huang, J., & Martin, C. 2005, *ApJ*, 630, 82

Pilbratt, G. L., Riedinger, J. R., Passvogel, T., Crone, G., Doyle, D., Gageur, U., Heras, A. M., Jewell, C., Metcalfe, L., Ott, S., & Schmidt, M. 2010, *A&A*, 518, L1+

Pope, A., Borys, C., Scott, D., Conselice, C., Dickinson, M., & Mobasher, B. 2005, *MNRAS*, 358, 149

Pope, A., Scott, D., Dickinson, M., Chary, R., Morrison, G., Borys, C., Sajina, A., Alexander, D. M., Daddi, E., Frayer, D., MacDonald, E., & Stern, D. 2006, *MNRAS*, 370, 1185

Puget, J.-L., Abergel, A., Bernard, J.-P., Boulanger, F., Burton, W. B., Desert, F.-X., & Hartmann, D. 1996, *A&A*, 308, L5+

Ratcliffe, A., Shanks, T., Parker, Q. A., Broadbent, A., Watson, F. G., Oates, A. P., Collins, C. A., & Fong, R. 1998, *MNRAS*, 300, 417

Ravikumar, C. D., Puech, M., Flores, H., Proust, D., Hammer, F., Lehnert, M., Rawat, A., Amram, P., Balkowski, C., Burgarella, D., Cassata, P., Cesarsky, C., Cimatti, A., Combes, F., Daddi, E., Dannerbauer, H., di Serego Alighieri, S., Elbaz, D., Guiderdoni, B., Kembhavi, A., Liang, Y. C., Pozzetti, L., Vergani, D., Vernet, J., Wozniak, H., & Zheng, X. Z. 2007, *A&A*, 465, 1099

Rieke, G. H., Young, E. T., Engelbracht, C. W., Kelly, D. M., Low, F. J., Haller, E. E., Beeman, J. W., Gordon, K. D., Stansberry, J. A., Misselt, K. A., Cadien, J., Morrison, J. E., Rivlis, G., Latter, W. B., Noriega-Crespo, A., Padgett, D. L., Stapelfeldt, K. R., Hines, D. C., Egami, E., Muzerolle, J., Alonso-Herrero, A., Blaylock, M., Dole, H., Hinz, J. L., Le Floc'h, E., Papovich, C., Pérez-González, P. G., Smith, P. S., Su, K. Y. L., Bennett, L., Frayer, D. T., Henderson, D., Lu, N., Masci, F., Pesenson, M., Rebull, L., Rho, J., Keene, J., Stolovy, S., Wachter, S., Wheaton, W., Werner, M. W., & Richards, P. L. 2004, *ApJS*, 154, 25

Rodighiero, G., Cimatti, A., Gruppioni, C., Popesso, P., Andreani, P., Altieri, B., Aussel, H., Berta, S., Bongiovanni, A., Brisbin, D., Cava, A., Cepa, J., Daddi, E., Dominguez-Sanchez, H., Elbaz, D., Fontana, A., Förster Schreiber, N., Franceschini, A., Genzel, R., Grazian, A., Lutz, D., Magdis, G., Magliocchetti, M., Magnelli, B., Maiolino, R., Mancini, C., Norrdon, R., Perez Garcia, A. M., Poglitsch, A., Santini, P., Sanchez-Portal, M., Pozzi, F., Riguccini, L., Saintonge, A., Shao, L., Sturm, E., Tacconi, L., Valtchanov, I., Wetzstein, M., & Wiprecht, E. 2010, *A&A*, 518, L25+

Rowan-Robinson, M. 2001, *ApJ*, 549, 745

Rowan-Robinson, M., Babbedge, T., Oliver, S., Trichas, M., Berta, S., Lonsdale, C., Smith, G., Shupe, D., Surace, J., Arnouts, S., Ilbert, O., Le Févre, O., Afonso-Luis, A., Perez-Fournon, I., Hatziminaoglou, E., Polletta, M., Farrah, D., & Vaccari, M. 2008, *MNRAS*, 386, 697

Salpeter, E. E. 1955, *ApJ*, 121, 161

Santini, P., Fontana, A., Grazian, A., Salimbeni, S., Fiore, F., Fontanot, F., Boutsia, K., Castellano, M., Cristiani, S., de Santis, C., Gallozzi, S., Giallongo, E., Menci, N., Nonino, M., Paris, D., Pentericci, L., & Vanzella, E. 2009, *A&A*, 504, 751

Schlegel, D. J., Finkbeiner, D. P., & Davis, M. 1998, *ApJ*, 500, 525

Schulz, B., Pearson, C. P., Clements, D. L., Altieri, B., Amblard, A., Arumugam, V., Auld, R., Aussel, H., Babbedge, T., Blain, A., Bock, J., Boselli, A., Buat, V., Burgarella, D., Castro-Rodríguez, N., Cava, A., Chanial, P., Conley, A., Conversi, L., Cooray, A., Dowell, C. D., Dwek, E., Eales, S., Elbaz, D., Fox, M., Franceschini, A., Gear, W., Giovannoli, E., Glenn, J., Griffin, M., Halpern, M., Hatziminaoglou, E., Ibar, E., Isaak, K., Ivison, R. J., Lagache, G., Levenson, L., Lu, N., Madden, S., Maffei, B., Mainetti, G., Marchetti, L., Marsden, G., Mortier, A. M. J., Nguyen, H. T., O'Halloran, B., Oliver, S. J., Omont, A., Page, M. J., Panuzzo, P., Papageorgiou, A., Pérez-Fournon, I., Pohlen, M., Rangwala, N., Rawlings, J. I., Raymond, G., Rigopoulou, D., Rizzo, D., Roseboom, I. G., Rowan-Robinson, M., Sánchez Portal, M., Scott, D., Seymour, N., Shupe, D. L., Smith, A. J., Stevens, J. A., Symeonidis, M., Trichas, M., Tugwell, K. E., Vaccari, M., Valiante, E., Valtchanov, I., Vigroux, L., Wang, L., Ward, R., Wright, G., Xu, C. K., & Zemcov, M. 2010, *A&A*, 518, L32+

Serjeant, S., Dye, S., Mortier, A., Peacock, J., Egami, E., Cirasuolo, M., Rieke, G., Borys, C., Chapman, S., Clements, D., Coppin, K., Dunlop, J., Eales, S., Farrah, D., Halpern, M., Mauskopf, P., Pope, A., Rowan-Robinson, M., Scott, D., Smail, I., & Vaccari, M. 2008, *MNRAS*, 386, 1907

Shao, L., Lutz, D., Nordon, R., Maiolino, R., Alexander, D. M., Altieri, B., Andreani, P., Aussel, H., Bauer, F. E., Berta, S., Bongiovanni, A., Brandt, W. N., Brusa, M., Cava, A., Cepa, J., Cimatti, A., Daddi, E., Dominguez-Sánchez, H., Elbaz, D., Förster Schreiber, N. M., Geis, N., Genzel, R., Grazian, A., Gruppioni, C., Magdis, G., Magnelli, B., Mainieri, V., Pérez García, A. M., Poglitsch, A., Popesso, P., Pozzi, F., Riguccini, L., Rodighiero, G., Rovilos, E., Saintonge, A., Salvato, M., Sanchez Portal, M., Santini, P., Sturm, E., Tacconi, L. J., Valtchanov, I., Wetzstein, M., & Wiprecht, E. 2010, *A&A*, 518, L26+

Sharp, R., Saunders, W., Smith, G., Churilov, V., Correll, D., Dawson, J., Farrel, T., Frost, G., Haynes, R., Heald, R., Lankshear, A., Mayfield, D., Waller, L., & Whittard, D. 2006, in Presented at the Society of Photo-Optical Instrumentation Engineers (SPIE) Conference, Vol. 6269, Society of Photo-Optical Instrumentation Engineers (SPIE) Conference Series

Silverman, J. D., Lamareille, F., Maier, C., Lilly, S. J., Mainieri, V., Brusa, M., Cappelluti, N., Hasinger, G., Zamorani, G., Scudegger, M., Bolzonella, M., Contini, T., Carollo, C. M., Jahnke, K., Kneib, J., Le Fèvre, O., Merloni, A., Bardelli, S., Bongiorno, A., Brunner, H., Caputi, K., Civano, F., Comastri, A., Coppa, G., Cucciati, O., de la Torre, S., de Ravel, L., Elvis, M., Finoguenov, A., Fiore, F., Franzetti, P., Garilli, B., Gilli, R., Iovino, A., Kampczyk, P., Knobel, C., Kovač, K., Le Borgne, J., Le Brun, V., Mignoli, M., Pello, R., Peng, Y., Montero, E. P., Ricciardelli, E., Tanaka, M., Tasca, L., Tresse, L., Vergani, D., Vignali, C., Zucca, E., Bottini, D., Cappi, A., Cassata, P., Fumana, M., Griffiths, R., Kartaltepe, J., Koekeboer, A., Marinoni, C., McCracken, H. J., Memeo, P., Meneux, B., Oesch, P., Porciani, C., & Salvato, M. 2009, *ApJ*, 696, 396

Smail, I., Ivison, R. J., & Blain, A. W. 1997, *ApJ*, 490, L5+

Stern, D., Eisenhardt, P., Gorjian, V., Kochanek, C. S., Caldwell, N., Eisenstein, D., Brodwin, M., Brown, M. J. I., Cool, R., Dey, A., Green, P., Jannuzi, B. T., Murray, S. S., Pahre, M. A., & Willner, S. P. 2005, *ApJ*, 631, 163

Surace, J. A., Shupe, D. L., Fang, F., Evans, T., Alexov, A., Frayer, D., Lonsdale, C. J., & SWIRE Team. 2005, in *Bulletin of the American Astronomical Society*, Vol. 37, *Bulletin of the American Astronomical Society*, 1246–+

Takeuchi, T. T., Buat, V., Heinis, S., Giovannoli, E., Yuan, F., Iglesias-Paramo, J., Murata, K. L., & Burgarella, D. 2009, ArXiv e-prints

Taylor, E. N., Franx, M., van Dokkum, P. G., Quadri, R. F., Gawiser, E., Bell, E. F., Barrientos, L. F., Blanc, G. A., Castander, F. J., Damen, M., Gonzalez-Perez, V., Hall, P. B., Herrera, D., Hildebrandt, H., Kriek, M., Labbé, I., Lira, P., Maza, J., Rudnick, G., Treister, E., Urry, C. M., Willis, J. P., & Wuyts, S. 2009, *ApJS*, 183, 295

Truch, M. D. P., Ade, P. A. R., Bock, J. J., Chapin, E. L., Devlin, M. J., Dicker, S. R., Griffin, M., Gundersen, J. O., Halpern, M., Hargrave, P. C., Hughes, D. H., Klein, J., Marsden, G., Martin, P. G., Mauskopf, P., Moncelsi, L., Barth Netterfield, C., Olmi, L., Pascale, E., Patanchon, G., Rex, M., Scott, D., Semisch, C., Thomas, N. E., Tucker, C., Tucker, G. S., Viero, M. P., & Wiebe, D. V. 2009, *ApJ*, 707, 1723

Viero, M. P., Moncelsi, L., Buitrago, F., Marsden, G., Bauer, A. E., Trujillo, I., Conselice, C. J., Pérez-González, P. G., Chapin, E. L., Devlin, M. J., Halpern, M., Mentuch, E., Netterfield, C. B., Pascale, E., Rex, M., Scott, D., Truch, M. D. P., & Wiebe, D. V. 2010, ArXiv e-prints

Vlahakis, C., Dunne, L., & Eales, S. 2005, MNRAS, 364, 1253

Vollmann, K. & Eversberg, T. 2006, Astronomische Nachrichten, 327, 862

Weiβ, A., Kovács, A., Coppin, K., Greve, T. R., Walter, F., Smail, I., Dunlop, J. S., Knudsen, K. K., Alexander, D. M., Bertoldi, F., Brandt, W. N., Chapman, S. C., Cox, P., Dannerbauer, H., De Breuck, C., Gawiser, E., Ivison, R. J., Lutz, D., Menten, K. M., Koekemoer, A. M., Kreysa, E., Kurczynski, P., Rix, H., Schinnerer, E., & van der Werf, P. P. 2009, ApJ, 707, 1201

Wiebe, D. V., Ade, P. A. R., Bock, J. J., Chapin, E. L., Devlin, M. J., Dicker, S., Griffin, M., Gundersen, J. O., Halpern, M., Hargrave, P. C., Hughes, D. H., Klein, J., Marsden, G., Martin, P. G., Mauskopf, P., Netterfield, C. B., Olmi, L., Pascale, E., Patanchon, G., Rex, M., Scott, D., Semisch, C., Thomas, N., Truch, M. D. P., Tucker, C., Tucker, G. S., & Viero, M. P. 2009, ApJ, 707, 1809

Wolf, C., Hildebrandt, H., Taylor, E. N., & Meisenheimer, K. 2008, ArXiv e-prints

Wolf, C., Meisenheimer, K., Kleinheinrich, M., Borch, A., Dye, S., Gray, M., Wisotzki, L., Bell, E. F., Rix, H.-W., Cimatti, A., Hasinger, G., & Szokoly, G. 2004, A&A, 421, 913

Wyder, T. K., Martin, D. C., Schiminovich, D., Seibert, M., Budavári, T., Treyer, M. A., Barlow, T. A., Forster, K., Friedman, P. G., Morrissey, P., Neff, S. G., Small, T., Bianchi, L., Donas, J., Heckman, T. M., Lee, Y., Madore, B. F., Milliard, B., Rich, R. M., Szalay, A. S., Welsh, B. Y., & Yi, S. K. 2007, ApJS, 173, 293